

**DEVELOPMENT OF PLASMONIC
NANOSTRUCTURES FOR PHOTOTHERMAL
THERAPY OF PROSTATE AND BREAST CANCER**

**A Thesis Submitted to
the Graduate School of Engineering and Sciences of
İzmir Institute of Technology
in Partial Fulfillments of the Requirements for the Degree of**

**DOCTOR OF PHILOSOPHY
in Materials Science and Engineering**

**by
Aysel TOMAK**

December 2019

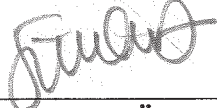
İZMİR

We approve the thesis of Aysel TOMAK

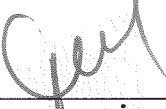
Examining Committee Members:



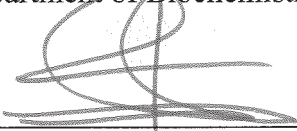
Prof. Dr. Volga BULMUŞ
Department of Bioengineering, İzmir Institute of Technology



Prof. Dr. Gülperi ÖKTEM
Department of Histology and Embryology, Ege University



Prof. Dr. Suna TİMUR
Department of Biochemistry, Ege University



Prof. Dr. Mustafa M. DEMİR
Department of Materials Science and Engineering, İzmir Institute of Technology



Assoc. Prof. Dr. Yaşar AKDOĞAN
Department of Materials Science and Engineering, İzmir Institute of Technology

19 December 2019



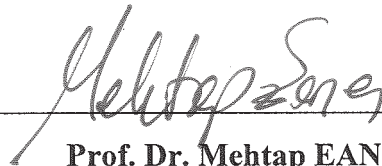
Prof. Dr. Volga BULMUŞ
Supervisor, Department of Bioengineering
İzmir Institute of Technology



Prof. Dr. Hasan ŞAHİN
Co-Supervisor, Department of Photonics
İzmir Institute of Technology



Prof. Dr. Haldun SEVİNÇLİ
Head of the Department of Materials
Science and Engineering



Prof. Dr. Mehtap EANES
Dean of the Graduate School of
Engineering and Sciences

ACKNOWLEDGMENTS

Foremost, I would like to thank my advisor Prof. Dr. Volga BULMUŞ for her generous support, knowledge, guidance and suggestions throughout of this research. It has been an honor to me to be the member of her team. I would also like to thank my previous advisor Dr. Hadi M. ZAREIE for helping me learn about instruments.

I would like to thank The Scientific and Technological Research Council of Turkey (TÜBİTAK, GRANT #: 112T507, 213M673 and 117F186) for providing financial support during my PhD. I would like to thank Prof. Dr. Gülperi ÖKTEM for non-commercial cell-specific antibody and always spreading positive vibes.

I would like to thank staff of Research Centers in İYTE for their contributions; Biotechnology and Bioengineering Applications and Research Centre (BIOMER): especially Özgür OKUR for flow cytometry experiments and Yekta GÜNAY OĞUZ for lyophilization process, Environmental Development Application and Research Center (Environmental R&D): Sanem Ezgi KINAL for ICP-MS analyses, The Center for Materials Research (IZTECH-CMR): Duygu OĞUZ KILIÇ, Mutlu Devran YAMAN and Zehra Sinem YILMAZ for Scanning Electron Microscopy analyses. And I also would like to thank to staff of Central Research Test and Analysis Laboratory Application and Research Center (EGE-MATAL); Ayşegül ERDOĞAN for XPS analyses. And I am also thankful to other colleagues from different universities for our collaborative study.

To our research team; Aykut ZELÇAK, Gözde YEŞİLTAŞ, Aytaç GÜL for their helps and supports. Especially, I thank to Damla TAYKOZ and Gürbüz DURSUN for their friendship and contributions in the last days of my thesis.

I appreciatively thank to my family, my brother Mustafa TOMAK, my mother Zehra TOMAK and my father Mehmet TOMAK for their understanding, encouragement, bottomless love and support during my PhD.

ABSTRACT

DEVELOPMENT OF PLASMONIC NANOSTRUCTURES FOR PHOTOTHERMAL THERAPY OF PROSTATE AND BREAST CANCER

The aim of this thesis is to synthesize gold nanorods (AuNRs) and lipid-stabilized nanobubbles containing AuNRs and investigate the potential of these plasmonic nanostructures as photothermal therapy agents for breast and prostate cancer through *in vitro* cell culture experiments. For this aim, firstly, AuNRs were synthesized at varying aspect ratios (ARs) and characterized via several techniques including UV-Vis/NIR spectroscopy, scanning electron microscopy (SEM), atomic force microscopy (AFM), inductively coupled plasma-mass spectroscopy (ICP-MS), electrophoretic light scattering (ELS) and X-ray photoelectron spectroscopy (XPS). The surface of AuNRs was modified with a biocompatible polymer, poly(ethylene glycol) (PEG), via ligand exchange method. Cytotoxicity, cell uptake and photothermal effects of AuNRs were investigated via *in vitro* cell culture experiments using human prostate cancer (DU 145) and epithelial (RWPE-1), breast cancer (MCF7) and epithelial (MCF 10A) cell lines. It was concluded that AuNRs (AR=4.0) were superior than AuNRs (AR=7.0) in terms of cell viability and photothermal effect. Separately, a non-commercial antibody (Ab) targeting a specific sialic acid derivative on the plasma membrane of DU 145 and MCF7 cancer cells was conjugated to AuNRs. Conjugations were characterized with the same techniques and investigated via *in vitro* cytotoxicity and cell uptake experiments. The Ab-conjugated AuNRs displayed the capability of selective targeting prostate cancer cells.

Additionally, lipid-stabilized AuNRs and lipid-stabilized nanobubbles containing AuNRs (AuNBs) were synthesized for the first time and characterized using UV-Vis/NIR spectroscopy, SEM, ICP-MS and ELS techniques. Lipid-stabilized AuNRs were successfully synthesized using varying lipid mixtures instead of cationic, toxic surfactant. Separately, AuNBs were synthesized by combining PEG-modified AuNRs with DPPC: DSPE-PEG lipid film under sonication and gas stream. AuNBs showed the same or significantly lower toxicity depending on the cell types and the same photothermal effect with respect to AuNRs (AR=4.0) upon irradiation under laser at 808 nm.

ÖZET

PROSTAT VE MEME KANSERİ FOTOTERMAL TEDAVİSİ İÇİN PLAZMONİK NANOYAPILARIN GELİŞTİRİLMESİ

Bu tezin amacı, altın nanoçubukları (AuNRs) ve altın nanoçubukları içeren lipit stabilize edilmiş nanobalonları sentezlemek ve bu plazmonik nanoyapıların, *in vitro* hücre kültürü deneyleri aracılığıyla meme ve prostat kanseri için fototermal terapi maddeleri olarak potansiyelini araştırmaktır. Bu amaçla, ilk olarak, altın nanoçubuklar değişen boy-en oranlarında sentezlendi ve UV-Vis/NIR spektroskopisi, taramalı elektron mikroskobu (SEM), atomik kuvvet mikroskobu (AFM), indüktif olarak eşleşmiş plazma kütle spektroskopisi (ICP-MS), elektroforetik ışık saçılımı (ELS) ve X-ışını fotoelektron spektroskopisi (XPS) dahil olmak üzere çeşitli tekniklerle karakterize edildi. Altın nanoçubukların yüzeyi, ligand değişim metodu ile biyoyumlu bir polimer olan poli(etilen glikol) (PEG) ile modifiye edildi. Altın nanoçubukların sitotoksitesi, hücre alımı ve fototermal etkileri, insan prostat kanser (DU 145) ve epitel (RWPE-1), meme kanser (MCF7) ve epitel (MCF 10A) hücre hatları kullanılarak *in vitro* hücre kültürü deneyleri ile araştırıldı. Hücre canlılığı ve fototermal etki açısından boy-en oranı 4 olan altın nanoçubukların boy-en oranı 7 olandan daha üstün olduğu sonucuna varıldı. Ayrıca, DU 145 ve MCF7 kanser hücrelerinin plazma zarı üzerinde spesifik bir sialik asit türevini hedef alan bir antikor, altın nanoçubuklara konjuge edildi. Konjugasyonlar aynı teknikler ile karakterize edildi ve *in vitro* sitotoksite ve hücre alımı deneyleri ile araştırıldı. Antikor ile konjuge altın nanoçubuklar prostat kanseri hücrelerini seçici hedefleme yeteneği göstermiştir.

Ek olarak, lipit stabilize edilmiş altın nanoçubuklar ve altın nanoçubukları içeren lipit stabilize edilmiş nanobalonlar (AuNBs) ilk kez sentezlendi ve UV-Vis/NIR spektroskopisi, SEM, ICP-MS ve ELS yöntemleri kullanılarak karakterize edildi. Katyonik, toksik yüzey aktif madde yerine çeşitli lipit karışımları kullanılarak lipit stabilize altın nanoçubuklar başarıyla sentezlendi. Ayrıca, altın nanobalonlar sonikasyon ve gaz akışı altında PEG modifiye altın nanoçubukların DPPC: DSPE-PEG lipit filmi ile birleştirilmesiyle sentezlendi. Altın nanobalonlar boy-en oranı 4 olan altın nanoçubuklara göre, hücre tiplerine bağlı olarak önemli ölçüde daha düşük veya aynı toksisite ve 808 nm lazer ışınması altında aynı fototermal etki gösterdi.

TABLE OF CONTENT

LIST OF FIGURES	ix
LIST OF TABLES.....	xv
CHAPTER 1. INTRODUCTION.....	1
CHAPTER 2. LITERATURE REVIEW	3
2.1. Gold Nanostructures: Shape and Properties	3
2.2. Synthesis Methods for Gold Nanorods.....	5
2.3. Optical Properties of Gold Nanorods.....	8
2.4. Growth Mechanism of Gold Nanorods via Seed Mediated Technique	11
2.5. Functionalization of Gold Nanorods.....	15
2.6. Potential Applications of Gold Nanostructures as Cancer Theranostics	18
2.7. Photothermal Therapy.....	23
CHAPTER 3. MATERIALS AND METHODS	29
3.1. Materials	29
3.1.1. Chemicals	29
3.1.2. Instruments	30
3.1.2.1. UV-Visible / Near IR Spectrophotometer.....	30
3.1.2.2. Electrophoretic Light Scattering (ELS)	30
3.1.2.3. Scanning Electron Microscopy (SEM)	31
3.1.2.4. Atomic Force Microscopy (AFM)	31
3.1.2.5. X-Ray Photoelectron Spectroscopy (XPS)	31
3.1.2.6. Inductively Coupled Plasma Mass Spectroscopy (ICP-MS)	32
3.2. Methods.....	32
3.2.1. Synthesis of Gold Nanorods (AuNRs)	32
3.2.2. Surface Modification of AuNRs.....	34
3.2.2.1. Modification of AuNRs with Poly(ethylene glycol) (PEG).....	34
3.2.2.2. Antibody Conjugation of AuNRs.....	34
3.2.2.3. Labelling of AuNRs	34

3.2.3. Lipid-stabilized AuNRs Synthesis	35
3.2.4. The Synthesis of AuNBs	37
3.2.5. Determination of Photothermal Effect in Nanostructure Solutions.	39
3.2.6. <i>In vitro</i> experiments.....	40
3.2.6.1. Cell culture	40
3.2.6.2. Cytotoxicity assays via MTT	40
3.2.6.3. Photothermal Therapy	41
3.2.6.4. Cell Uptake.....	41
CHAPTER 4. RESULTS AND DISCUSSION.....	43
4.1. Synthesis and <i>In vitro</i> Evaluation of Gold Nanorods (AuNRs) at Different Aspect Ratio	43
4.1.1. Synthesis of AuNRs, Modification with PEG and Characterization.....	43
4.1.2. Photothermal Effects of AuNRs	53
4.1.3. <i>In vitro</i> Assessments of AuNRs	57
4.1.3.1. Effect of AuNRs on Cell Viability.....	59
4.1.3.2. Cell Uptake.....	62
4.1.3.3. Photothermal Ablation of Cells.....	64
4.2. Part II: Lipid-stabilized Gold Nanostructures.....	67
4.2.1. Synthesis of Lipid-stabilized AuNRs	67
4.2.2. Synthesis of AuNBs and Characterization	77
4.2.3. Photothermal Effects of AuNBs.....	81
4.2.4. <i>In vitro</i> Assessments of AuNBs	83
4.2.4.1. Effect of AuNBs on Cell Viability.....	84
4.2.4.2. Cell Uptake.....	87
4.2.4.3. Photothermal Ablation of Cells.....	89
4.3. Part III: Cell-Specific Antibody Functionalized AuNRs	91
4.3.1. Antibody Conjugation to AuNRs and Characterization	91
4.3.2. <i>In vitro</i> Assessments of Ab-AuNRs	96
4.3.2.1. Effect of Ab-AuNRs on Cell Viability.....	96
4.3.2.2. Cell Uptake.....	97

CHAPTER 5. CONCLUSION	101
REFERENCES	105
APPENDICES	121

LIST OF FIGURES

<u>Figure</u>	<u>Page</u>
Figure 2.1. Photograph of the Lycurgus cup in (a) reflected and (b) transmitted light, in the British Museum.....	4
Figure 2.2. SEM and TEM images of different shapes and sizes of gold nanostructures: (a) nanoparticles, (b) nanorods, (c) nanobipyramids, (d) hollow interior nanosemishells, (e) hollow interior nanocages, (f) hematite core/Au shell nanorice, (g) nanostars, (h) silica core/Au Shell nanoshells, and (i) nanocubes.	5
Figure 2.3. Different approaches for the synthesis of gold nanorods.	6
Figure 2.4. Schematic representation of AuNRs synthesis with seed-mediated method.....	7
Figure 2.5. (a) Schematic illustration of LSPR excitation for AuNRs and (b) Typical surface plasmon absorption spectrum of AuNRs: longitudinal and transverse plasmon bands corresponding to the electron oscillation along the long axis (Fig. (a) top) and the short axis (Fig. (a) below) of the AuNR respectively.	9
Figure 2.6. Gold nanorods with different aspect ratios have different colors and tunable ultraviolet–visible/near- infrared spectra. (Scale bar: 100 nm).....	10
Figure 2.7. Schematic of seed-mediated AuNRs synthesis with CTAB as surfactant and ascorbic acid as the reducing agent.	12
Figure 2.8. One of the proposed mechanisms that explain the role of silver in the seed-mediated method of gold nanorod synthesis. Underpotential deposition of silver occurs preferentially at the {110} facets of gold, leading to relatively quick growth of other facets until the slower deposition of silver on the end of the rods eventually terminates growth. ..	14
Figure 2.9. (A) Transmission Electron Microscope image of nanorods. (B) A schematic demonstration of crystal structure, growth direction and major planes in nanorods.....	15

<u>Figure</u>	<u>Page</u>
Figure 2.10. Schematics of (A) CTAB stabilized AuNRs, (B) functionalized AuNRs with the completely exchanged of CTAB, (C) functionalized AuNRs with the partially exchanged of CTAB, and (D) secondarily functionalized AuNRs.....	16
Figure 2.11. Various surface functionalization methods of AuNRs. (a) PEGylation and biotin-avidin conjugation; (b) antigen-antibody binding; (c) silica coating; (d) layer-by-layer polyelectrolyte assembly and (e) self-assembly of AuNRs.	17
Figure 2.12. Schematic representation showing the surface modification of CTAB stabilized Gold Nanorods (GNRs) with DMPC liposomes.	19
Figure 2.13. Illustration of light-mediated biomedical applications of modified AuNRs.....	22
Figure 2.14. Schematic illustration of the biological effects of gold nanoparticle-mediated photothermal therapy (PTT).....	24
Figure 2.15. Multifunctional gold coated liposome nanoparticle (Lipos Au NP) in imaging, drug delivery and photothermal therapy PTT.....	27
Figure 2.16. Illustration of synthesis of LiposAu NPs and their photothermal treatment with intracellular DNA damage.....	28
Figure 3.1. Schematic representation of AuNBs synthesis procedure.....	38
Figure 3.2. Experimental setup for photothermal effect measurements of nanostructures.	39
Figure 4.1. UV-Vis / NIR spectra of AuNRs prepared at different aspect ratio.....	45
Figure 4.2. SEM images of AuNRs with (A) AR=2.7, (B) AR=3.2, (C-D) AR=4.0 and (E-F) AR=7.0.	46
Figure 4.3. UV-Vis / NIR spectra of before and after PEG modification of AuNRs with (A) AR=4.0 and (B) AR=7.0. CTAB-stabilized AuNRs (blue spectrum) and PEG-AuNRs (red spectrum).	48
Figure 4.4. SEM images of PEG mixture coated AuNRs with different magnifications.....	49
Figure 4.5. AFM image of PEG modified AuNRs.	50
Figure 4.6. Chemical structures of (A) CTAB, (B) mPEG-thiol and (C) amine-PEG-thiol.	50

<u>Figure</u>	<u>Page</u>
Figure 4.7. XPS spectra showing the C1s and N1s regions of AuNRs and PEGylated AuNRs.....	52
Figure 4.8. Temperature change of AuNR aqueous solutions at varying concentrations with time upon irradiation with 780 nm diode laser (100 mW). (A) AR= 4.0 and (B) AR= 7.0.....	55
Figure 4.9. Temperature change of AuNR aqueous solutions at varying concentrations with time upon irradiation with 808 nm diode laser (200 mW). (A) AR= 4.0 and (B) AR= 7.0.....	56
Figure 4.10. Temperature change of AuNR aqueous solutions at varying concentrations with time upon irradiation with 808 nm diode laser (500 mW). (A) AR= 4.0 and (B) AR= 7.0.....	58
Figure 4.11. Viability of human breast (A) cancer MCF7 and (B) epithelial MCF 10A cells after 24-h incubation with varying doses of AuNRs at two different aspect ratios (AR=4.0 and AR= 7.0).	60
Figure 4.12. Viability of human prostate (A) cancer DU 145 and (B) epithelial RWPE-1 cells after 24-h incubation with varying doses of AuNRs at two different aspect ratios (AR=4.0 and AR= 7.0).	61
Figure 4.13. Uptake of PEGylated AuNRs (AR=4.0 and AR=7.0) by DU 145 prostate and MCF7 breast cancer cells determined by ICP-MS. Data were analyzed by t-test. (n = 3; * p <0.05).....	63
Figure 4.14. The viability of MCF7 human breast and DU 145 human prostate cancer cells incubated with AuNRs (0.2 mM) having an AR (4.0) after exposure to laser light at 808 nm (500 mW) for 15 mins. Control is the cells only. Data were analyzed by t-test. (n = 3; * p <0.05).....	65
Figure 4.15. The viability of MCF7 human breast and DU 145 human prostate cancer cells incubated with AuNRs (0.2 mM) having an AR (7.0) after exposure to laser light at 808 nm (500 mW) for 15 mins. Control is the cells only. Data were analyzed by t-test. (n = 3; * p <0.05).....	65
Figure 4.16. The viability of MCF7 human breast and DU 145 human prostate cancer cells incubated with AuNRs (0.5 mM) having an AR (4.0) after exposure to laser light at 808 nm (500 mW) for 15 mins. Control is the cells only. Data were analyzed by t-test. (n = 3; * p <0.05).....	66

<u>Figure</u>	<u>Page</u>
Figure 4.17. Chemical structures of DDAB, POPC, DPSE-PEG and DPPC.....	68
Figure 4.18. UV-Vis spectra (A-B) and SEM images (C-D) of lipid-stabilized AuNPs prepared using DDAB (A and C) 15 mM in seed and 15 mM in growth, and (B and D) 15 mM in seed solution and 40 mM in growth solution....	69
Figure 4.19. (A) UV-Vis spectra and (B-C) SEM images of lipid-stabilized AuNPs prepared with 1 mM DSPE-PEG.....	70
Figure 4.20. (A) UV-Vis spectrum and (B-C) SEM images of lipid-stabilized AuNRs prepared with DDAB: DSPE-PEG (at a mol ratio of 3:1) mixture.	71
Figure 4.21. (A) UV-Vis spectrum and (B-C) SEM images of lipid-stabilized AuNRs prepared with DDAB: DSPE-PEG (at a mol ratio of 14:1) mixture.	72
Figure 4.22. (A) UV-Vis spectrum and (B-C) SEM images of lipid-stabilized AuNRs prepared with DDAB: POPC (at a mol ratio of 2.7:1) mixture.....	73
Figure 4.23. (A) UV-Vis spectrum and (B-C) SEM images of lipid-stabilized AuNRs prepared with DDAB: POPC (at a mol ratio of 27.3:1) mixture.....	74
Figure 4.24. (A) UV-Vis spectrum and (B-C) SEM images of lipid-stabilized AuNRs prepared with DDAB: POPC: DSPE-PEG (at a mol ratio of 30:1:2.8) mixture.....	75
Figure 4.25. (A) UV-Vis spectrum and (B-C) SEM images of lipid-stabilized AuNRs prepared with DDAB: POPC: DSPE-PEG (at a mol ratio of 40:1:2.8) mixture.....	75
Figure 4.26. (A) UV-Vis spectrum and (B-C) SEM images of lipid-stabilized AuNRs prepared with DDAB: DPPC: DSPE-PEG (at a mol ratio of 30:1:2.8) mixture.....	76
Figure 4.27. Chemical structures of DPPC and DSPE-PEG.	78
Figure 4.28. UV-Vis / NIR spectra of AuNRs (AR= 3.2) before (blue spectrum) and after PEG (Mn 1000 Da) modification (red spectrum), and AuNBs containing AuNRs (green spectrum).	79
Figure 4.29. SEM images of AuNBs containing AuNRs at different magnifications....	80
Figure 4.30. Temperature change of AuNB aqueous solutions at varying concentrations with time upon irradiation with 808 nm diode laser. (A) 200 mW and (B) 500 mW.	82

<u>Figure</u>	<u>Page</u>
Figure 4.31. Viability of human breast (A) MCF7 cancer and (B) MCF 10A epithelial cells after 24-h incubation with varying doses of AuNBs.....	85
Figure 4.32. Viability of human prostate (A) DU 145 cancer and (B) RWPE-1 epithelial cells after 24-h incubation with varying doses of AuNBs.....	86
Figure 4.33. Cell uptake histogram examples of MCF 10A breast epithelial and MCF7 cancer cells after 1 h incubation with fluorescent-labeled AuNBs.	87
Figure 4.34. Cell uptake histogram examples of RWPE-1 prostate epithelial and DU 145 prostate cancer cells after 1 h incubation with fluorescent-labeled AuNBs.	88
Figure 4.35. The viability of (A) MCF7 breast and (B) DU 145 prostate cancer cells incubated with AuNBs after exposure to laser light at 808 nm (500 mW) for 15 mins. Control is the cells only. Data were analyzed by t-test. (n = 3; * p <0.05).	90
Figure 4.36. UV-Vis /NIR spectra of PEGylated AuNRs, before (blue spectrum) and after Ab conjugation (red spectrum).....	92
Figure 4.37. XPS spectra showing the C1s and N1s regions of PEGylated AuNRs and Ab-AuNRs.	95
Figure 4.38. Viability results of (A) MCF7, (B) MCF 10A, (C) DU 145 and (D) RWPE-1 after 24 h incubation with PEGylated and Ab-conjugated AuNRs.	97
Figure 4.39. Uptake of fluorescent-labeled PEGylated AuNRs and fluorescent-labeled Ab conjugated AuNRs by MCF 10A breast epithelial and MCF7 breast cancer cells determined by flow cytometry.....	98
Figure 4.40. Uptake of fluorescent-labeled PEGylated AuNRs and fluorescent-labeled Ab conjugated AuNRs by RWPE-1 prostate epithelial and DU 145 prostate cells determined by flow cytometry.....	99
Figure A1. Cell number determination results of (A) MCF7 and (B) MCF 10A cells after 24 h incubation with varying cell concentrations.....	119
Figure A2. Cell number determination results of (A) DU 145 and (B) RWPE-1 cells after 24 h incubation with varying cell concentrations.....	120

<u>Figure</u>	<u>Page</u>
Figure B1. SEM images of AuNBs containing AuNRs with AR of 4.0 (A-B) and 7.0 (C-D).....	121
Figure B2. SEM images of AuNBs without applying nitrogen gas during the synthesis.....	122
Figure C1. Cellular uptake histograms of MCF 10A breast epithelial and MCF7 breast cancer cells. Top: untreated, Middle: after incubation with fluorescent-labeled PEGylated AuNRs for 1 h and Bottom: after incubation with fluorescent-labeled Ab-AuNRs for 1 h.....	123
Figure C2. Cellular uptake histograms of RWPE-1 breast epithelial and DU 145 breast cancer cells. Top: untreated, Middle: after incubation with fluorescent- labeled PEGylated AuNRs for 1 h and Bottom: after incubation with fluorescent-labeled Ab-AuNRs for 1 h.....	124

LIST OF TABLES

<u>Table</u>	<u>Page</u>
Table 3.1. Synthesized AuNRs used in experiments.	33
Table 3.2. Lipids and concentrations used in the preparation of lipid-stabilized AuNRs.	36
Table 4.1. AuNR synthesis yields measured by ICP-MS.	47
Table 4.2. Zeta potential measurement of AuNRs (CTAB-stabilized) before and after PEGylation (n=3).	51
Table 4.3. Elemental composition and atomic percentages of AuNRs and PEGylated AuNRs obtained by XPS.	53
Table 4.4. IC ₅₀ values of AuNRs with different ARs (4.0 and 7.0) for each cell line.	62
Table 4.5. Zeta potential measurements of PEGylated AuNRs and AuNBs containing AuNRs (n=3).	81
Table 4.6. IC ₅₀ values of AuNBs and AuNRs (AR=4.0) for each cell line.	84
Table 4.7. Zeta potential measurements of AuNRs, PEGylated AuNRs and Ab- conjugated AuNRs (n=3).	93
Table 4.8. Elemental composition and atomic percentages of PEGylated AuNRs and Ab-AuNRs obtained by XPS.	96

CHAPTER 1

INTRODUCTION

Gold nanostructures due to their controllable size, shape, surface functionality, light absorption in the NIR region and scattering properties are extensively investigated as biocompatible structures that can be used in diagnosis and treatment of disease (Kim et al., 2009; Papavassiliou, 1979; Prasad et al., 2005). In particular, gold nanostructures have the ability to convert light into heat and specifically target specific tissue and cell types, which makes it very advantageous in cancer treatment compared to conventional radiotherapy and chemotherapy methods, which also damage cancer cells along with healthy cells (Oyelere et al., 2010). Gold nanorods and nanobubbles containing gold nanorods produce more heat energy as compared to nanoparticles because of their longitudinal surface plasmons which are more affected by the changes in the surrounding dielectric field (Carpin et al., 2011; Link and El-Sayed, 1999). Therefore, in this thesis, gold nanorods and nanobubbles structures containing multiple gold nanorods were preferred.

Breast cancer is the most common type of cancer in women in Turkey and in the world (Curado, 2011). Prostate cancer is the most common type of cancer in men in the world and it ranks second after lung cancers in Turkey (Jemal et al., 2008; American Cancer Society, 2018). It is needed that an effective diagnosis and treatment methods to reduce the health and socioeconomic effects of these two types of cancer.

In the literature, it is possible to encounter many examples of cancer diagnosis and treatment studies performed with gold nanorods (Kiziltepe et al., 2012; Rosi and Mirkin, 2005; Tong et al., 2007; Dickerson et al., 2008; Tsai et al., 2013). In one study, gold nanorods were used to transport paclitaxel for the treatment of breast cancer. The obtained results showed that the gold nanorod based transport system successfully released the paclitaxel in MCF7 breast cancer cell line (Kuo et al., 2010).

However, active-targeted gold nanostructures take part in relatively fewer studies (Kumar et al., 2011; Xiao et al., 2012; Jin et al., 2012). Researching new molecules that can separate cancer cells from healthy cells has an important place in cancer diagnosis and treatment studies. In this context, non-commercially available antibodies that are

capable of targeting specific sialic acid derivative cell receptors at a very low level in healthy tissue in comparison to cancerous tissue were conjugated to gold nanorods. The use of this selective antibody to breast and prostate cancer cells significantly enhances the efficacy and specificity of diagnostic and treatment nanosystems of gold nanorods. In addition, there is no study on the production or treatment of nanobubble structures containing more than one gold nanorods produced for the first time in this thesis.

This thesis focuses on developing new nanostructures which are biocompatible materials. For this purpose, the preparation of gold nanostructures and their functionalizations were carried out. *In vitro* experiments such as cytotoxicity, cell uptake and photothermal treatments were conducted. A series of analyses were performed by UV-Vis/NIR spectroscopy, Scanning Electron Microscopy (SEM), Atomic Force Microscope (AFM), X-Ray Electron Spectroscopy (XPS), Electrophoretic Light Scattering (ELS), Inductively coupled Plasma Mass Spectroscopy (ICP-MS) and Flow Cytometry. The second chapter describes the literature review. Chapter 3 and 4 give the experimental methods and results of the experiments performed throughout the study, respectively. Chapter 5 summarizes the conclusions and future recommendations.

CHAPTER 2

LITERATURE REVIEW

2.1. Gold Nanostructures: Shape and Properties

Noble metals nanostructures have received a great deal of interest for their optical and plasmonic properties. The plasmonic properties of nanostructures have been one of the most amazing and dynamic research areas in the field of nanotechnology. The excitation of surface plasmons on metallic nanostructures provides ways to control electromagnetic waves and to adapt light-matter interactions at the nanoscale (Ye et al., 2012). Their optical properties relying on size and shape have introduced a remarkable potential in many applications such as optics (Zijlstra et al., 2009), materials science and plasmonics (Atwater and Polman, 2010), bioimaging and therapeutics (Huang et al., 2006; Xue et al., 2011), drug delivery (Wijaya et al., 2009), and nanomedicine and biosensors (Kabashin et al., 2009; Wang et al., 2010) (Tomak, 2013).

In the 4th century AD, colloidal gold was used as a method of staining glass. A famous example is the Lycurgus cup, which is red in transmitted light and green in reflected light (Figure 2.1). In 1857, Faraday reported that the brilliant colors of these glasses are due to the colloidal nature of AuNPs (Boisselier and Astruc, 2009; Pollard and Heron, 2008).

Various methods using appropriate techniques for the synthesis of gold particles were reported in the 20th century. In 1951, Turkevitch et al. introduced a method for preparation of colloidal gold using citrate reduction, which is still used today. There are a large number of ways to synthesize AuNPs, most of which start from commercial HAuCl₄.

Among the metal particles, gold, one of the noble metals, is the most preferred since it is non-toxic and resistant to corrosion and oxidation. Due to these properties, gold has been used in medicinal applications for centuries. It also has unique properties due to its size and shape (Rejiya et al., 2012). Gold nanoparticles (AuNPs) are easily characterized by the presence of surface plasmon resonance (SPR) bands. Also, AuNPs

are easily functionalized with the help of polymers, oligonucleotides, antibodies and proteins to achieve biocompatibility. They are also preferred because they can be easily synthesized by inexpensive methods such as wet chemistry. During the synthesis, the reaction parameters can be changed, and their size can vary between 2-500 nm.

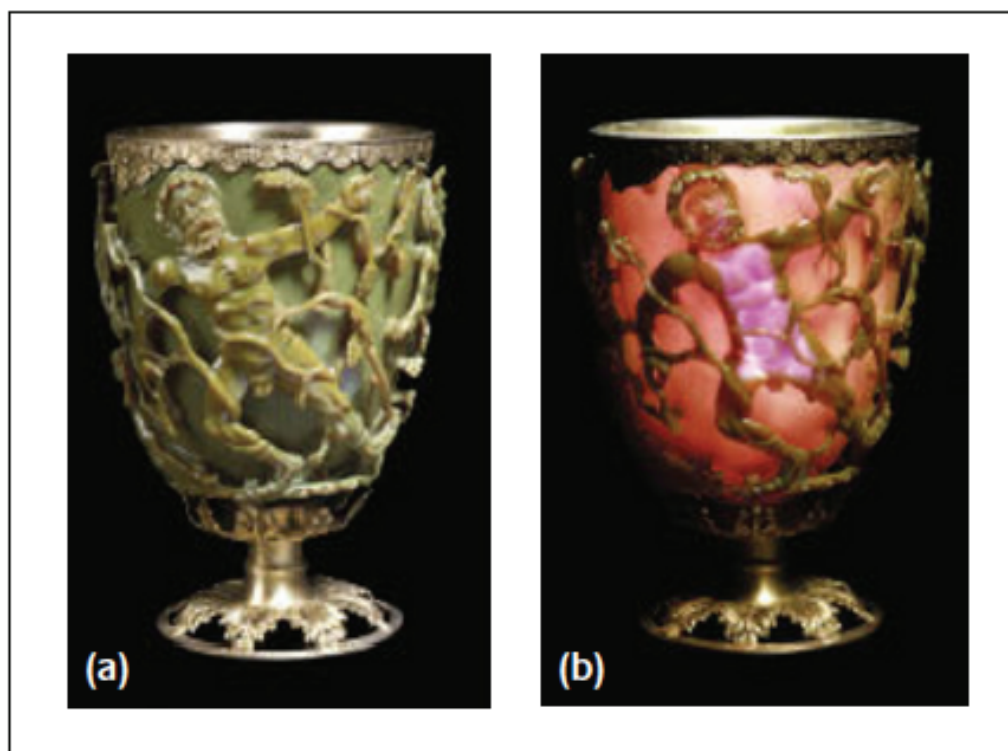


Figure 2.1. Photograph of the Lycurgus cup in (a) reflected and (b) transmitted light, in the British Museum.

(Source: Freestone et al., 2007)

It is reported that not only AuNPs but also gold nanostructures in different forms (e.g. spherical, rod, plate, hexagonal shape, wires, triangles and core-shell structures) were synthesized by various methods (Figure 2.2). Particularly, among these nanostructures, gold nanorods (AuNRs) have been extensively studied due to their easy synthesis, control over the aspect ratio (the ratio of the length to the width) and potential applications (Daniel and Astruc, 2003; Park, 2006). In particular, AuNRs with controlled aspect ratio in the range of 2–6 have been synthesized using the micelle-templated seed and feed technique developed by the groups of Murphy (2008) and El-Sayed (2008), and

the Halas' group (2008) has developed the synthesis of gold nanoshells (AuNSs) composed of a silica core surrounded by a thin Au layer (Boisselier and Astruc, 2009).

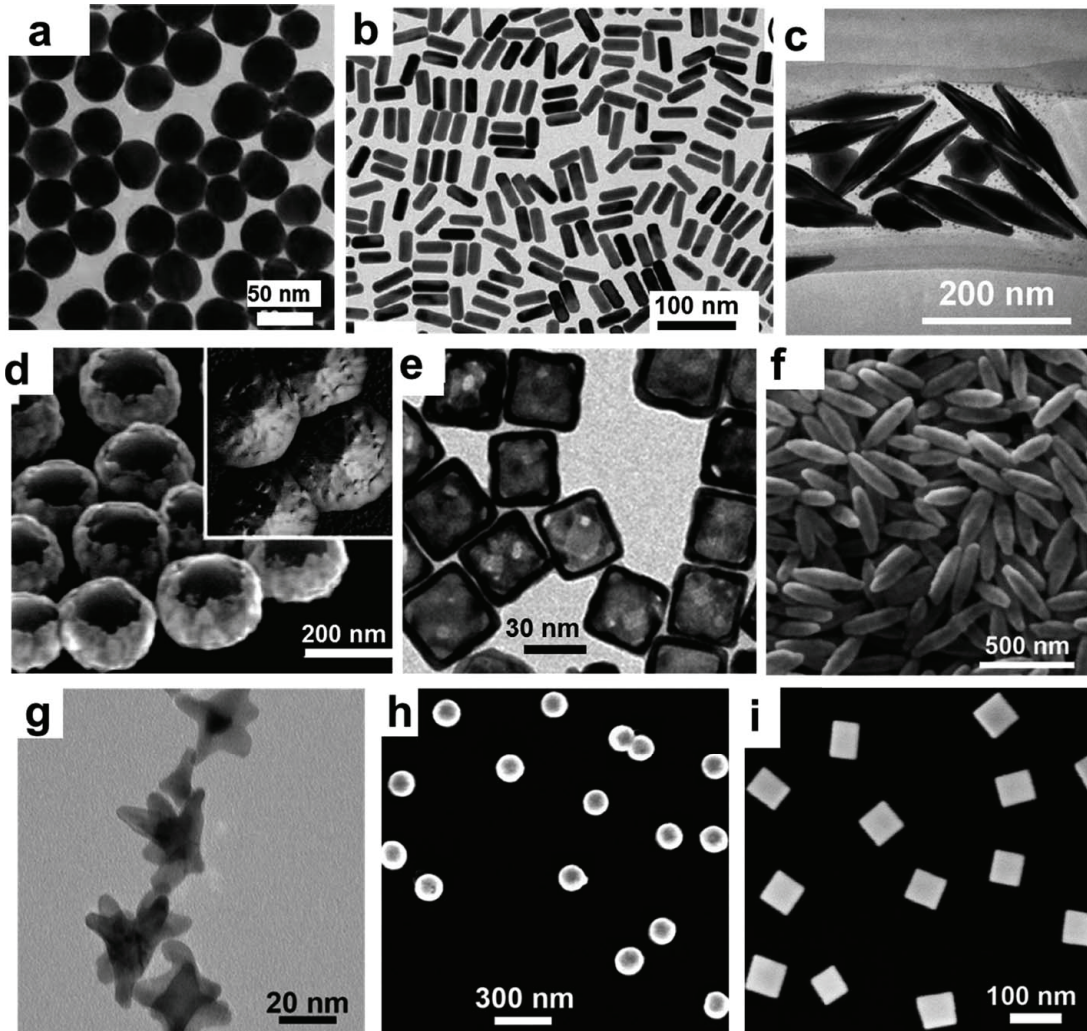


Figure 2.2. SEM and TEM images of different shapes and sizes of gold nanostructures: (a) nanoparticles, (b) nanorods, (c) nanobipyramids, (d) hollow interior nanosemishells, (e) hollow interior nanocages, (f) hematite core/Au shell nanorice, (g) nanostars, (h) silica core/Au Shell nanoshells, and (i) nanocubes. (Source: Webb and Bardhan, 2014)

2.2. Synthesis Methods for Gold Nanorods

Different approaches have been developed in the literature for the synthesis of AuNRs (Figure 2.3). The first developed method for the production of AuNRs was the

template method found by Foss Jr. et al. (1994). However, the disadvantage of this method is that the production efficiency is low. The second synthesis approach is the electrochemical method first reported by Yu et al. (1997). However, the control of the electric field makes this method more complex and difficult.

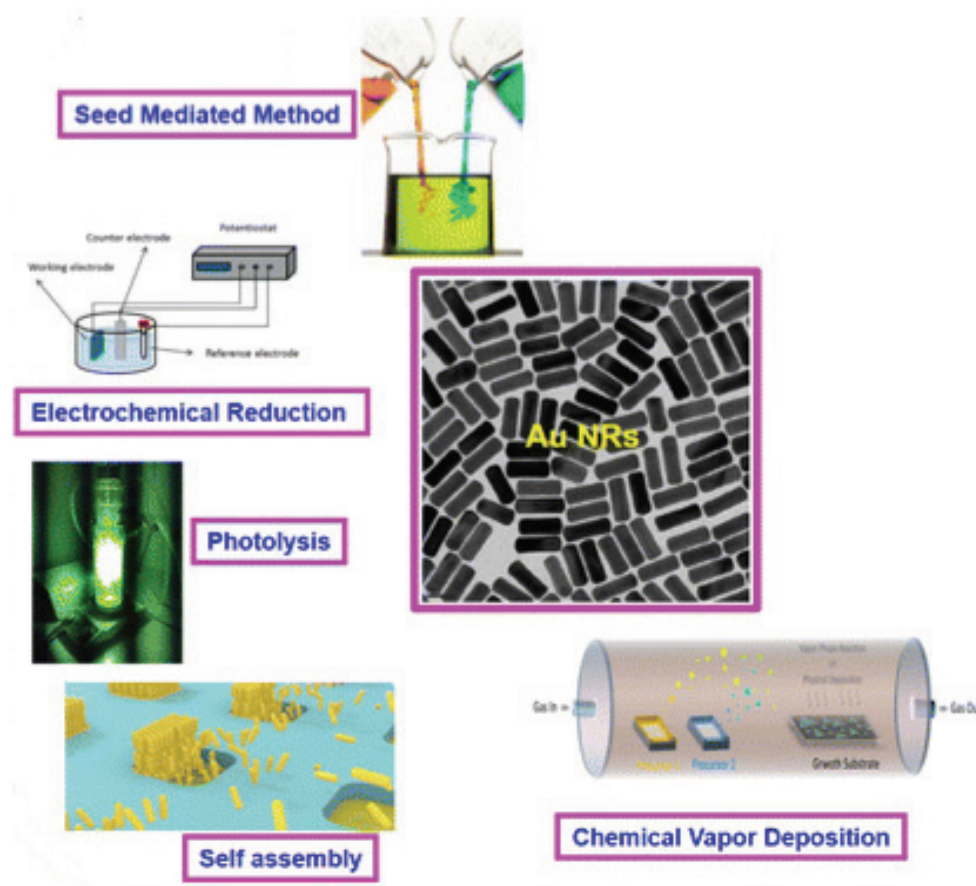


Figure 2.3. Different approaches for the synthesis of gold nanorods.
(Source: Alagiri et al., 2011)

The photochemical approach to the production of AuNRs was first demonstrated by Kim et al. (2002). This process has some similarities with the electrochemical approach. The main difference is the use of UV light to allow reduction reactions. In the photochemical method, nanoparticles and AuNRs are formed in the same solution. This results in the formation of many nanoparticles and few AuNRs. Esumi et al. (1995) used the photochemical reduction in the presence of cetyltrimethylammonium chloride to develop gold nanostructures.

The most commonly used method for the synthesis of AuNRs with high efficiency is the seed-mediated method, also known as the wet chemical method (Figure 2.4). This method has been studied by many authors and its steps have been developed. Gole and Murphy (2004) introduced a seed-mediated approach in which AuNPs are used as seeds to grow AuNRs. El-Sayed and coworkers showed that the efficiency of the reaction, as well as the control of the AuNR anisotropy, can be increased using Ag(I) during rod formation. This method makes it possible to produce AuNRs at low cost. It is also possible to prepare the compositions, shapes and sizes of the nanoparticles by controlling each step very well (Perez-Juste et al., 2005).

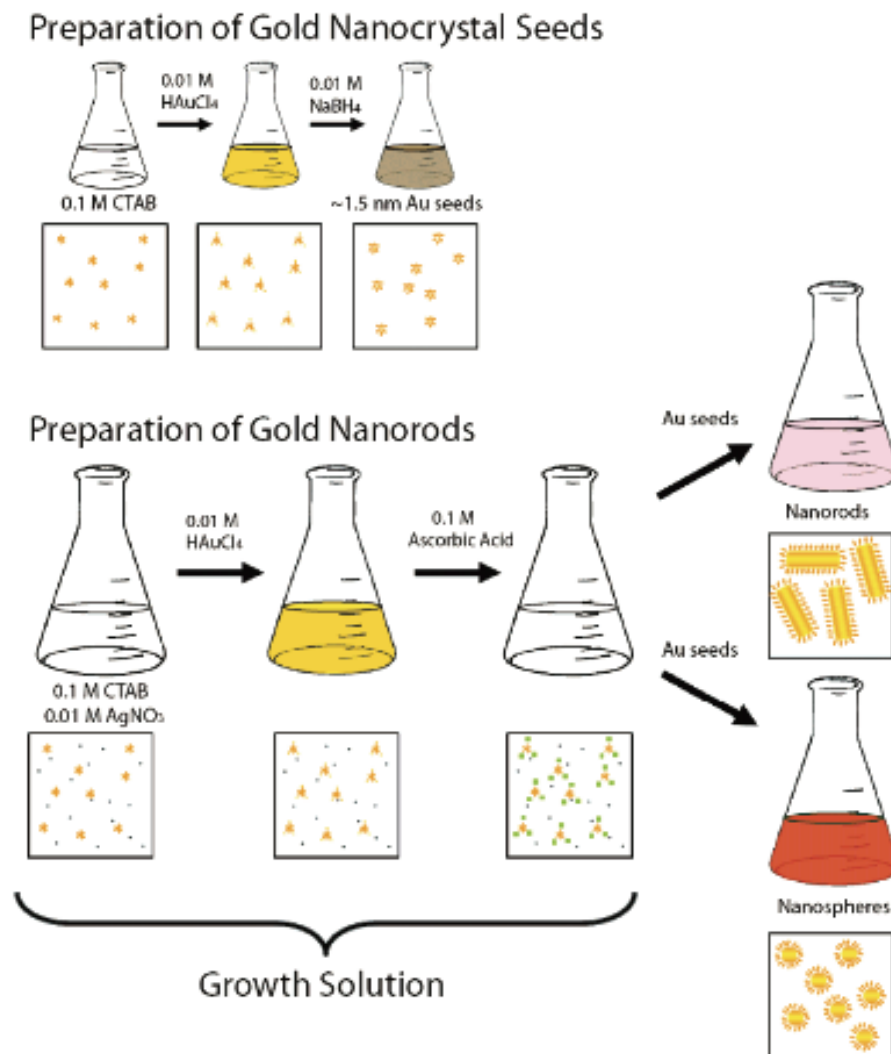


Figure 2.4. Schematic representation of AuNRs synthesis with seed-mediated method. (Source: Smith and Korgel, 2008)

In particular, AuNRs growth mechanism was analyzed by the presence of the cetyltrimethylammonium bromide (CTAB) by Murphy and co-workers, and this method has become very popular. Gao et al. (2003) also illustrated that the shape of AuNRs depends on the changes of the surfactant. They examined C₁₆TAB with different length and tail groups and demonstrated that these changes in length are critical for the production of AuNRs.

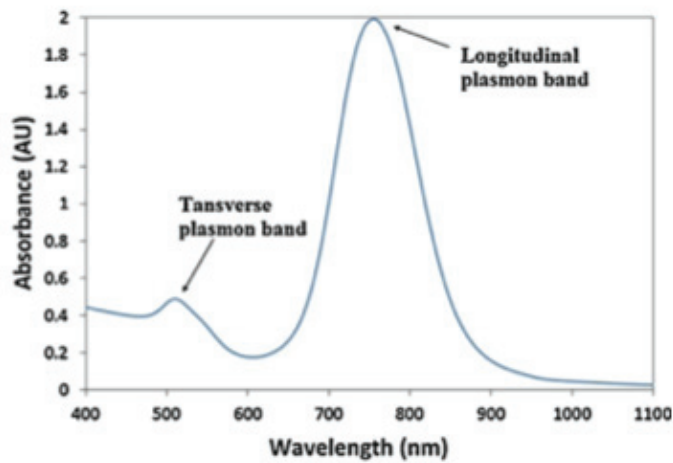
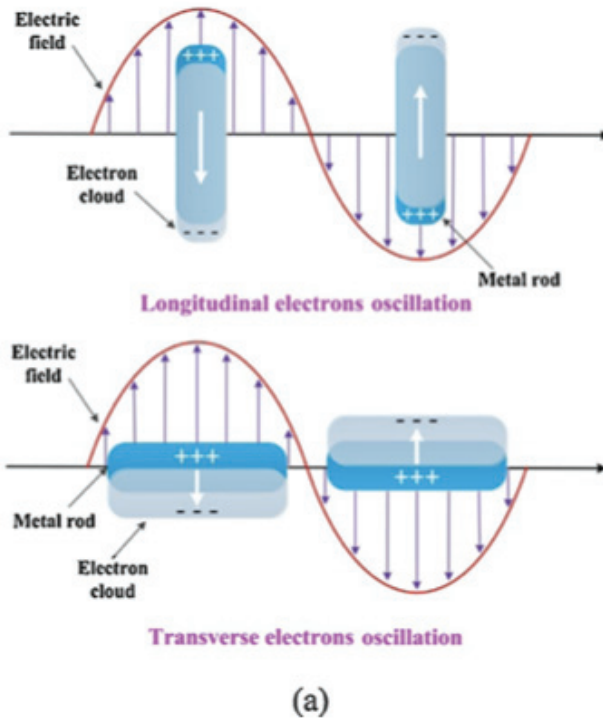
Nikoobakht and El-Sayed (2003) produced AuNRs with different aspect ratios in solution by changing the amount of silver nitrate for a given amount of gold. They showed that AuNRs with high yield depended on surfactant-stabilized Au seeds. Later Sau and Murphy (2004) extended this study to produce a very high yield of short AuNRs with average lengths of 20 to 100 nm. They also found that the various reaction parameters can directly affect AuNRs dimension. They also reported that ascorbic acid plays an important role in aspect ratios of AuNRs.

Jana (2005) developed a new method for the synthesis of AuNRs in which seed solution is not necessary. He introduced a mixture of strong and weak reducing agents into the micellar solution of a metal salt, where the strong reducing agent initiates nucleation and the weak reducing agent helps the nanoparticles to grow.

2.3. Optical Properties of Gold Nanorods

AuNRs typically show two plasmon resonance bands. The first is the transverse resonance, which is attributed to the diameter of AuNRs, whereas the length of AuNRs presents the longitudinal resonance, as illustrated in Figure 2.5. The spherical AuNPs have only a single plasmon band. These absorption bands occur when the incident photon frequency is resonant with the collective oscillation of the free electron cloud of the particle and is known as “Localized Surface Plasmon Resonance (LSPR)” (Chen et al., 2007).

The optical property of AuNPs is dependent on the size, surrounding environment, and the shape of the nanoparticles. The aspect ratio in AuNRs is the value of the longitude divided by the width and energy separation between the resonance frequencies of the long and short bands changes by increasing the aspect ratio (Link and El-Sayed, 2000).



(b)

Figure 2.5. (a) Schematic illustration of LSPR excitation for AuNRs and (b) Typical surface plasmon absorption spectrum of AuNRs: longitudinal and transverse plasmon bands corresponding to the electron oscillation along the long axis (Fig. (a) top) and the short axis (Fig. (a) below) of the AuNR respectively. (Source: Cao et al., 2014)

It is known that the spectral location of the plasmon resonance can be adjusted by altering the aspect ratio of AuNRs. AuNRs with varying aspect ratios create different-colored nanorod solutions due to different interactions with light in the spectrum (Figure 2.6) (Vines et al., 2019).

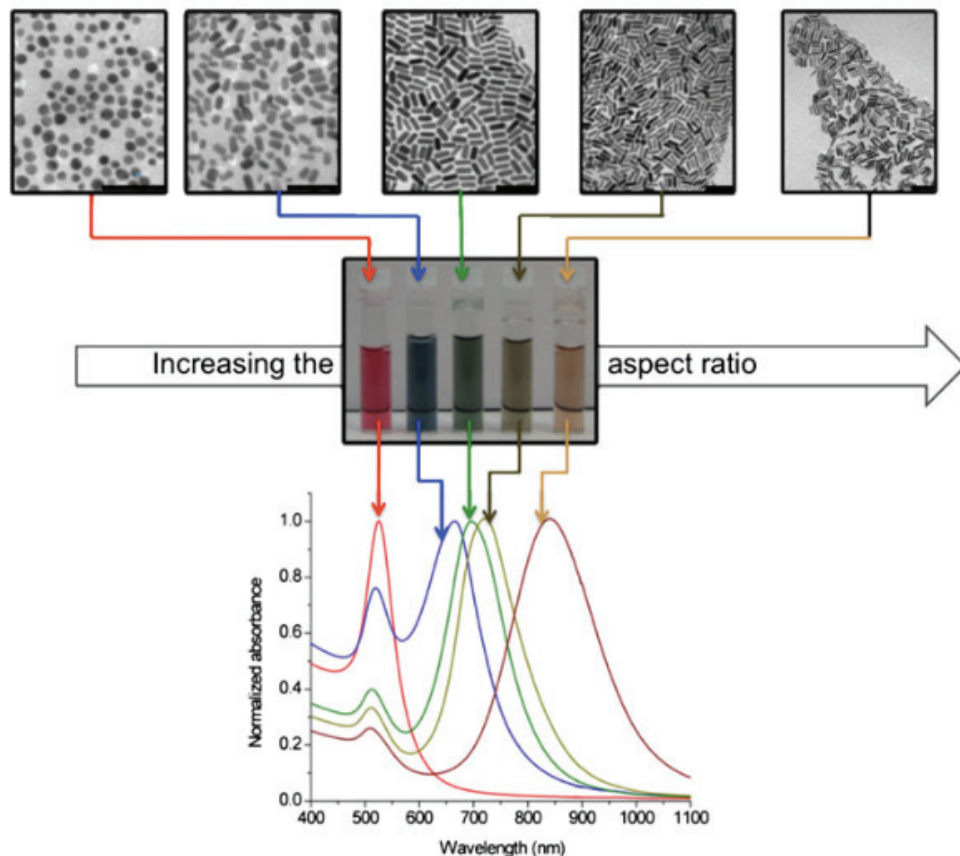


Figure 2.6. Gold nanorods with different aspect ratios have different colors and tunable ultraviolet-visible/near-infrared spectra. (Scale bar: 100 nm). (Source: Alkilany and Murphy, 2010)

AuNRs show different colors depending on the aspect ratio, which allows the gold nanorods to be used in optical applications (Perez-Juste et al., 2005). One of these applications is in the biological area. For instance, AuNRs bind to specific cells with higher affinity, and one can observe the conjugated cell using a simple optical microscope due to the enhanced scattering cross-section (El-Sayed et al., 2005). Also, AuNRs with a high enhancement of the longitudinal plasmon resonance can enhance fluorescence over

bulk metal and can be used in sensor applications (Eustis and El-Sayed, 2005). By increasing the absorption intensity of the surface plasmon resonance, the enhancement of the Raman scattering of molecules adsorbed on AuNRs occurs, which makes AuNRs an excellent candidate for the future of nanoelectronics (Nikoobakht et al., 2002).

2.4. Growth Mechanism of Gold Nanorods via Seed Mediated Technique

The wet chemistry technique was first demonstrated by Jana et al. (2001). In this study, they modified the electrochemical technique using chloroauric acid instead of the gold electrode. While CTAB was also used as a stabilizer, additional chemicals such as acetone and cyclohexane were used to reshape for AuNRs. Ascorbic acid (AA) reduces from Au + 3 to Au + 1 valence as a weak reducing agent. Metallic gold can be fully reduced with seed particles with a diameter of 3 nm (Figure 2.7). Seed particles are formed by the addition of sodium borohydride as a strong reducing agent to the CTAB-chloroauric acid mixture.

External factors such as temperature, additives and pH are the variables that must be controlled during the growth process. Zweifel and Wei (2005) demonstrated that an increase in the amount of Na₂S in the growth solution can directly reduce the optical drift in AuNRs. The sulfide treatment further enhances the dielectric function at the surface of the nanorod which leads the plasmon resonances to shift toward longer wavelengths. AuNRs after treatment with sulfide is stable at room temperature. In one study, it was reported that the addition of NaOH, which increases the pH of the solution, is crucial for the formation of nanorods with high aspect ratio in the seed-mediated method (Busbee et al., 2003). Another study by Wu et al. (2005) illustrated that the addition of nitric acid to seed-mediated solution leads to monodispersity and a higher aspect ratio of AuNRs.

Jana (2005) demonstrated that CTAB micelles break down at high temperatures and AuNRs cannot be produced; that is why they indicated that AuNRs only form at temperatures below 50 °C. Pe´rez-Juste et al. (2004) also reported the same hypothesis that temperatures of reaction must be close to room temperature for higher AuNR yields. Zijlstra et al. (2006) reported that the temperature of AuNRs solution can increase up to 90°C in the seedless method without a breakdown of the formation of the micelles.

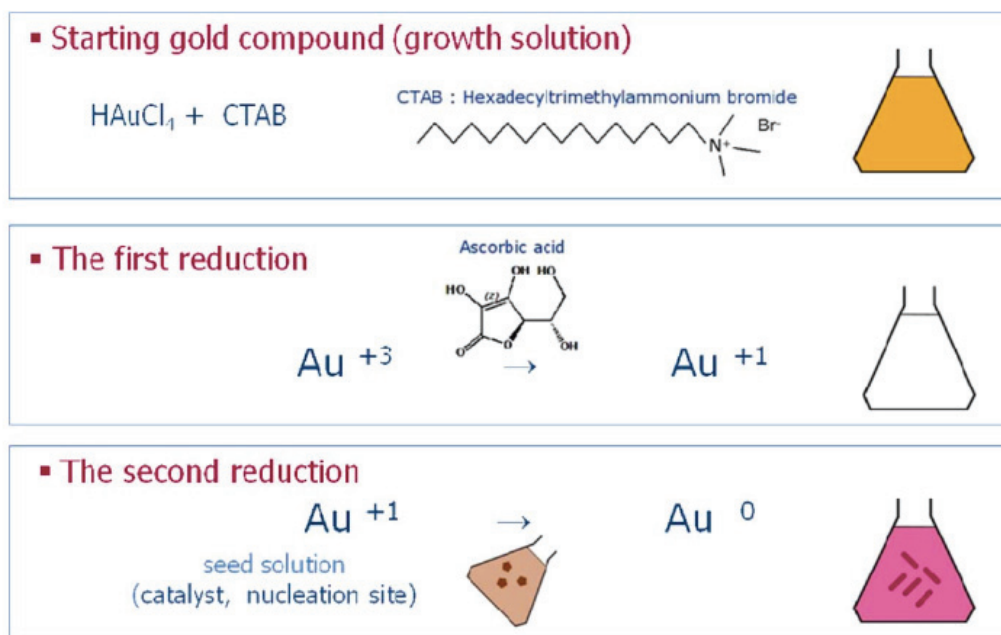


Figure 2.7. Schematic of seed-mediated AuNRs synthesis with CTAB as surfactant and ascorbic acid as the reducing agent.

(Source: Sharma et al., 2009)

It was found that the growth process under high-temperature conditions led to the production of high aspect ratio AuNRs. Perez-Juste et al. (2005) observed that decreasing the temperature and CTAB concentration caused low aspect ratio AuNRs (Hubert et al., 2010). In addition, changing the concentration of reactants during the growth process led to the production of AuNRs with various lengths and diameters (Vidgerman et al., 2012).

Although the seed-mediated method has advantages over other methods, scientists working on AuNRs have doubts about the precise growth mechanism (Sau and Murphy, 2004). In the first step, spherical Au nanoparticles (2–3 nm) are produced in the seed solution, usually in the presence of a strong reducing agent such as NaBH_4 . In the second step, these seed particles are added to the growth solution ordinarily containing Au ions, growth directional agents (CTAB and AgNO_3) and a mild reducing agent (ascorbic acid). Also, there are many studies producing AuNRs using sodium citrate instead of CTAB, but no high yield is observed (Gole and Murphy, 2004). Briefly, the experimental results suggest that CTA^+ ions from the surfactant and Au(III) ions from HAuCl_4 form a $\text{CTA}^+ - \text{Au(III)}$ complex. Ascorbic acid (AA) instantly reduces this complex to form $\text{CTA}^+ - \text{Au(I)}$ (Chhatre et al., 2018). It is widely known that AA reduces Au(III) to Au(I) in the

growth solution. In addition, studies indicate that AA changes the shape of AuNRs (Scarabelli et al., 2013). Finally, the addition of the seed particles to the growth solution provides a catalytic effect for the complete reduction of Au. However, seed solution is used immediately after formation. As seeds lose their catalytic activity, the diameter of AuNRs increases and the growth is inhibited (Park et al., 2013).

There are some different ideas on the growth mechanism for the synthesis of anisotropic AuNRs using AgNO_3 , CTAB and AA, so it is still under debate. One investigation showed that when CTAB is added to a HAuCl_4 solution, chloride ions in the Au precursor are replaced by bromine ions via ligand exchange. Chen et al. (2013) also noticed that the addition of AA to the growth solution containing HAuCl_4 and CTAB reduce Au ions from the +3 to the 0 state. These gold clusters surrounding CTAB protect them from agglomerating. Then, the gold seeds are added to this solution and this leads to the growth of AuNRs. However, this explanation disagrees with some other studies that AA can only reduce Au ions from the +3 to the +1 state because of a weak reducing agent. Also, various mechanisms for AgNO_3 in the growth of AuNRs have been indicated such as facet-specific deposition of AgBr , under-potential deposition (UPD) of Ag on various facets, and formation of a $\text{CTA}^+\text{AgBr}_2^-$ complex (Ahmed et al., 2014).

A detailed study demonstrated that silver is present in the metallic rather than ionic form and also several layers of metallic silver are observed on the surface of AuNRs. The presence of metallic silver on AuNRs is driven by UPD of silver. According to this different growth mechanism, Ag(I) from AgNO_3 cannot be reduced by AA in the growth solution. However, the silver on the gold surface deposits on the $\{110\}$ facets compared to the $\{100\}$ facets at lower potential. Since re-oxidation of silver requires slow growth along the $[110]$ direction, the unexpected growth happens along the more stable $[100]$ direction (Vigderman et al., 2012) (Figure 2.8).

The addition of Ag ions disturbs the CTAB surrounding the gold leading to the nucleation of metallic Au, and this will influence the zipping of the CTAB bilayer. Some crystals grow along the $[100]$ direction, and also the side faces made of $\{100\}$ or $\{110\}$ facets grow (Figure 2.9). CTAB makes a good interaction with the high surface energy $\{100\}$ and $\{110\}$ facets rather than the closely packed low energy $\{111\}$ facet. Because the $\{111\}$ facet has the smallest Au–Au atomic distance compared to the $\{100\}$ and $\{110\}$, adsorption of the large head groups of CTAB is favored along the loosely packed facets $\{100\}$ or $\{110\}$ (Chhatre et al., 2018). This anisotropic adhesion of CTAB causes an electrostatic interaction among the growing nanoparticles because CTAB has a

positive charge after losing the Br⁻ ions. The electrostatic interactions in the assembly are affected by increasing the concentration of the CTAB. A better adhesion of CTAB molecules on the growing surface results in the use of high concentration of CTAB, leading to stronger electrostatic interactions (Ahmed et al., 2014). The growing side facets are stabilized by CTAB bilayers in a zipper-like.

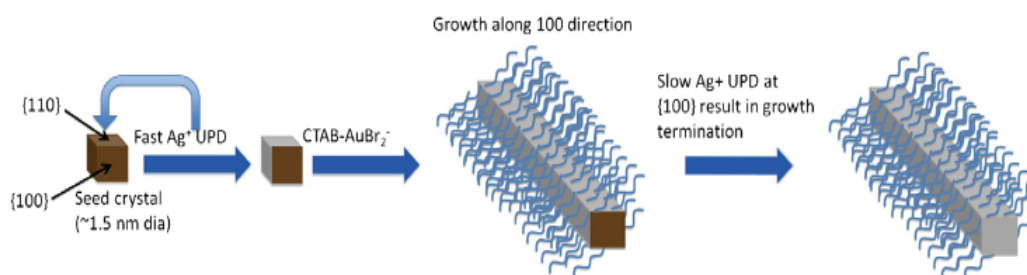


Figure 2.8. One of the proposed mechanisms that explain the role of silver in the seed-mediated method of gold nanorod synthesis. Underpotential deposition of silver occurs preferentially at the {110} facets of gold, leading to relatively quick growth of other facets until the slower deposition of silver on the end of the rods eventually terminates growth.

(Source: Murphy et al., 2011)

In addition to the basic components, various additives such as acetone, cyclohexane, Na₂S, hydrochloric acid or nitric acid, iodide and bromide ions are also used in the growth solution of AuNRs. El-Sayed and Nikoobakht (2003) presented that AuNRs with high aspect ratios were synthesized using a binary surfactant mixture of CTAB and benzyldimethylhexadecylammonium chloride (BDAC) after aging of the growth solutions for 7– 10 days.

Ye et al. (2013) also used a binary surfactant mixture composed of CTAB and sodium oleate (NaOL) in the growth solution and produced AuNRs at high yields. The double bond in NaOL molecules slowly reduced HAuCl₄ in the absence of AA, in contrast to common methods in which AuCl₄⁻ CTAB complexes are not reduced until AA is added to the growth solution. Therefore, a small amount of AA is required to reduce Au(I) to Au⁰ state catalyzed by the gold seeds, in this binary surfactant system. Furthermore, not only is NaOL related to the reduction of Au but also NaOL molecules might mediate between CTAB surfactants and certain facets of growing AuNRs.

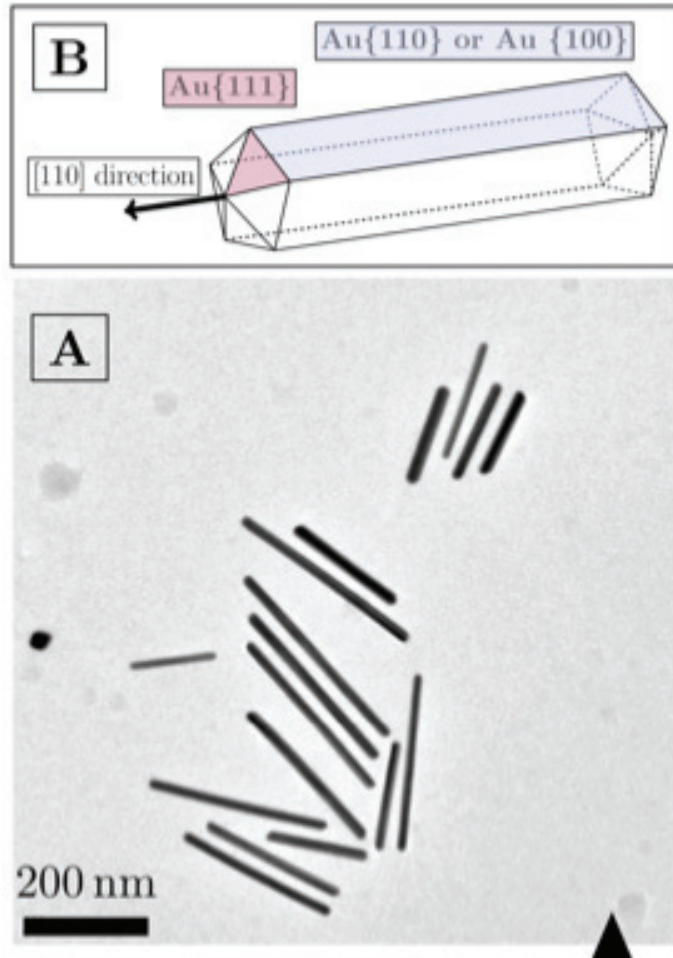


Figure 2.9. (A) Transmission Electron Microscope image of nanorods. (B) A schematic demonstration of crystal structure, growth direction and major planes in nanorods.

(Source: Chhatre et al., 2018)

2.5. Functionalization of Gold Nanorods

In recent years, there has been a considerable increase in the biomedical applications of metal nanoparticles. Nanoparticles that have plasmon resonance by modification with biological molecules provide advantages for both diagnostic and photothermal treatment (Figure 2.10).

During AuNRs synthesis, CTAB was used as a growth control agent. At the same time, CTAB ensures the stabilization of AuNRs. Although CTAB provides stability, it is a highly toxic reagent and disrupts the membrane integrity of living cells. The important thing is to ensure the stability of AuNRs while reducing the toxic effect of CTAB by

removing (Nikoobakht and El- Sayed, 2003). Many ligands or molecules have been used to reduce the toxic effect of AuNRs in their use in biomedical applications. Ligand exchanges using reactants such as biocompatible phosphatidylcholine, polystyrenesulfonate and thiol-terminated polyethylene glycol (PEG) are alternative methods for reducing the toxic effect of CTAB on AuNRs (Takahashi et al., 2006; 2008). Fratoddi et al. (2014) found that molecules including thiol or amine groups could be easily functionalized with AuNPs via the formation of Au-S or Au-N bonds. In addition to PEGylation, layering and silica coating techniques are the most common techniques for the functionalization of AuNRs (Figure 2.11) (Paramasivam et al., 2017).

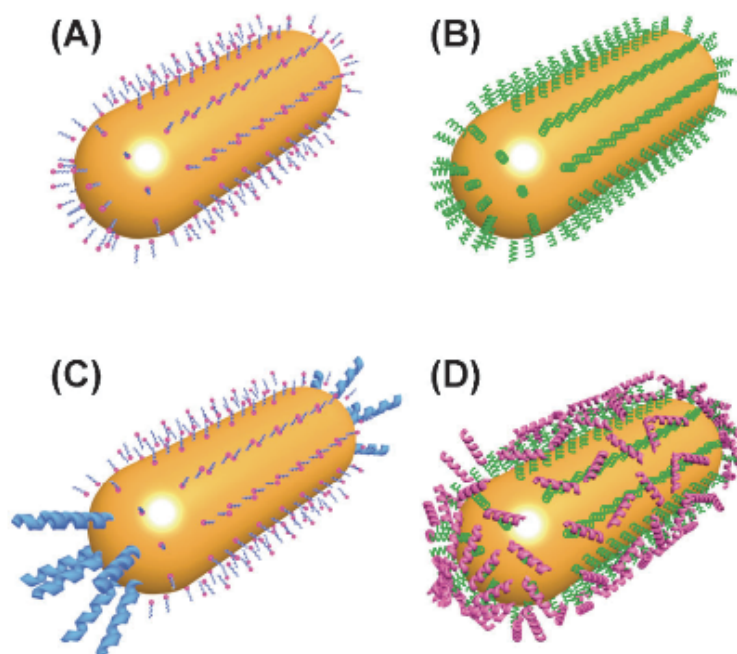


Figure 2.10. Schematics of (A) CTAB stabilized AuNRs, (B) functionalized AuNRs with the completely exchanged of CTAB, (C) functionalized AuNRs with the partially exchanged of CTAB, and (D) secondarily functionalized AuNRs. (Source: Chen et al., 2013)

The most commonly used polymer for surface modification is PEG. The ligand exchange of CTAB slowly occurred with the thiol terminated PEG in pure water due to the strong binding of CTAB on AuNRs. Thus, the coating condition should be controlled to avoid partial functionalization and aggregation of AuNRs. PEGylated AuNRs were found to be stable in serum (Zhang et al., 2014). Thiol terminated PEG makes the

nanoparticles stable not only in phosphate-buffered saline (PBS) but also at high, low pH levels and in neutral environments (Pelicano et al., 2006). Proteolytic enzymes and the reticuloendothelial system (RES) recognize molecules from outside the body and destroy them. PEG coating prohibits recognition by proteolytic enzymes and RES (Roberts et al., 2012; Wang et al., 2009).

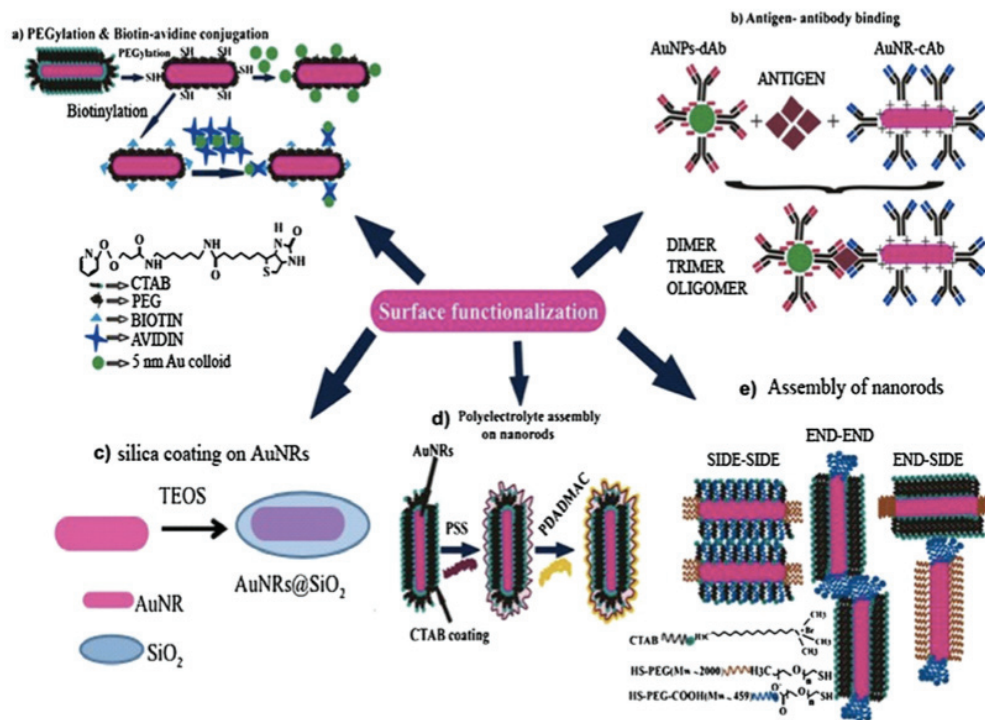


Figure 2.11. Various surface functionalization methods of AuNRs. (a) PEGylation and biotin-avidin conjugation; (b) antigen-antibody binding; (c) silica coating; (d) layer-by-layer polyelectrolyte assembly and (e) self-assembly of AuNRs.

(Source: Parasivam et al., 2017)

Particularly, the functionalization of AuNRs surfaces for their use in the biomedical field is carried out for two reasons: First, gold nanoparticles show an affinity for nonspecific binding with serum proteins in a biological media (Strickland and Batt, 2009). This leads to the formation of undesired larger gold nanoparticle aggregates in biological application. Surface modification of AuNRs with PEG may reduce non-specific protein binding as it increases colloidal stability in the biological environment (Boca and Asteljan, 2010). Secondly, immune system cells can recognize AuNRs which

do not have appropriate surface modifications and eliminate them. This prevents the remaining nanoparticles in the blood circulation from having sufficient time to reach the targeted tissue or cells. Surface modification of AuNRs with PEG prevents the recognition of AuNRs by the immune system and thus extends their half-life in blood circulation (Roberts et al., 2012).

Another technique used for surface functionalization of AuNRs is layering using polyelectrolytes. AuNRs are coated with anionic polyelectrolytes due to positively charged CTAB. The cationic polyelectrolytes are then bound to this layer. The main purpose of using anionic and cationic polyelectrolytes is to reduce their recognition in the biological environment and to make them dispersible (Alkilany et al., 2012; Qiu et al., 2010).

Alternative functionalization methods are also available, including amphiphilic block copolymers and phospholipid coatings (Figure 2.12). However, some limitations arise in these methods, such as poor water solubility in the desired coating agent and low chemical and physical efficiency in the modification (Basiruddin et al., 2010). Lipid-nanoparticles exhibit better biocompatibility than polymeric nanoparticles (Battaglia and Ugazio, 2019).

Also, liposomes have played an important role due to their natural characteristics such as high biocompatibility, large drug-carrying capacity, and convenient and feasible tunability. However, since pure liposomes have poor stability, they are prone to adhere and fuse to form larger ones in suspension. Up to now, nanoparticles-functionalized liposomes, so-called liposomal nanohybrids, have been developed as theranostic nanoscale systems (Zhu et al., 2018).

2.6. Potential Applications of Gold Nanostructures as Cancer Theranostics

According to the World Health Organization (WHO), cancer is one of the largest causes of death worldwide and is expected to increase by 70 % over the next 20 years. Although the variety of cancer treatment methods has increased nowadays, systemic treatment methods such as chemotherapy, hormone therapy, and radiotherapy are not completely effective, and there are side effects such as weakening of the immune system,

tissue and organ damage and anemia. In addition, such treatments affect healthy cells as well as cancer cells. Treatment with surgical procedure is a highly invasive method that can result in complete removal of the organ, and there is a possibility of recurrence of cancer later.

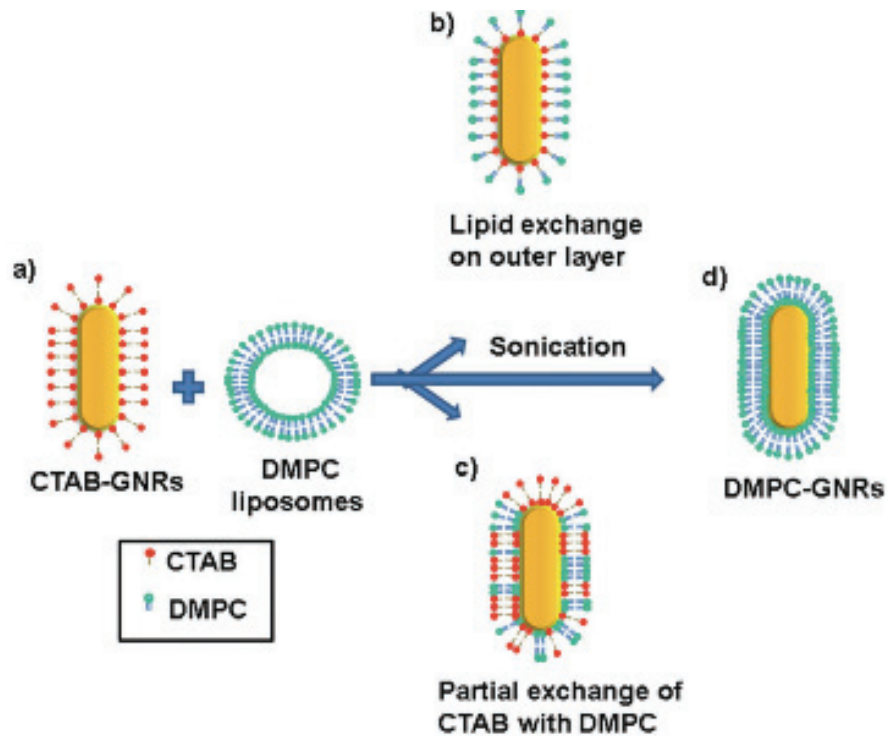


Figure 2.12. Schematic representation showing the surface modification of CTAB stabilized Gold Nanorods (GNRs) with DMPC liposomes.
(Source: Santhosh et al., 2017)

Breast cancer is the most common type of cancer in women in Turkey and in the World. The average incidence of this type of cancer in the world is 38-40 per hundred thousand and around 40 per hundred thousand in Turkey (Curado, 2011). Although breast cancer is a complex disease, it is one of the biggest reasons for death in women (Lal et al., 2017). Prostate cancer is the most common type of cancer in men in the world and it ranks second after lung cancers in Turkey. The world average is 28 per hundred thousand and this rate is 37 per hundred thousand in Turkey (Jemal et al., 2008; American Cancer Society, 2018). Effective diagnosis and treatment methods are needed to reduce the health and socioeconomic effects of these two types of cancer. Important studies explore ways

of employing chemotherapy and radiotherapy methods, which are frequently used in cancer treatment, while preventing damage to cells without distinction between cancerous and non-cancerous cells and destroying only cancerous cells, to reveal an alternative approach that does not have any toxic effects.

Gold colloids, which have been used safely in the treatment of rheumatoid joint diseases (Merchant, 1998; Root et al., 1954) for almost half-century and known to have no *in vivo* toxicity at long-term or other adverse effects (Connor et al., 2005; Shukla et al., 2005), have been used as theranostic systems in the diagnosis and treatment of cancer due to their unique biocompatibility and optical and electronic properties. By binding with ligands, these structures can recognize cell receptors on their surfaces and selectively target the cancer cells (Paciotti et al., 2004). In virtue of their plasmonic properties, they can locally destroy the cancer cells with photothermal effect under near-infrared (NIR) laser radiation, which is not harmful to tissues and has tissue penetration up to a depth of 10 mm. Thus, the local heating mechanism affects the minimum of the healthy cells and cells around the tumor and therefore is highly advantageous compared to conventional chemotherapy in terms of eliminating side effects (Oyelere et al., 2010). Another equally important advantage is that local heating mechanism can be effective in chemotherapy-resistant cancers by deactivating drug resistance mechanisms (Carpin et al., 2011). Positive results have been obtained from clinical trials of gold nanoparticles coated with PEG, polymer, biocompatible, along with prolongation of the circulation time in the blood flow (Libutti et al., 2010).

Gold nanoparticles in different forms promise innovative biomedical applications in drug delivery, biomedical imaging, and chemical diagnostics. Gold nanoparticles are also excellent agents for non-invasive imaging and diagnostic techniques such as “Surface-Enhanced Raman Spectroscopy” (SERS) and “NIR thermal imaging” (Qian et al., 2007; Charan et al., 2012). Gold nanoparticles can increase the Raman scattering efficiency of the adsorbed chromophores up to 10^{15} times, and thus, spectroscopic determination of a single molecule is possible under atmospheric conditions (Kneipp et al., 1999; Campion and Kambhampati, 1998). It has been reported in the literature that gold nanospheres which have been modified with Raman chromophores, PEG and cell-specific ligands make it possible to accurately diagnose tumors in mice using the SERS technique (Qian et al., 2007). Diagnostic efficacy with SERS can be enhanced by gold nanorods with larger surface area and stronger scattering (Vendrell et al., 2013). With a simpler approach, thermal imaging of tumors is also possible using targeted gold

nanorods and nanoshells. As a result of converting their absorbed light of these structures in the NIR region to heat via photothermal effect, distinctly increasing the temperature of these structures in the localized tumor area can be easily visualized with a thermal camera (Von Maltzahn et al., 2009). Plasmonic excitation of nanoparticles is more advantageous than imaging systems using organic dyes (Jain et al., 2006). Gold nanoparticles provide high resolution in confocal microscopy, dark field imaging, two-photon imaging, phase-sensitive optical coherence tomography and photoacoustic imaging in cell and tissue imaging due to this feature (Huang and El-Sayed, 2010; Yeh et al., 2012; Riley and Day, 2017).

AuNRs-based theranostics provide a platform to realize both diagnosis and therapy (Figure 2.13) (Zhang et al., 2013). Many types of research on the application of AuNRs in biology and health sciences have been mooted. Green et al. (2011) reported PEGylating antibody-AuNRs conjugates resulting in a 33.9 % improvement in the conjugation efficiency of AuNRs to tumor-targeted antibodies. Li et al. (2010) prepared the arginine-glycine-aspartic acid (RGD)-conjugated dendrimer-modified gold nanorods (RGD-dGNRs) for *in vivo* tumor targeting and selective photothermal therapy. They found that the RGD-dGNRs selectively killed tumor cells *in vitro* and *in vivo* and extend the life of mice loaded with tumors. In another study, Gormley et al. (2011) evaluated the cellular binding and uptake of gold nanorods surface-functionalized with the cyclic RGDfK peptide (RGDfK) in DU 145 human prostate cancer and HUVEC human umbilical vein endothelial cells. And also, the biodistribution of RGDfK surface-modified GNRs was then evaluated in prostate tumor-bearing mice. Targeting of the RGDfK surface-modified GNRs was confirmed *in vitro* due to selective binding by endothelial cells, but not observed *in vivo* due to the fast clearance of the RGDfK-GNRs from the blood.

One of the most important reasons why targeted therapies have not yet been fully developed in cancer is difficulties in selectively separating cancer cells from healthy cells. In addition to the routine pathological examination, discovering new molecules in the diagnosis of cancer and targeting cancer cells constitutes an important part of cancer research all over the world. The number of molecules used to precisely separate the cancer cell from the normal cell is quite limited. Although there are promising preclinical studies for this purpose, there is no molecule that fully meets the expectations. In the literature, receptors that are also prominently expressed in healthy tissues are often targeted such as

EGFR (El-Sayed et al., 2005) or folic acid (Jin et al., 2012) receptors. Treatments with such systems cannot truly eliminate the side effects.

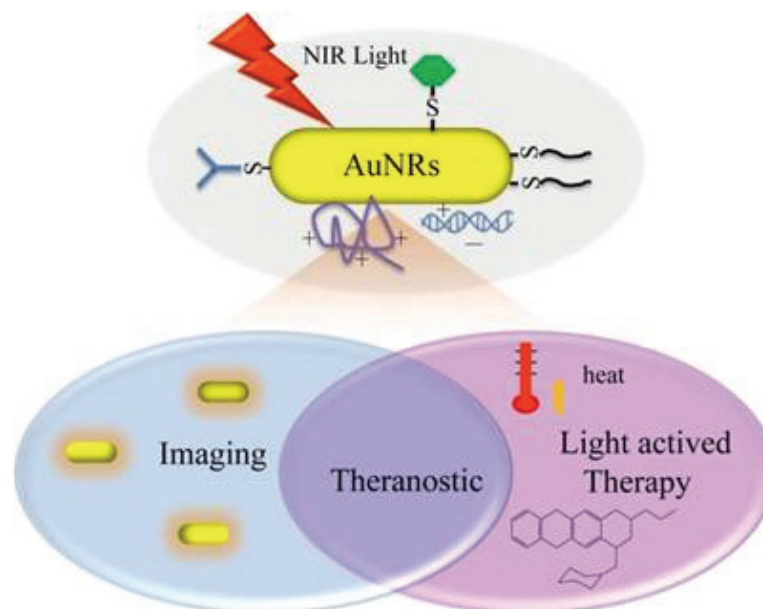


Figure 2.13. Illustration of light-mediated biomedical applications of modified AuNRs. (Source: Zhang et al., 2013)

More specific targeting of tumors can be achieved by conjugating tumor-specific recognition molecules to the surface of AuNPs (El-Sayed et al., 2005; Chithrani et al., 200; Eghtedari et al., 2009). In one study, citrate-capped AuNPs were conjugated with trastuzumab to target EGF receptors in human SK-BR-3 breast cancer cells (Jiang et al., 2008). In another study, gold nanoparticle was conjugated with Anti-HER2 monoclonal antibodies, which are known to target breast cancer cells overexpressing the HER2 epidermal growth factor cell surface receptor for use in a photodynamic therapy approach (Stuchinskaya et al., 2011).

Chanda et al. (2009) investigated whether synthetic bombesin peptide conjugated gold nanorods can preferentially locate gastrin-releasing peptide (GRP) receptors, which are overexpressed in prostate and breast tumor cells as theranostic agents. They designed and developed the target-specific gold nanorods by conjugating with GRP-receptor avid bombesin peptide for the treatment of cancers. In another study, researchers demonstrated the potential of gold nanorod-PEG-bombesin as a photoacoustic imaging agent that can

provide improved specificity and sensitivity for breast cancer detection (Heidari et al., 2014).

Centi et al. (2014) presented the preparation and the application of AuNRs conjugated with anti-CA125 (Cancer Antigen 125) antibodies to detect cells overexpressing CA125, which is very specific for ovarian cancers.

Moreover, the surface of lipid nanoparticles can be engineered for active targeting. Also, lipid nanoparticles have recently been used in the diagnostic field for contrast magnetic resonance imaging (MRI), and dyes have been conjugated to lipid nanoparticles for therapeutic agents and diagnostic tools in the same multimodal theranostic nanoparticle. Lipid nano- and microparticles are widely useful in peptide and protein delivery due to the stabilizing and absorption promoting effect of lipids (Battaglia and Ugazio, 2019).

2.7. Photothermal Therapy

Gold nanorods show superior plasmonic properties compared to nanosphere geometry. The nanorods give heat to their surroundings by radiation between 700-900 nm which does not damage the tissues (Pissuwan et al., 2008). It was determined that the applied gold nanorods in mice increased the temperature in the center of the tumor by 20 °C with minimal damage to the surrounding tissue under laser irradiation for only 10 minutes (Dickerson et al., 2008). In a published study, researchers investigated the potential of the gold nanorods as a targeted diagnostic and therapeutic agent for breast cancer by modifying with trastuzumab and porphyrin of the surface of the gold nanorods (Kang et al., 2017). In another similar study, gold nanorods modified with chitosan and Pluronic F-68 were injected into mice with squamous tumors, and photothermal therapy was applied. In the study, it was found that gold nanorods have an efficient therapeutic effect in cancer treatment *in vivo* (Choi et al., 2011). In the literature, it has been reported that nanorod structures in a shell (rod-in-shell) which newly emerged showed a more effective photothermal effect in the 2nd NIR window (1000-1350 nm) which provides much deeper tissue penetration (Tsai et al., 2013). Materials which are effective in the 2nd NIR range considering in the 1st NIR window are quite limited in the literature. Fluorophores with toxicity problems in quantum nanoparticles such as PbS, PbSe, Ag₂S

are available. Materials less than 100 nm in size that absorb light in the 2nd NIR region are much more limited (Huang et al., 2010, 2011). Recently, the nanoshell structure containing a single Au nanorod in the Ag / Au shell has been synthesized, and it has been determined to be highly effective in the photothermal destruction of tumors in both the 1st and 2nd NIR regions (Tsai et al., 2013). The cell membrane deformation of lipid conjugated gold nanorods is less than CTAB-coated gold nanorods, so the uptake of lipid conjugated ones into the cell is more efficient (Yoo et al., 2013).

Photothermal therapy (PTT) kills abnormal cells by causing external light-induced hyperthermia on malignant tissues (Figure 2.14). Unfortunately, traditional hyperthermia techniques are not suitable because of their invasive effect and result in the non-specific generation of heat throughout the body and undesirable side effects (Kaur et al. 2016). Also, the traditional photodynamic therapy (PDT) technique using a laser or visible light is limited by the insufficient depth of penetration in tissues (Ochsner, 1997; Wilson and Patterson, 2008). However, NIR light (in the wavelength range of 800–1200 nm) has much greater body transparency and penetrates deep into biological tissues for PTT. It has been demonstrated that a threshold temperature ranging between 70 and 80 °C is required to completely destroy cancer cells *in vitro* (Huang et al., 2006). Regarding this, a more promising cancer treatment technique would involve a targeted, nanoparticle-mediated localized hyperthermia. This technique has recently attracted attention with its ease, minimal intervention, reliability, and remote-control features.

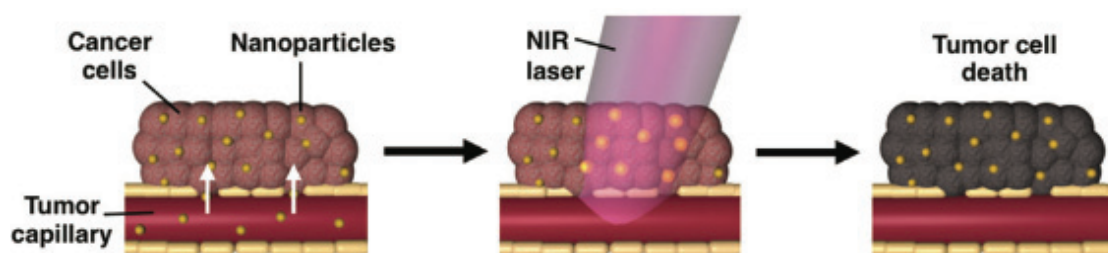


Figure 2.14. Schematic illustration of the biological effects of gold nanoparticle-mediated photothermal therapy (PTT).

(Source: Riley and Day, 2017)

Various PTT agents such as ferromagnetic nanoparticles, gold nanoparticles, copper sulfide nanoparticles, carbon nanotubes, and polymer-based technologies have

been developed (Lee et al., 2011; Fantechi et al., 2014; Huang et al., 2010; Kaur et al., 2016). PTT agents can precisely target tumor cells by modifying target groups such as ligands, peptides, and proteins.

AuNPs stand out as a new generation agent in photothermal treatment due to their biocompatibility and photostability. When the gold nanomaterials in different structures were examined, it was found that small spherical gold nanoparticles were not suitable for PTT because they could not absorb the near-infrared beams sufficiently. However, AuNRs are suitable materials for PTT owing to their strong light absorption, good photostability, and high photothermal conversion efficiency. Since AuNRs showed strong light absorption and scattering in the NIR region, their therapeutic potentials due to surface plasmon oscillation were investigated (Jana et al., 2001). The longitudinal band has a larger extinction coefficient than the transverse band and thus, AuNRs are extraordinary materials with an intense surface plasmon band (Niidome et al., 2006). Strong light absorption in the NIR region allows more heat radiation of AuNRs. This radiated heat has been used efficiently in drug release and targeted drug delivery systems without damaging the surrounding tissues (Kim et al., 2009). Xu et al. (2018) developed PEGylated gold nanorods based nanoplatform for triple-combined chemotherapy, photodynamic therapy and photothermal therapy of breast cancer. Upon irradiating with laser, the temperatures of gold nanorods suspensions increased approximately 55 °C after 10 minutes. To the best of the author's knowledge, temperature changes in photothermal therapy have been generally observed using a high power NIR laser in many studies in the literature. In addition, the effects of AuNRs with different aspect ratios on toxicity have not been compared, and there is no detailed study in the literature comparing the photothermal effects of different aspect ratio AuNRs.

Photothermal therapy relies on the conversion of light energy into heat energy caused by cellular necrosis or apoptosis (Ray et al., 2012). AuNRs are converted into light heat energy. Heat is an effective approach for the destruction of tumor cells and for the supply and penetration of molecules into the cell. When a metallic particle is irradiated by external light at the appropriate wavelengths, the free electrons on the particle surface are excited, and conduction-band electrons collectively oscillate at the same frequency, which is termed as localized surface plasmon resonance (LSPR) (Kim et al., 2019). When a photon of light strikes a metallic particle, it may be absorbed, transmitted or scattered. The total energy of the incoming light must equal the sum of the energies of the transmitted, absorbed or scattered light due to the law of conservation of energy. Gold

particles strongly absorb the light, and their excited plasmons follow two different decay processes in the LSPR condition. Some of the absorbed light decays radiatively by emitting photons with the same frequency as the incident light (scattering), while some decays nonradiatively by converting into phonons (absorption). Thus, the absorbed light is converted to heat (Cortie et al., 2018).

AuNRs were first studied for use in NIR spectrum photothermal therapy by Jain et al. (2006). Recent advances in photothermal treatment methods have been largely attributed to the emergence of AuNRs. Targeted photothermal therapy with gold nanoparticle structures has been tried in various tumors in a limited number of studies worldwide, and successful results have been obtained (Hirsch et al., 2003; Yuan et al., 2012; Eghtedari et al., 2008). In addition to stabilizing and preventing the toxic effect of AuNRs, selective targeting and drug release are essential for functionalization. The remarkable resonance properties of gold nanoparticles earn them an important place among alternative innovative methods in photothermal treatment. This resonance feature consists of obtaining energy output by sending the beams to the surface of gold nanoparticles at specific wavelengths. Gold nanoparticles that absorb light stronger than organic dyes convert almost 100 % of absorbed light into heat by non-radioactive means.

PTT is an effective treatment strategy in tumor tissue ablation without damaging the surrounding healthy cells in preclinical trials (Chen et al., 2016). Tumor cells are more sensitive to hyperthermic effects than normal cells because of their high metabolic activity compared to other cells. For this reason, abnormal cells are killed easily by localized hyperthermia (Kapp et al., 2000; Wust et al., 2002). In treatment applications, AuNRs were also used for the thermal ablation of tumor cells in animals (Choi et al., 2011). Bovine serum albumin (BSA)-coated gold nanorods (BSA-coated AuNRs) were used for photothermal ablation of breast tumor cells, and incubation with BSA-coated AuNRs at an Au concentration of 0.4 mM killed all the tumor cells by laser irradiation (Wang et al., 2019). Although there are some studies on breast cancer cells using AuNRs, studies on prostate cancer are almost unavailable.

PTT agents, when equipped with amphiphilic components such as liposomes, polymers, and micelles, may also accumulate in malignant tissues by the effect of enhanced permeability and retention (EPR) resulting from long circulation time or high concentration (Hou et al., 2015). Additionally, studies on lipid-conjugated gold nanoparticles generally focus on the modification of gold nanoparticles with the lipid

layer. In particular, there are a limited number of studies in the literature on gold nanostructures interacting with liposome structures.

Troutman et al. (2008) developed gold on the surface of dipalmitoyl phosphatidylcholine (DPPC) for photothermal mediated drug release in the near-infrared (NIR) region. Rengan et al. (2014) reported that Lipos Au NPs can be used for photothermal therapy of breast cancer cells. They can also be applied for drug delivery applications using NIR laser irradiation (Figure 2.15).

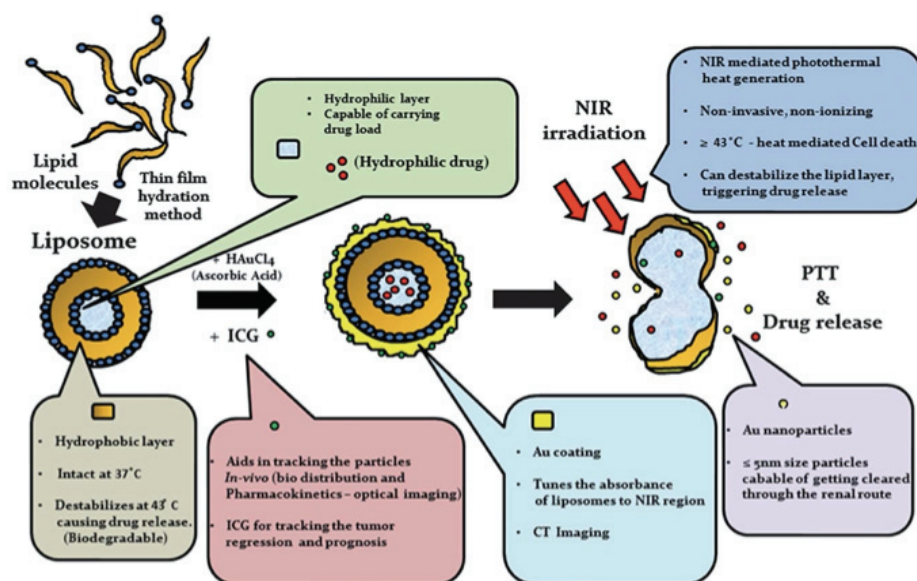


Figure 2.15. Multifunctional gold coated liposome nanoparticle (Lipos Au NP) in imaging, drug delivery and photothermal therapy PTT. (Source: Rengan et al., 2014)

Biodegradable liposome gold nanoparticles (LiposAu NPs) were used for killing cancer cells by photothermal therapy. Further, the therapeutic potential of LiposAu NPs was tested in the mouse tumor model using NIR laser (750 nm) and resulted in a complete ablation of the tumor mass (Rengan et al., 2015) (Figure 2.16).

Liu et al. (2016) exhibited the photothermal, pH-responsive drug release and superior antitumor property of gold nanoshells-coated Oleanolic acid (OA) liposomes. This gold nanoshells-coated OA liposomes structure has a great potential for chemophotothermal antitumor therapy. Chauhan et al. (2018) investigated gold nanorods-liposome nanohybrid for photothermal therapy and chemotherapy. The therapeutic

efficacy of combined targeted chemo-photothermal therapy of gold nanorods-liposome nano hybrid is significantly higher than the additive therapeutic efficacy of chemotherapy and photothermal therapy.

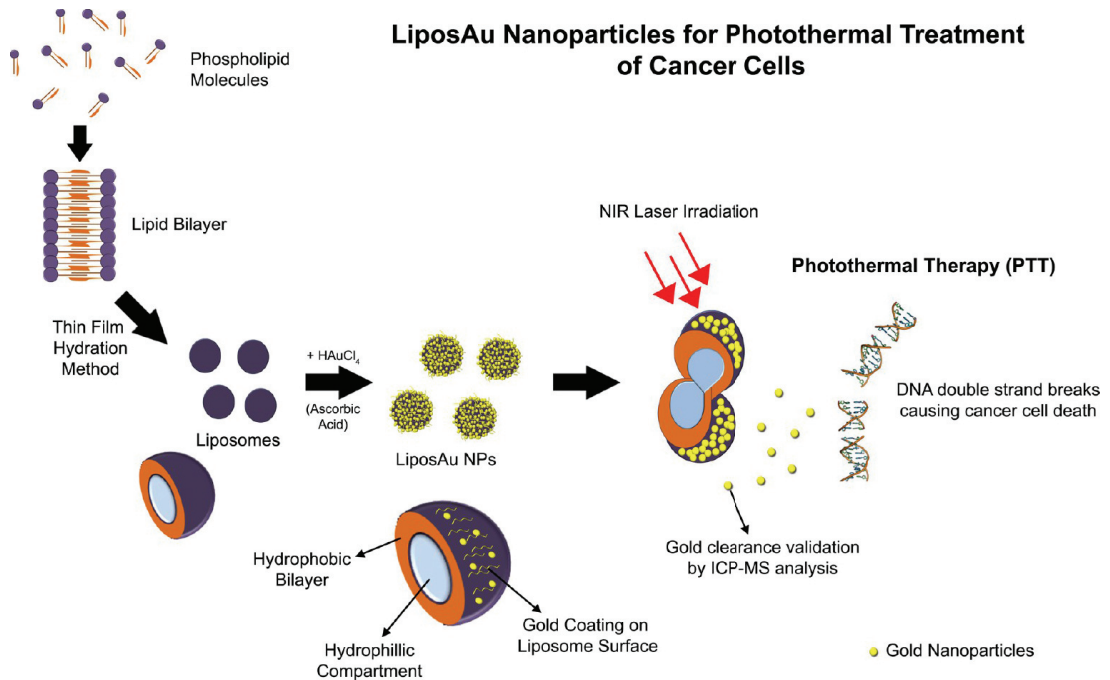


Figure 2.16. Illustration of synthesis of LiposAu NPs and their photothermal treatment with intracellular DNA damage.
(Source: Rengan et al., 2015)

CHAPTER 3

MATERIALS AND METHODS

3.1. Materials

3.1.1. Chemicals

Cethyltrimethylammonium bromide (CTAB) – Sigma, L-Ascorbic acid (AA) – Fluka, Tetrachloroauric acid (HAuCl_4) and Silver nitrate (AgNO_3) – Alfa Aesar, Sodium Borohydride (NaBH_4) – Sigma, Sodium oleate (NaOL) – acbr, Didodecyldimethylammonium bromide (DDAB) – Alfa Aesar, 1,2-dipalmitoyl-*sn*-glycero-3-phosphocholine (DPPC) – Avanti POLAR Lipids, 1,2-distearoyl-*sn*-glycero-3-phosphoethanolamine (DSPE) – NOF AMERICA CORPORATION, 1,2-distearoyl-*sn*-glycero-3-phosphoethanolamine-N-[methoxy(polyethylene glycol)-2000] (DSPE-PEG) – Biochempeg Scientific Inc., 1-palmitoyl-2-oleoyl-glycero-3-phosphocholine (POPC) – Avanti POLAR Lipids, Chloroform – Sigma, Ethanol ($\text{C}_2\text{H}_5\text{OH}$, 99 %) – Sigma, Nitric acid (HNO_3 , 65 %) – Merck, Ammonium hydroxide (NH_4OH , 32 %) – Merck, Sulfuric acid (H_2SO_4 , 95-97 %) – Merck, Hydrogen peroxide (H_2O_2 , 30 %) – Merck, Hydrochloric acid (HCl , 37 %) – Merck, Dimethyl sulfoxide (DMSO, 99 %) – Sigma, Potassium carbonate (K_2CO_3 , >99 %) – Sigma Aldrich, Sodium bicarbonate (NaHCO_3) – Sigma Aldrich, N-ethyl-N'-(3-dimethylaminopropyl) carbodiimide hydrochloride (EDC) – Merck, N-Hydroxysulfosuccinimide (Sulfo-NHS) – Thermo Scientific, Methoxy-Polyethylene glycol (mPEG-SH, MW: 5000 Da) – Laysan Bio, Thiol- and amine-bifunctional PEG (SH-PEG-NH₂, MW: 1000-5000 Da) – Biochempeg Scientific Inc., Dialysis membrane (MWCO=3.5, 20 and 50 kDa) – Spectrum® Labs, Silicon (p-type; 100, Silicon Inc.), RPMI 1640 (+L-Glutamine) – Gibco, Fetal bovine serum (FBS) – Gibco, Penicillin-streptomycin (Pen-strep) – Gibco, Epidermal growth factor human recombinant (EGF) – Biovision, Bovine pituitary extract (BPE) – Thermo Scientific, Hydrocortisone – Calbiochem, Insulin – Sigma, Phosphate Buffer Saline (PBS) – Gibco,

Keratinocyte SFM – Gibco, Trypan Blue stain – Biological Industries, Thiazol Blue Tetrazolium Bromide (MTT) – Sigma, Alexa Flour 647 NHS ester – Thermo Fisher Scientific. All chemicals were used as received. A non-commercial rabbit monoclonal antibody against sialic acid derivative cell receptors and cell lines (human breast cancer MCF7, prostate cancer DU 145, breast epithelial MCF 10A, prostate epithelial RWPE-1) were kindly provided by Prof. Dr. Gülperi Öktem at Ege University. DI water ($18.2 \text{ M}\Omega\text{cm}^{-1}$) treated through reverse osmosis (Thermo Scientific) was used for preparing all solutions.

3.1.2. Instruments

3.1.2.1. UV-Visible / Near IR Spectrophotometer

UV-Vis / NIR extinction measurements were carried out using Ocean Optics USB2000+VIS / NIR spectrophotometer fiber optically coupled to a light microscope with unpolarized white light provided by a tungsten halogen lamp. In this study, all spectra are macroscopic measurements performed in standard transmission geometry mode.

3.1.2.2. Electrophoretic Light Scattering (ELS)

The surface charge of gold nanostructures was evaluated using a MALVERN Zetasizer Nano ZS. Zeta potential measurements were performed after an equilibration time of 120 s and 2 x 70 runs at 25 °C. Each measurement was repeated at least three times.

3.1.2.3. Scanning Electron Microscopy (SEM)

SEM images were obtained using a Philips XL 30S FEG, FEI QUANTA 250 FEG and Zeiss Ultra Plus High-Resolution FE-SEM equipped with an in-lens secondary-electron detector at operating range 5-20 keV depending on sample charging. Images were acquired with back-scattered electron (BSE) and second electron (SE) detectors. A total of 20 μL of the sample solution was dropped on Si (111) previously cleaned using Piranha (CAUTION) solution and allowed to dry in the open atmosphere for SEM analysis. Freshly prepared samples were attached to the sample holder with conductive carbon adhesive tape. All SEM measurements were performed at the Materials Research Center of İzmir Institute of Technology.

3.1.2.4. Atomic Force Microscopy (AFM)

A Nanosurf FlexAFM operating in tapping mode at room temperature in air was used to obtain topographic data. All imaging operations were conducted with 512 x 512 data acquisitions at various scan speeds. Oxide-sharpened silicon nitride tips with integrated cantilever with a nominal spring constant of 42 N/m were used. These tips have resonance frequencies between 204 and 497 kHz and an effective radius of curvature at the tip of less than 7 nm. AFM images were processed by using Scanning Probe Image Processor (SPIP) software. 20 μL of the sample solution was dropped on the Si substrate and allowed to dry in the open atmosphere for AFM analysis.

3.1.2.5. X-Ray Photoelectron Spectroscopy (XPS)

Elemental analyses of the samples were performed via Thermo Scientific K-Alpha Surface Analysis XPS system. The measurements were taken from an area of 300 μm diameter with x-rays produced by Al-K α beam source. Freshly prepared samples on Si surface were attached to the sample holder. The base pressure of the vacuum chamber

was 1.0×10^{-8} mbar during the measurements. The spectra were recorded with a pass energy of 50 eV, which corresponds to a spectral resolution of ca. 0.5 eV. The spectra were referenced to the C 1s binding energy at 284.8 eV.

3.1.2.6. Inductively Coupled Plasma Mass Spectroscopy (ICP-MS)

Inductively coupled plasma-mass spectroscopy connected Agilent 7500ce Octopole Reaction System (ORS) was used to determine the gold concentration in the gold nanostructure solutions. Briefly, amounts of gold in gold nanostructure solutions (3 ml) were measured by ICP-MS by digesting in a microwave oven for 25 min ramp to 180 °C at 1200 W with 25 min of hold in aqueous mixture of 3 ml HCl (37 %), 1 mL HNO₃ (65 %) and 1 mL H₂O₂ (30 %). Samples extracted from digestion were diluted with water to 20 ml and ICP-MS measurements were performed. Each experiment was conducted with at least three independent replicates. In addition, ICP-MS was used to quantify the gold nanostructures in cell uptake experiments.

3.2. Methods

3.2.1. Synthesis of Gold Nanorods (AuNRs)

In this thesis, gold nanorods (AuNRs) were synthesized via seed-mediated method. In order to vary the aspect ratio (AR) of AuNRs, the seed-mediated synthesis method was adapted from Green et al. (2011) for ARs between 2 and 4 and Ye et al. (2013) for AR of 7.

First, an aqueous sodium borohydride (0.01 M, 0.6 ml) was added to an aqueous solution containing CTAB (0.2 M, 5 ml) and HAuCl₄ (0.001 M, 2.5 ml) for synthesis of seed solution. Yellow-brownish seed solution was stirred for 2 h in order to remove excess Na ions.

Then, CTAB (0.2 M, 17-20 ml) was mixed with HAuCl₄ (0.001 M, 17-20 ml), AgNO₃ (0.032 M, 60-100 μl) and ascorbic acid (0.079 M, 260-280 μl). Then, 60-100 μl

of seed solution was added to this mixture. The growth solution was stored overnight at room temperature for nanorod formation (Green et al., 2011).

In order to produce AuNRs with higher AR (AR=7), a binary surfactant mixture methodology was adapted from Ye et al. (2013). Briefly, for the preparation of growth solution, CTAB (3.5 g) and NaOL (0.617 g) were dissolved in water (125 ml) at 50 °C. After mixing, the temperature of the solution was reduced to 30 °C. Then AgNO₃ (9-15 ml) and HAuCl₄ (125 ml) were added and final solution was let to stand for 15 minutes. The resultant solution was stirred for 1.5 hours at high speed, until resultant solution was turned into colorless. After producing a colorless solution, the speed was reduced and HCl (1-2 mL) was added into the solution and stirred for further 15 minutes. Lastly, AA (625 µl) was mixed with the final solution.

To synthesize seed solution, an aqueous sodium borohydride (0.01 M, 0.6 ml) was added to a 10 ml aqueous solution containing CTAB (0.2 M, 5 ml) and HAuCl₄ (0.5 mM, 5 ml). The mixture was then stirred at room temperature for 2 minutes at high speed and left to stand for 30 minutes. Finally, 200-400 µl of seed solution was mixed with the prepared growth solution. The final solution was allowed to incubate overnight in a water bath at 30 °C.

The undesired structures and excess surfactants were removed from the resultant solution via centrifugation which was performed twice between 8 000 and 13 500 rpm for 15-30 minutes depending on the dimensions of nanostructures. The centrifugation procedure was repeated until most of the surfactant was removed from the solution. At the end, produced precipitates were re-dispersed in DI water.

The synthesized AuNRs used in experiments are summarized in Table 3.1.

Table 3.1. Synthesized AuNRs used in experiments.

Sample code	Sample description
AuNRs (AR=2.7)	Gold nanorods with aspect ratio of 2.7
AuNRs (AR=3.2)	Gold nanorods with aspect ratio of 3.2
AuNRs (AR=4.0)	Gold nanorods with aspect ratio of 4.0
AuNRs (AR=7.0)	Gold nanorods with aspect ratio of 7.0

3.2.2. Surface Modification of AuNRs

3.2.2.1. Modification of AuNRs with Poly(ethylene glycol) (PEG)

AuNRs were modified with a mixture of mono- and bi-functional PEG molecules (i.e. monomethoxy-PEG thiol (mPEG-SH, MW: 5000 Da) and amine-PEG-thiol (SH-PEG-NH₂, MW: 5000 Da), respectively) at a mol ratio of 4:1. For modification, AuNR suspensions were incubated for overnight in a mixture inhabiting K₂CO₃ (2 mM) and mixed PEG (5 mM) (Liopo et al., 2012). PEGylated AuNRs were centrifuged at 12 500 rpm for 15 min to remove excess PEG molecules.

3.2.2.2. Antibody Conjugation of AuNRs

A home-made antibody against a derivative of a sialic acid receptor that is thought to be highly expressed on prostate and breast cancer cells was covalently conjugated to PEGylated AuNRs (mPEG-SH: NH₂-PEG-SH (a mol ratio of 4:1) via EDC/Sulfo-NHS chemistry.

Briefly, the carboxylic groups on antibody was first activated by mixing 50 µl of antibody (3 mg/ml) with EDC solution (40 mM) and then Sulfo-NHS solution (5 mM) in PB buffer at pH 7.4 and allowing for 15 minutes. Afterwards, resultant reaction mixture was added to the PEGylated AuNRs solution and final mixture was left for incubation at +4 °C overnight. At the end of incubation time, the solution was centrifuged at 12 500 rpm for 15 minutes and washed with ultrapure water at least twice in order to eliminate unreacted reagents and remaining side-products (Cho et al., 2014).

3.2.2.3. Labelling of AuNRs

For *in vitro* cell uptake experiments, AuNRs were labelled with Alexa Flour 647 fluorescent dye. To prepare fluorescent-labelled AuNRs, NH₂-PEG-SH was first labeled

with Alexa Flour 647-NHS ester fluorescent dye. Briefly, fluorescent dye was added to the polymer solution (dye and polymer at a mol ratio of 2:1) in water under stirring for 24 h at room temperature. The dye-polymer mixture was purified against water via dialysis using a membrane having a MWCO 3500 Da for 3-5 days. After dialysis, the dye-polymer mixture was freeze-dried. In order to prepare fluorescent-labelled AuNRs, CTAB-stabilized AuNRs were mixed with mono- and bi-functional PEG mixture having fluorescent-dye conjugated using the procedure described in Section 3.2.2.1 followed by purification step.

In order to prepare fluorescent-labelled antibody conjugated AuNRs, PEGylated AuNRs were conjugated with fluorescent dye-labelled antibody via NHS/EDC chemistry as described in Section 3.2.2.2. Fluorescent dye-labelled antibody was prepared according to the procedure described by Hermanson (2008). Briefly, Alexa Flour 647 NHS ester fluorescent dye was first dissolved in 100 μ l DMSO to yield a final concentration of 10 mg/ml. Then 50 μ l of antibody (3 mg/ml) diluted to 1000 μ l in NaHCO_3 . The antibody and the dye were stirred for 4 h. After 4 h, the final mixture was dialyzed for 3-4 days using a membrane of MWCO 50 kDa. The antibody-dye conjugate was obtained after freeze-drying. Finally, labelled antibody was mixed with PEGylated AuNRs for EDC/Sulfo-NHS reaction.

3.2.3. Lipid-stabilized AuNRs Synthesis

Different lipids and lipid mixtures were used instead of the CTAB stabilizer to produce AuNRs. The lipid types and the concentrations tested for the synthesis of lipid-stabilized AuNRs are given in Table 3.2.

Initially, lipid films were prepared (Orendorff et al., 2009; Avanti Polar Lipids, Inc.). To do that, lipids were first dissolved in chloroform and the organic phase was evaporated using rotary evaporator. In order to ensure the removal of organic phase, reaction flask was dried under high vacuum conditions overnight. The lipid films were then dissolved by addition of equivalent volume of pure water and allowed to stand at 40 $^{\circ}$ C for 1 hour. After thawing, three cycles of sonication process were repeated for 30 minutes. In the next step, the lipid solution was centrifuged at 13 500 rpm for 20 minutes. The supernatant portion was filtered through a 0.22 μ m filter.

Table 3.2. Lipids and concentrations used in the preparation of lipid-stabilized AuNRs.

Lipid (Mol Ratio)	Total Lipid Concentration
DDAB	5 mM, 10 mM, 15 mM, 20 mM, 40 mM
POPC	10 mM, 15 mM
DSPE-PEG	0.1 μ M, 0.25 μ M, 0.5 μ M, 1 μ M, 2 μ M, 5 μ M, 10 μ M, 20 μ M, 30 μ M, 50 μ M, 100 μ M, 1 mM
DPPC	1 mM, 5 mM, 10 mM, 15 mM
DSPC	1 mM, 10 mM
DDAB: DSPE-PEG (3:1)	15 mM
DDAB: DSPE-PEG (0.9:1)	15 mM
DDAB: DSPE-PEG (14:1)	13 mM
DDAB: DSPE-PEG (2.5:1)	8 mM
DDAB: DSPE-PEG (5.8:1)	11 mM
DDAB: DSPE-PEG (1:4)	1 mM
DDAB: POPC (2.7:1)	14 mM
DDAB: POPC (0.9:1)	13 mM
DDAB: POPC (0.3:1)	11 mM
DDAB: POPC (27.3:1)	12 mM
DDAB: POPC (9.1:1)	8 mM
DDAB: POPC: DSPE-PEG (20:1:2.8)	6.9 mM
DDAB: POPC: DSPE-PEG (30:1:2.8)	10.1 mM
DDAB: POPC: DSPE-PEG (40:1:2.8)	13.3 mM
DDAB: DPPC (2.8:1)	13.8 mM
DDAB: DPPC (17.5:1)	10 mM
DDAB: DPPC (23.3:1)	13.3 mM
DDAB: DPPC: DSPE-PEG (20:1:2.8)	6.9 mM
DDAB: DPPC: DSPE-PEG (30:1:2.8)	10 mM
DDAB: DPPC: DSPE-PEG (40:1:2.8)	13.3 mM
DDAB: DPPC: DSPE-PEG (28:1:2.8)	9.4 mM
DDAB: DPPC: DSPE-PEG (17.3:1:2)	8.7 mM

(cont. on next page)

Table 3.2. (Cont.)

DDAB: DSPE (23:1)	13.3 mM
DDAB: DSPE: DSPE-PEG (40:1:2.8)	13.3 mM
DPPC: DSPE (1.5:1)	1 mM
DPPC: DSPE-PEG (1:2.5)	1 mM
DSPE: DSPE-PEG (1:2.5)	1 mM

AuNRs were produced by the colloidal seed-mediated method which is a two-step process involving the synthesis of the seed solution followed by the synthesis of the growth solution (Smith and Korgel, 2008). For this purpose, each lipid film or lipid mixtures (Table 3.2) were prepared as described above. Concentrations of all reagents in the synthesis were calculated according to the initial concentration of lipid. The mol ratios of reagents were constant in solutions. The mol ratio of lipid: H₂AuCl₄: NaBH₄ in the seed solution was 10:1:1. All reagents in the growth solution were used with a mol ratio of 10:1:1:10 for lipid: H₂AuCl₄: AgNO₃: AA. Then, cold NaBH₄ (0.2 ml) was added to the mixture containing lipid solution (3.25 ml) and H₂AuCl₄ (83 μl) to synthesize the seed solution and the mixture was stirred for 2 minutes. After the seed solution was prepared, AgNO₃ (150 μl), H₂AuCl₄ (0.5 ml) and AA (55 μl) were added to the lipid solution (9.5 ml) for the synthesis of the growth solution. Finally, the gold seed solution (20 μl) was added to the mixture and allowed to grow overnight. The undesired structures and excess surfactants were separated from the resultant solution via centrifugation which was performed twice at 13 500 rpm for 30 minutes. At the end, produced precipitates were re-dispersed in DI water.

3.2.4. The Synthesis of AuNBs

A new method was developed to synthesize lipid nanobubbles containing AuNRs using a mixture of DPPC and DSPE-PEG lipids. The experimental procedure for the preparation of AuNBs was illustrated in Figure 3.1.

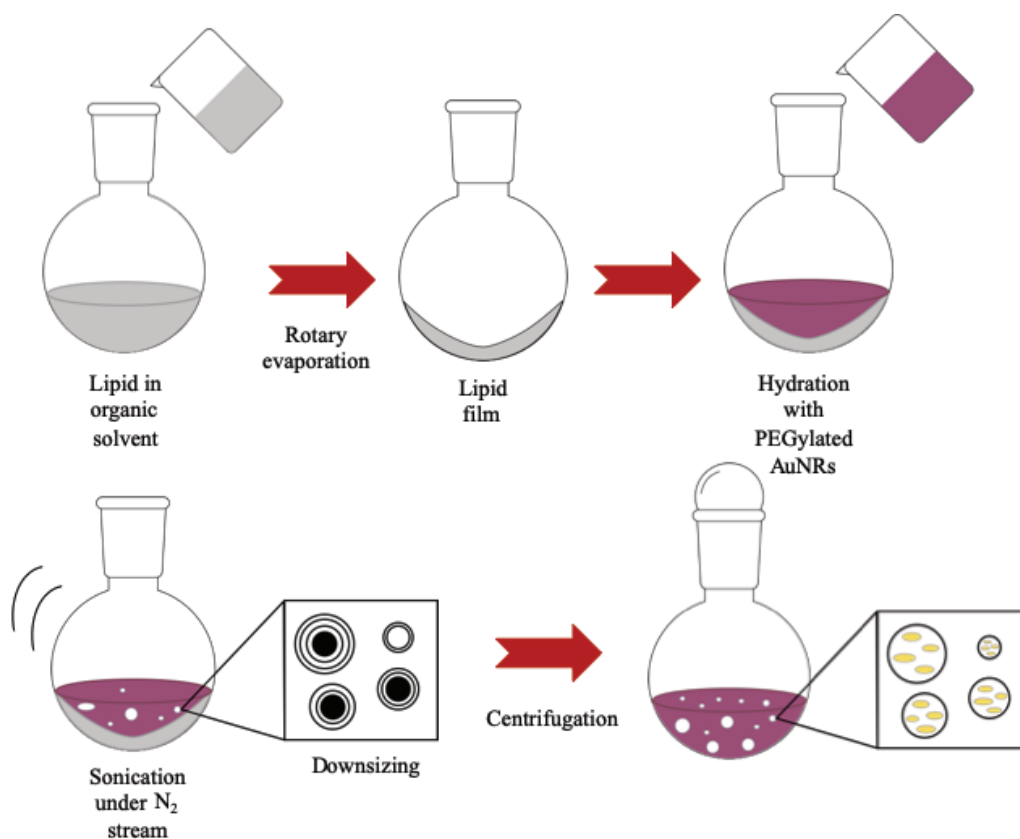


Figure 3.1. Schematic representation of AuNBs synthesis procedure.

The surface of the synthesized AuNRs was first modified with NH₂-PEG-SH (Mn of 1000 g/mol). A lipid film was formed using a mixture of 1 mM DPPC and 1 mM DSPE-PEG (50 % v/v) according to beforementioned procedure. Then, PEGylated AuNRs were suspended by adding to lipid film. Subsequently, the suspension was allowed to stand at 50 °C for 1 h. In order to reduce the size of the liposome vesicles, three cycles of sonication were performed under nitrogen gas for 30 minutes. The final product was centrifuged at 12 500 rpm for 20 mins and remaining precipitates were suspended in distilled water.

To label the AuNBs with fluorescence dye, AuNRs modified with fluorescence-conjugated PEGs were used in preparation of AuNBs.

3.2.5. Determination of Photothermal Effect in Nanostructure Solutions

Nanostructure solutions at different concentrations were irradiated by a 780 nm and 808 nm diode laser with varying power densities (100 mW, 200 mW and 500mW). The temperature of the solution in tube was monitored using a thermocouple. The tube was isolated from the environment using a light/heat proof chamber. Each measurement was repeated three times. The experimental setup for determination of photothermal effect of nanostructures was depicted in Figure 3.2.



Figure 3.2. Experimental setup for photothermal effect measurements of nanostructures.

3.2.6. *In vitro* experiments

3.2.6.1. Cell culture

Human prostate cancer (DU 145) and breast cancer (MCF7) cells were cultivated in RPMI 1640 containing 10 % fetal bovine serum (FBS) and 1 % penicillin-streptomycin (pen-strep) at 37 °C under 5 % CO₂ atmosphere. Human prostate epithelial (RWPE-1) cells were cultivated in Keratinocyte containing Bovine Pituitary Extract (BPE), human recombinant Epidermal Growth Factor (EGF) and 1 % pen-strep; human breast epithelial (MCF 10A) cells were cultivated in RPMI 1640 containing 10 % FBS, EGF, hydrocortisone, insuline and 1 % pen-strep at 37 °C under 5 % CO₂ atmosphere.

After reaching 70-80 % confluency, cells were passaged. Firstly, culture medium was poured. Cells were washed with Trypsin-EDTA and 2 - 3 ml of Trypsin-EDTA was added to the flask, then placed at 37 °C in order to detach of cells easily. After trypsination, cells were spinned at 800 rpm for 5 mins. The culture medium was gently poured, and cells were resuspended in fresh cell culture medium.

3.2.6.2. Cytotoxicity assays via MTT

Before cytotoxicity assays, standart curves for cell numbers were determined using MTT technique. For cell number determination, four cell lines were seeded in 96-well plates at varying concentrations between 10⁴ and 10⁶ cell/well and varying volumes between 100 and 200 µl. After 24 hours incubation, 10 µl of MTT dye (5 mg/ml) was added and allowed to incubate for 3 hours. After the incubation period, plate was centrifuged at 1800 rpm for 10 minutes. The solution in each well was poured gently. Precipitates were dissolved with DMSO (100 µl/well) in order to dissolve formazan crystals. Then, plate was shaken at 150 rpm for 5 mins and absorbance of each well was measured using a Varioscan plate reader at 570 nm.

Cells were exposed to different concentrations of AuNRs and AuNBs suspensions (0.1-1.2 mM Au). Cells were counted on hemocytometer. The cell suspensions were transferred into 96-well plates. Before addition of gold nanostructures to cells,

nanostructures were dispersed in PBS (pH 7.4). Gold nanostructure dispersions were added into the cells to yield 5 % (v/v) PBS in cell culture media. Cells containing only 5 % (v/v) PBS was used as control group. Cells with gold nanostructure dispersions were incubated at 37 °C for 24 h. After 24 h incubation, MTT dye in PBS solution was added to each well (10 µl/well) and the plate was further incubated for 3 h at 37 °C. Then, MTT procedure was continued according to cell number determination. The absorbance values were acquired using a Varioscan plate reader at 570 nm. All experiments were repeated five times.

3.2.6.3. Photothermal Therapy

Human prostate cancer (DU 145) and breast cancer (MCF7) cells were cultured in 96-well plates. Next, cells were incubated with PEGylated AuNRs (AR=4.0 and AR=7.0) and AuNBs at 0.2, 0.5 and 1.0 mM Au concentration for 24 h. Cells with no treatment, cells with gold nanostructures and cells after laser exposure in the absence of gold nanostructures were used as control groups. After 24 h, 808 nm diode laser with the power density of 500 mW was exposed to both cell types. After 15 mins exposure the laser, cells were incubated for further 2 h at 37 °C and dyed with MTT. The standart MTT assay protocol was then performed on all samples (Li et al., 2018).

3.2.6.4. Cell Uptake

Cell uptake experiments were performed using two different methods. In the first method, cells were collected after 80 % confluency and centrifuged at 800 rpm for 5 minutes. The culture medium including Trypsin-EDTA was discharged and pellets were suspended in fresh medium. Cells were then incubated in 6-well plates at a concentration of 10^6 cells/ well for overnight. Cells were incubated with PEGylated AuNRs (0.1 mM concentration) for 1 h. Cells containing only 5 % (v/v) PBS were cultivated as a control group. Each experiment was performed as triplicate. After incubation, cells were washed with PBS, three times. Lysis buffer was added in each well and wait for 15 mins. Cells

were collected and stored at +4 °C for further analysis using ICP-MS. In order to determine the cell uptake, the cells were digested in a microwave oven at 180 °C within a mixture of aqueous HCl, HNO₃ and H₂O₂. Samples extracted from digestion were diluted to 20 ml and ICP-MS measurements were performed. Each experiment was conducted with at least three independent replicates.

Secondly, time-dependent cell uptake experiments were determined via flow cytometry (BD FACSCanto™, BD Biosciences, San Jose, U.S.A.), equipped with solid-state 633 laser and 660/20 filter configuration. Data from 10000 events per sample were collected and analyzed using FACS Diva software. Briefly, MCF 10A, MCF7, DU 145 and RWPE-1 cells were transferred to 12-well plates at a concentration of 10⁵ cells per well and incubated overnight at 37 °C. Alexa Fluor 647 fluorescent dye-labeled gold nanostructures were prepared in PBS (1X). The cellular uptake of gold nanostructures was investigated via incubating with cells for 1h. Cells containing only 5 % (v/v) PBS were cultivated as a control group. At the end of the incubation, the cell culture medium was collected. Each well was washed with cold PBS twice and the cells were then harvested by trypsinization on ice. The solutions were centrifuged for 5 min at 4 °C. The supernatant was removed, and the resulting pellet was resuspended in cold PBS (250 µL) for flow cytometry measurements.

CHAPTER 4

RESULTS AND DISCUSSION

The results have been presented in three different sections. In the first section, synthesis and *in vitro* evaluation of PEGylated gold nanorods (AuNRs) at different aspect ratios have been presented. The second section presents the synthesis and *in vitro* evaluation of lipid nanobubbles containing AuNRs. The third section demonstrates the conjugation of cell-specific antibody to PEGylated AuNRs and their *in vitro* evaluations.

4.1. Synthesis and *In vitro* Evaluation of Gold Nanorods (AuNRs) at Different Aspect Ratio

4.1.1. Synthesis of AuNRs, Modification with PEG and Characterization

AuNRs with different aspect ratios were synthesized using seed-mediated method followed by PEGylation via ligand-exchange method. The structural characterizations were performed using different techniques such as UV-Vis / NIR spectroscopy, SEM, AFM, ICP-MS, ELS and XPS. AuNRs exhibit specifically two different absorption peaks. The first plasmon band is transverse absorption peak which is related to the diameter of AuNRs. The second plasmon band, i.e. longitudinal absorption peak, is caused by the length of AuNRs (Eustis and El-Sayed, 2006).

There are several hypotheses in the reaction mechanism on the synthesis of AuNRs of AgNO₃, AA and CTAB effects. CTAB was used as the surfactant in the synthesis of AuNRs and CTAB is known as a good stabilizer. Surfactant molecules are present in the bilayer form around the spherical gold seed particles and AuNRs. The bilayer surfactant makes it difficult for both the gold precursor (HAuCl₄) and the reducing agent to adhere to the particle surface and slows down the growth rate of the spherical nanoparticles (Chhatre et al., 2018). In addition, both CTAB and AgNO₃ act as growth directional agents. It is also known that AA used as a mild reducing agent reduces Au

(III) to Au (I). Finally, the addition of the seed particles provides a complete reduction of Au with a catalytic effect (Ahmed et al., 2014).

Figure 4.1 shows the absorption spectra of AuNRs with different aspect ratio (AR). The spectra clearly showed both the transverse and longitudinal plasmon bands, evidencing the formation of AuNRs. With increasing AR, which can be simply defined as the ratio of the length to the diameter of AuNRs, the longitudinal plasmon peak shifted toward NIR region while the transverse band remained constant at 530 nm except for AR of 7.0. Because AuNRs with high AR were produced by a different method and smaller gold seed particles are obtained in this method. Therefore, a transverse band at 510 nm was observed for AuNRs with AR of 7.0.

The longitudinal plasmon band red-shifted from 680 to 940 nm indicating the increase in length. The intensity of the longitudinal plasmon band was also observed to increase, which was attributed to formation of AuNRs at high yield. It is well-known that the length of AuNRs is grown leading to red-shift of the longitudinal plasmon band with increasing the silver concentration and co-surfactant, NaOL. In the literature, there are several mechanisms for the role of Ag in the anisotropic growth of AuNRs. The facet-specific deposition of ionic or metallic silver onto the gold surface happen by under-potential deposition (UPD) and thus, growth along the $\langle 110 \rangle$ direction occurs due to larger atomic distance and high energy resulted in better adhesion (Ahmed et al., 2014). In accordance with these explanations, it is well-known that AgNO_3 solution effect onto vary the AR of AuNRs.

In addition, a binary surfactant mixture composed of CTAB and NaOL is used in AuNRs synthesis with high aspect ratio. The double bond in NaOL molecules reduce Au(III) to Au(I) without AA. Moreover, NaOL molecules mediate between CTAB molecules on growing facet of AuNRs (Ye et al., 2013). This increasing length of AuNRs was expected with co-surfactant since NaOL molecules possessed the more flexible nature and reducing power of double bond in their structure as well as different affinities of the two surfactants on the facets of AuNRs.

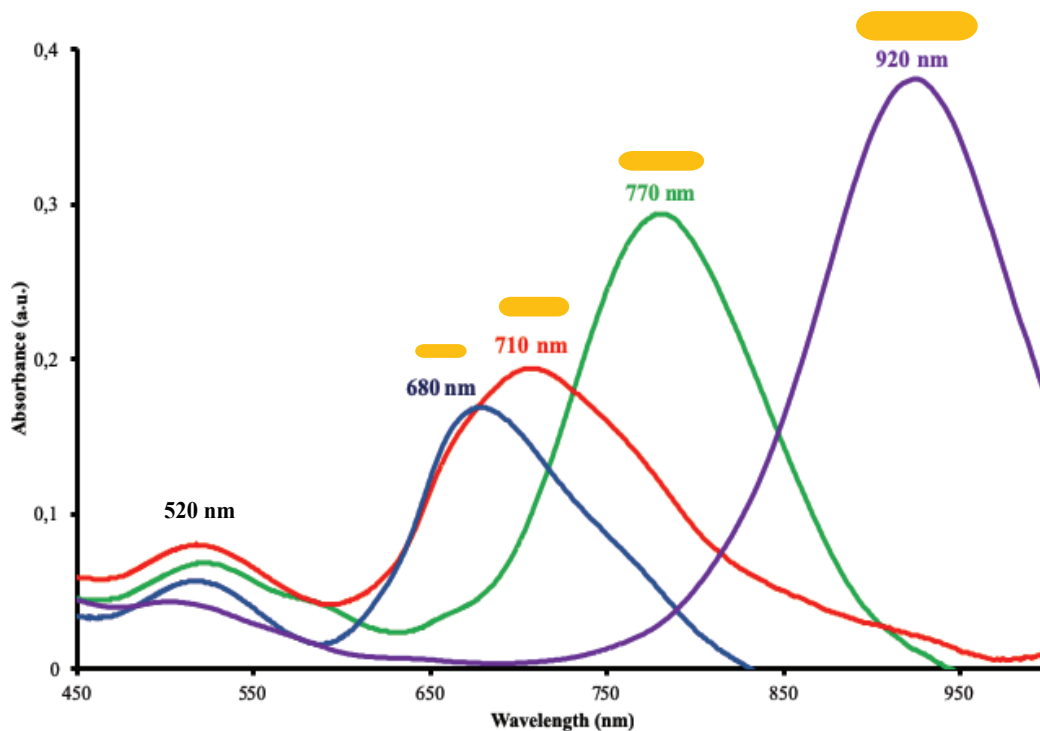


Figure 4.1. UV-Vis / NIR spectra of AuNRs prepared at different aspect ratio.

AuNRs having varying aspect ratio were investigated via SEM (Figure 4.2). Figures 4.2A-F represent the SEM images of AuNRs with varying AR (Table 3.1 in Methods Section). Sizes were estimated using Image J programme from SEM images with at least 50-100 AuNRs. From the SEM images, the dimensions of AuNRs was determined to be (A) 12.5 ± 2.5 nm, (B) 13.2 ± 1.5 nm, (C-D) 11.4 ± 2.0 nm, (E-F) 13.8 ± 1.9 nm in diameter and (A) 33 ± 3.0 nm, (B) 42.0 ± 2.3 nm, (C-D) 45.5 ± 1.5 nm, (E-F) 98.0 ± 5.9 nm in length, respectively. According to these measurements, the aspect ratio of AuNRs was calculated to be approximately 2.7, 3.2, 4.0 and 7.0. The SEM images depicted that AuNRs produced were monodisperse. In addition, SEM images showed that AuNRs were synthesized at high concentration. A very dense layer of AuNRs with AR=7.0 were monitored compared to other aspect ratios AuNRs. Moreover, AuNRs (AR=2.7, 3.2 and 4.0) with random orientations were observed in SEM images.

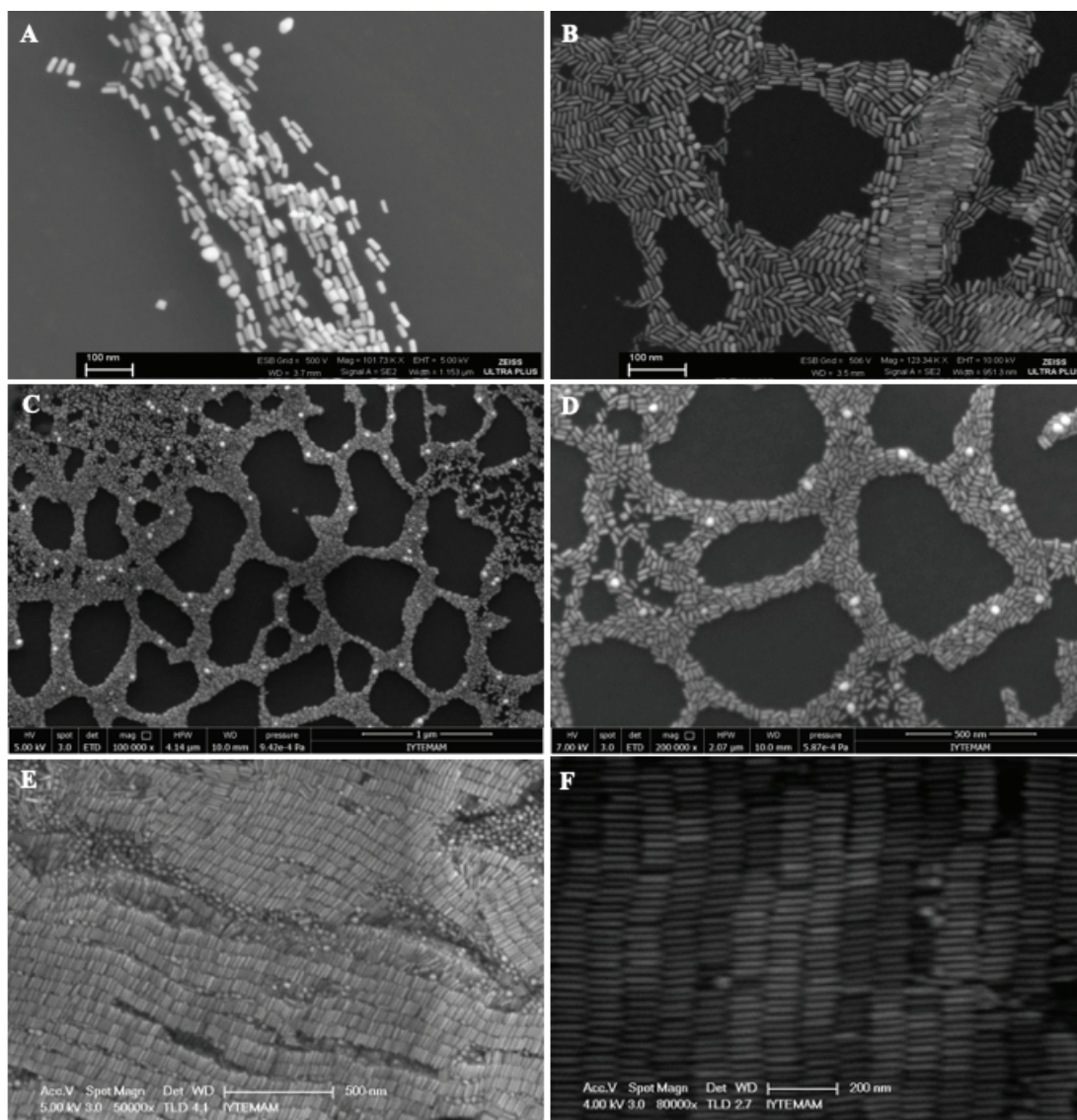


Figure 4.2. SEM images of AuNRs with (A) AR=2.7, (B) AR=3.2, (C-D) AR=4.0 and (E-F) AR=7.0.

The amount of gold in the purified AuNR solution was analyzed by ICP-MS. The gold amount in solution is proportional to the yield of AuNRs synthesis. The gold concentration was measured up to 950 ppm by ICP-MS analyses (Table 4.1). The data obtained from both the SEM and ICP-MS analyzes showed that the produced AuNRs were synthesized with high efficiency.

After producing AuNRs with desired lengths at high efficiency, the surface of AuNRs was modified with PEG to enhance their biocompatibility because CTAB-stabilized AuNRs show strong cytotoxicity (Niidome et al., 2006). PEGylation process is one of the useful techniques to make biocompatible AuNRs for medical applications. The

surface modification of AuNRs with PEG generally provides several advantages such as inhibiting of aggregation, lowering toxicity, preventing non-specific binding of proteins, enhancing colloidal stability and biorecognition ability (Jokerst et al, 2011).

Table 4.1. AuNR synthesis yields measured by ICP-MS.

AR	Gold Concentration (ppm)
2.7	245
3.2	400
4.0	580
7.0	950

PEG coated AuNRs were prepared by treating AuNRs stabilized by CTAB with a mixture of mPEG-SH and NH₂-PEG-SH. Amine functionalized PEG was used in the PEG mixture for further studies in antibody conjugation. PEGylated AuNRs were purified by dialysis or centrifugation. AuNRs exhibit well-known affinity to thiol compounds. The only (111) face of AuNRs are easily modified by thiolated compounds such as alkanethiols. The binding of thiolated molecules leads to a red shift of the plasmon due to the changes in refractive index at the surface of AuNRs (Yu and Irudayaraj, 2006). Accordingly, each functionalization step was confirmed by UV-Vis / NIR spectroscopy. Figure 4.3 illustrates the absorption spectra of AuNR suspensions before and after interaction with PEG mixture. Among synthesized AuNRs, two different AR of AuNRs were chosen (4.0 and 7.0), because their longitudinal bands were coherent with the wavelength of applied NIR lasers for *in vitro* photothermal therapy experiments. In the spectra of AuNRs with low aspect ratio (AR=4.0) (Figure 4.3A) before PEGylation, typical UV-Vis characteristic of AuNRs was observed i.e., two surface plasmon bands corresponding to the longitudinal 750 nm and transverse 520 nm oscillation modes. The longitudinal peak shifted from 750 nm to 765 nm while the transverse peak remained at approximately 520 nm after PEGylation (red spectrum). In the case of AuNRs with high aspect ratio (AR=7.0) (Figure 4.3B), the longitudinal peak at 920 nm and transverse peak at 520 nm were observed before PEGylation. After PEG interaction, the longitudinal peak shifted from 920 nm to 940 nm (red spectrum), which was attributed to the formation of

a PEG layer on the surface of AuNRs (Kopwiththaya et al., 2010). The absence of broadening of the longitudinal peak after PEGylation is indicative of a very good solubility in water of the PEGylated AuNRs (Oyelere et al., 2007).

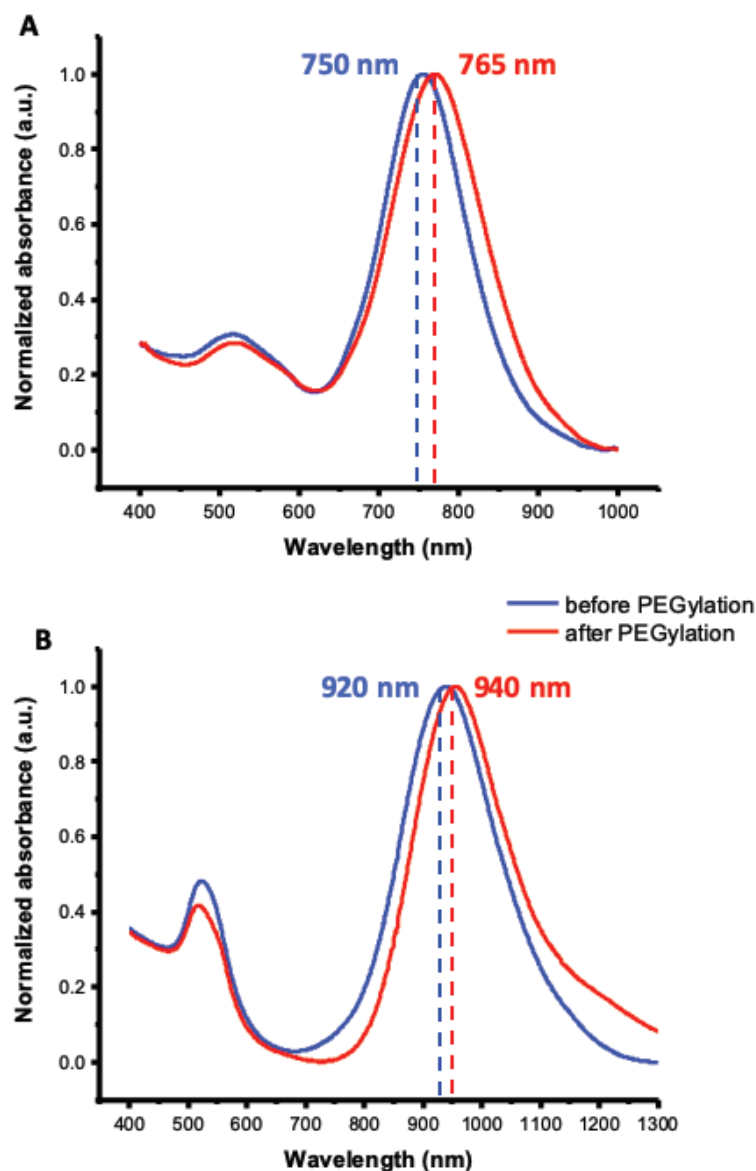


Figure 4.3. UV-Vis / NIR spectra of before and after PEG modification of AuNRs with (A) AR=4.0 and (B) AR=7.0. CTAB-stabilized AuNRs (blue spectrum) and PEG-AuNRs (red spectrum).

Figure 4.4 shows the SEM images of AuNRs after coating with the PEG mixture. According to the obtained images, it was observed that the PEG coated AuNRs were clustered regionally and they were settled one by one in some regions.

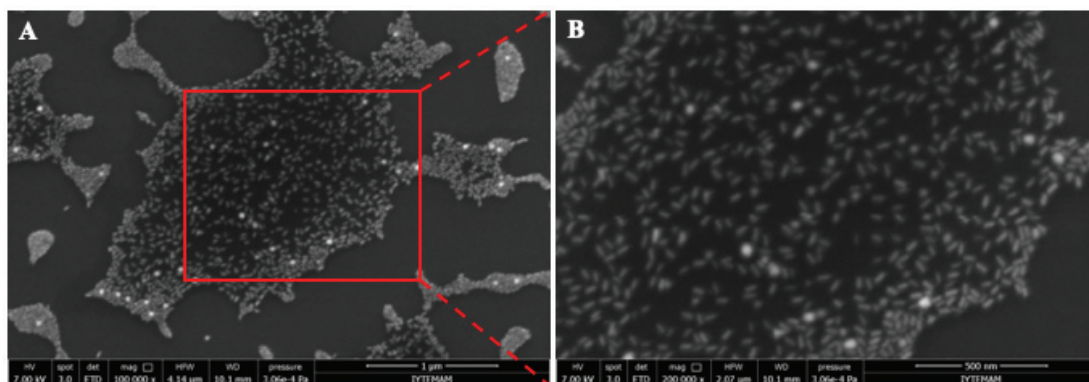


Figure 4.4. SEM images of PEG mixture coated AuNRs with different magnifications.

AFM analyses were also performed before and after modification of AuNRs with PEG mixture (Figure 4.5). Figures 4.5A and C show topography images of AuNRs, while Figures 4.5B and D are phase images of the same samples. The AFM image showed the size of AuNRs to be 20 nm in diameter and vary between 45 and 70 nm in length. These sizes were larger than the ones calculated from the SEM images. This was due to broadening effect of AFM tips and CTAB layers around AuNRs which were not visible in SEM images due to electron beam. The morphology of AuNRs changed completely after modification with PEG (Figure 4.5C and D). The PEG layer on AuNRs is clearly visible in AFM images.

The zeta potential measurement was used to prove the success of PEGylation process, showing the change in surface potential of AuNRs. The zeta potential before and after modification of AuNRs with PEG were analyzed and the results are shown in Table 4.2. AuNRs before PEGylation displayed a zeta potential of 34.9 mV. CTAB-stabilized AuNRs possess cationic surface charge as CTAB is a cationic molecule, providing colloidal stabilization around the produced AuNRs (Figure 4.5A) (Rayavarapu et al., 2010; Grabinski et al., 2011).



Figure 4.5. AFM image of PEG modified AuNRs.

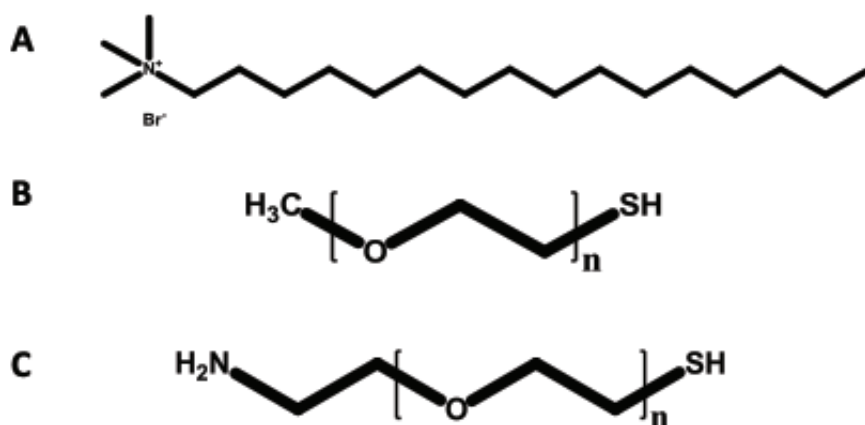


Figure 4.6. Chemical structures of (A) CTAB, (B) mPEG-thiol and (C) amine-PEG-thiol.

After PEGylation, zeta potential shifts from 34.9 mV to -4.15 mV, indicating that PEG replaced CTAB as the dominant adsorbate on the AuNR surfaces. The significant decrease in zeta potential was attributed to the removal of CTAB molecules which have quaternary ammonium groups as a hydrophilic head group (Figure 4.6A). In our experiments, a mixture of mPEG and amine-modified PEG (mol ratio of 4:1) was used (Figure 4.6B and C). The presence of mPEG is likely to shield the positive charge of amine-modified PEG. In conclusion, change of the zeta potential from positive to neutral or negative is expected during surfactant exchange from CTAB to PEG and the results

showed a successful PEGylation according to literature (Rayavarapu et al., 2010; Grabinski et al., 2011; Zhang et al., 2014).

Table 4.2. Zeta potential measurement of AuNRs (CTAB-stabilized) before and after PEGylation (n=3).

Sample	Zeta Potential in water (mV)
AuNRs before PEGylation	34.9 ± 2.1
AuNRs after PEGylation	-4.15 ± 0.9

Additionally, the PEG modification to AuNRs was also confirmed via XPS measurements. XPS is a surface-sensitive quantitative spectroscopic technique that measures the elemental composition and gives information about chemical state of the elements on a surface. XPS measurements were performed at least from three points of each sample surface. XPS spectra showing the C1s and N1s regions of AuNRs and PEGylated AuNRs were shown in Figure 4.7. In C1s spectrum, before PEGylation, the carbon peak at 283 eV was assigned to the C-C bonds in the CTAB molecules. After PEGylation of AuNRs, in addition to this major peak, carbon peak was assigned to the C-O bonds in PEG molecules. In N1s spectrum, before PEGylation, the weaker peak at 403 eV corresponded to the ammonia groups within the CTAB molecules, and after PEGylation, the stronger peak at 400 eV corresponded to the amine groups within the PEG molecules (Jakša, 2014).

From XPS experiments, the elemental composition was also determined by normalizing all measured values to Au quantity. The atomic percentages of the elements within the tested samples are summarized in Table 4.3. AuNRs before PEGylation show the elements of CTAB molecules surrounding AuNRs. Accordingly, the Br and N atom signals were clearly observed in the XPS analysis of AuNRs having CTAB as stabilizer. The Ag atom signal was also detected due to the use of AgNO₃ in AuNRs synthesis.

After PEG modification of AuNRs, the S atoms of PEG molecules which anchored to the gold surface was also observed. Besides, the Br atomic percentage was found to decrease CTAB molecules which indicated the replacement of CTAB molecules with PEG molecules on the surface of AuNRs. The low atomic percentage of nitrogen

was attributed to the embedding of functional end-group of PEG molecules in the macromolecular chain (5000 g/mol). Due to the large number of carbon atoms in PEG molecules compared to CTAB, the ratio of carbon increased after PEG functionalization to AuNRs.

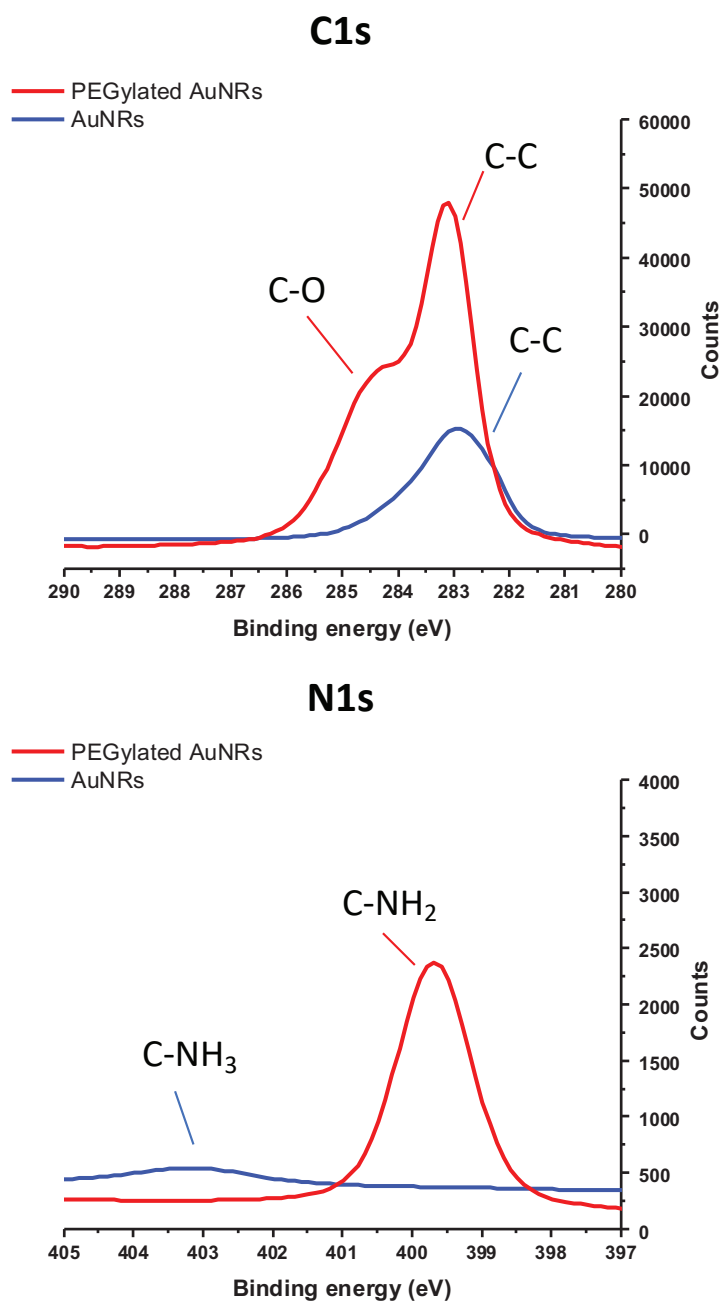


Figure 4.7. XPS spectra showing the C1s and N1s regions of AuNRs and PEGylated AuNRs.

Table 4.3. Elemental composition and atomic percentages of AuNRs and PEGylated AuNRs obtained by XPS.

Element	AuNRs	PEGylated AuNRs
C1s	11.8	26.9
O1s	3.0	4.9
N1s	0.5	0.1
S2p	-	0.1
Br3d	0.4	0.2
Ag3d	0.1	-

Overall UV-Vis / NIR spectroscopy, zeta-potentials and XPS results confirmed the binding of PEG modification onto AuNRs surfaces.

4.1.2. Photothermal Effects of AuNRs

The photothermal conversion efficiency of laser light to heat energy increases as the absorption of gold nanoparticles increases (Jiang et al., 2013). In the literature, as already proved, efficiency of the photothermal conversion is higher for AuNRs that their longitudinal plasmon bands are well match when considering the applied laser wavelength. NIR light can penetrate the tissues with little energy loss. AuNRs can convert NIR light to heat energy due to high absorption in the NIR region and this causes localized hyperthermia in the tissue. The temperature near 50 °C need to kill the tumor cells for photothermal therapy (Luo et al., 2016).

To the best of author's knowledge, there is no detailed study in the literature comparing the photothermal effects of different aspect ratio AuNRs. For this reason, photothermal effects of PEGylated AuNRs were investigated considering the potential use of these nanostructures in photothermal therapy. Results are given in Figures 4.8, 4.9 and 4.10. The photothermal effect of AuNRs at two different aspect ratios (AR= 4.0 and

7.0) was first investigated in water using AuNR solutions at varying concentrations. Both 780 nm (100 mW) and 808 nm (200 mW and 500 mW) diode lasers were used to heat the AuNR solutions. These lasers were chosen because the longitudinal plasmon band of synthesized AuNRs (AR=4.0) was in the close range to the wavelength of lasers, and in the literature, lasers in these wavelengths were mostly used for photothermal applications.

The temperature change of PEGylated AuNR solutions (AR=4.0 and AR=7.0) at varying concentrations were first examined under 780 nm diode laser irradiation at 100 mW power for 20 minutes (Figure 4.8). The temperature of AuNR aqueous solutions was observed to increase with time upon irradiation. While the heating effect of AuNRs having AR of 4.0 was observed to increase with increasing concentrations, this was not observed for AuNRs having higher AR. This might be due to laser wavelength inconsistent with the longitudinal wavelength of AuNRs (AR=7.0). AuNRs having AR of 4.0 increased the temperature of solutions above 37 °C at all concentrations tested within 12 minutes of irradiation. On the other hand, for AuNRs with AR of 7.0, the same effect was observed only at the highest concentrations (0.6 mM and 1.2 mM). Since AuNRs with AR of 4.0 interact better with the 780 nm laser compared to AuNRs with AR of 7.0, more temperature increases were observed even at the lowest concentration (0.12 mM) of AuNRs having AR of 4.0 in time dependent. The maximum temperature of AuNR aqueous solutions was observed to reach 40.7 °C for AuNRs with AR of 4.0 and 38.9 °C for AuNRs with AR of 7.0. Since the power of the laser at 780 nm is low, no more temperature increase was observed at varying concentrations of AuNRs. Photothermal effect experiments of AuNRs were continued by changing the wavelength and power of the laser as the measured maximum temperature values were not sufficient for cell death in photothermal therapy.

In Figure 4.9, the temperature change of PEGylated AuNR solutions at varying concentrations were examined under 808 nm diode laser irradiation at 200 mW power. The heating effect of both AuNRs solutions was more profound under these conditions, which was attributed to the more powerful laser and laser wavelength. Moreover, when compared with heating induced by 780 nm laser, AuNRs with higher aspect ratio heated the solution above 37 °C at lower concentrations. The maximum temperature of AuNR solutions was observed to reach 55.5 °C for AuNRs with AR of 4.0 and 53.8 °C for AuNRs with AR of 7.0. While the temperature rise for AuNRs with higher aspect ratio reaches constant values within 10 to 20 minutes, the temperature increases for AuNRs with lower aspect ratio at all concentrations.

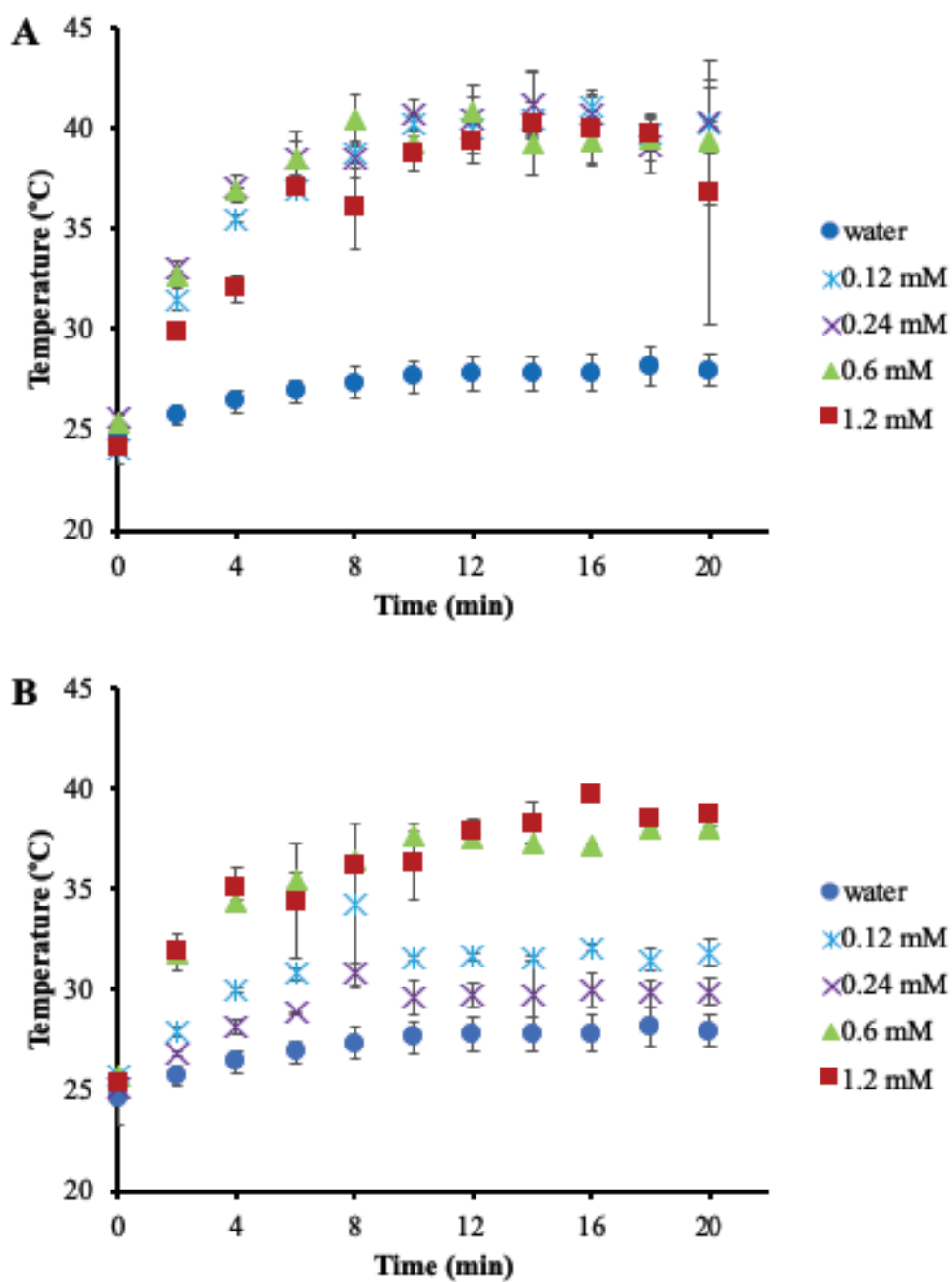


Figure 4.8. Temperature change of AuNR aqueous solutions at varying concentrations with time upon irradiation with 780 nm diode laser (100 mW). (A) AR= 4.0 and (B) AR= 7.0.

While the temperature rise of AuNRs with lower aspect ratio from laser at 200 mW was sufficient for photothermal therapy experiments, the temperature values

obtained in AuNRs with higher aspect ratio remained insufficient at low concentrations (0.12 and 0.24 mM), so the power of the laser was increased.

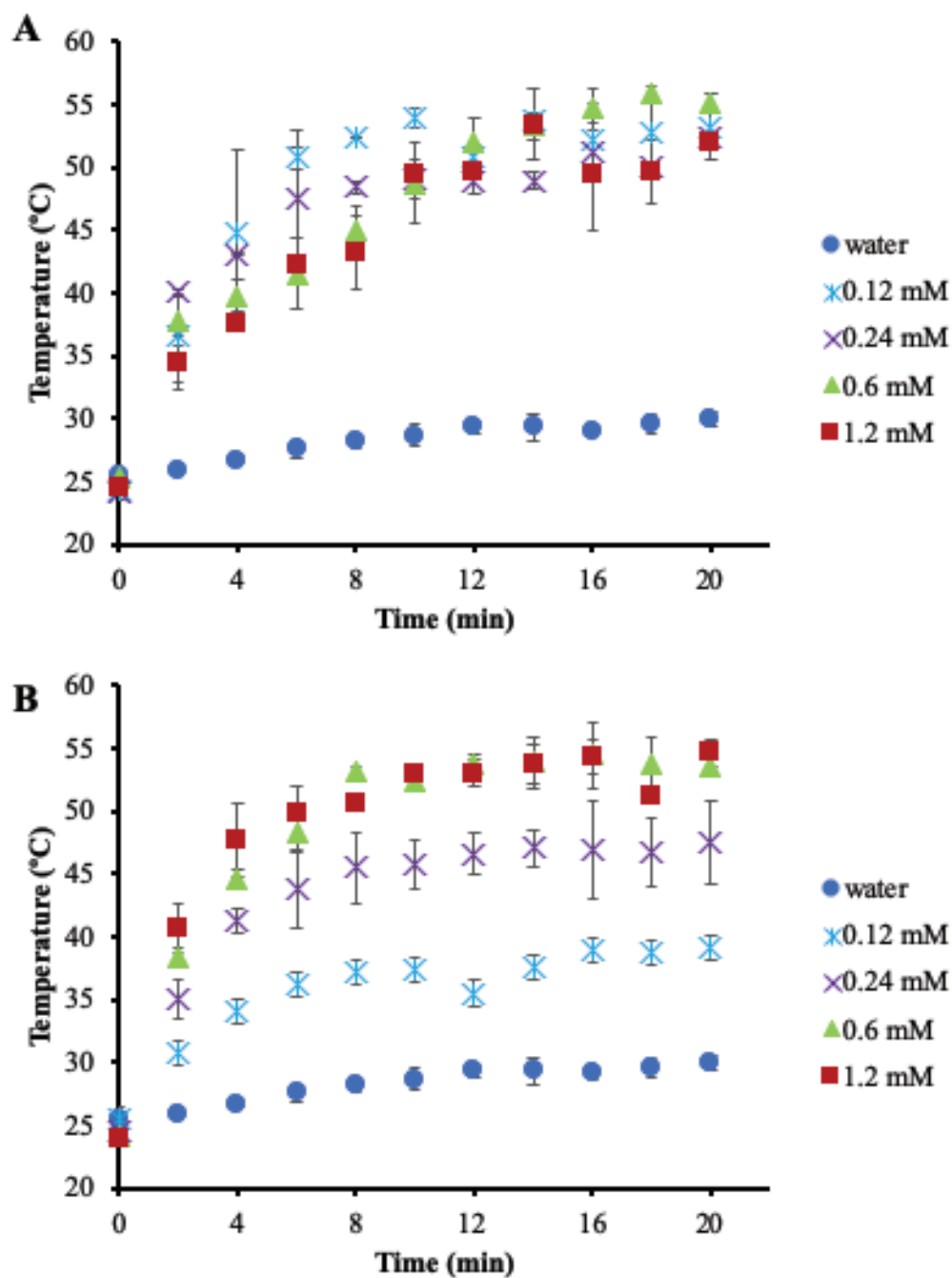


Figure 4.9. Temperature change of AuNR aqueous solutions at varying concentrations with time upon irradiation with 808 nm diode laser (200 mW). (A) AR= 4.0 and (B) AR= 7.0.

When the power of 808 nm diode laser was increased to 500 mW, the change of AuNR solution temperature drastically increased within shorter time (Figure 4.10) The maximum temperature was observed to reach 75.7 °C for AuNRs with AR of 4.0 and 73.1 °C for AuNRs with AR of 7.0. The 808 nm laser at 500 mW is more stable than the 808 nm laser at 200 mW because the temperature is fixed after a uniform temperature rise in all concentrations for both AuNRs. Sufficient temperature values were obtained both AuNRs at lowest concentration (0.12 mM) for photothermal therapy experiments. However, as expected, the higher temperature value (63.8 °C for AR of 4.0 and 50.8 °C for AR of 7.0) was measured with AuNRs of AR of 4.0 because their longitudinal plasmon band was more coherence with the laser wavelength.

Overall, significant rises in temperature were observed for all of the AuNR solutions compared to water used as negative control. The temperature rise for all samples reaches constant values within 10 to 20 minutes. AuNRs with lower AR even at the lowest concentration (0.12 mM) increased the surrounding temperature to 40.3 °C (at 100 mW) and approximately 52.9 °C (at 200 mW) and 63.8 °C (at 500 mW) depending on laser power. The temperature rises caused by AuNRs with higher AR under the same conditions remained relatively low. Considering all these results, it was concluded that AuNRs with AR=4.0 and the irradiation using 808 nm laser at high power (500 mW) for 15 min yielded the strongest photothermal effect. Hence these conditions were chosen to be utilized for *in vitro* cell culture experiments. It is also confirmed in the literature that the 808 nm laser is suitable for the photothermal effect of produced AuNRs at low aspect ratio (Liu et al, 2018).

4.1.3. *In vitro* Assessments of AuNRs

In vitro cell culture experiments were started with PEGylated AuNRs with two different AR (4.0 and 7.0). At this stage, the effects of PEGylated AuNRs on cell viability of breast epithelial cell line MCF 10A, breast cancer cell line MCF7, prostate epithelial cell line RWPE-1 and prostate cancer cell line DU 145 at varying time and doses were investigated. Firstly, IC₅₀ (50 % cell survival - 50 % cell death) values were determined by applying PEGylated gold nanorods to the breast and prostate cell lines. The 'safe dose' to be applied from the IC₅₀ values was determined and continued with these values for *in*

in vitro studies. Then, photothermal experiments were performed by applying laser on breast and prostate cancer cells in the range of safe dose.

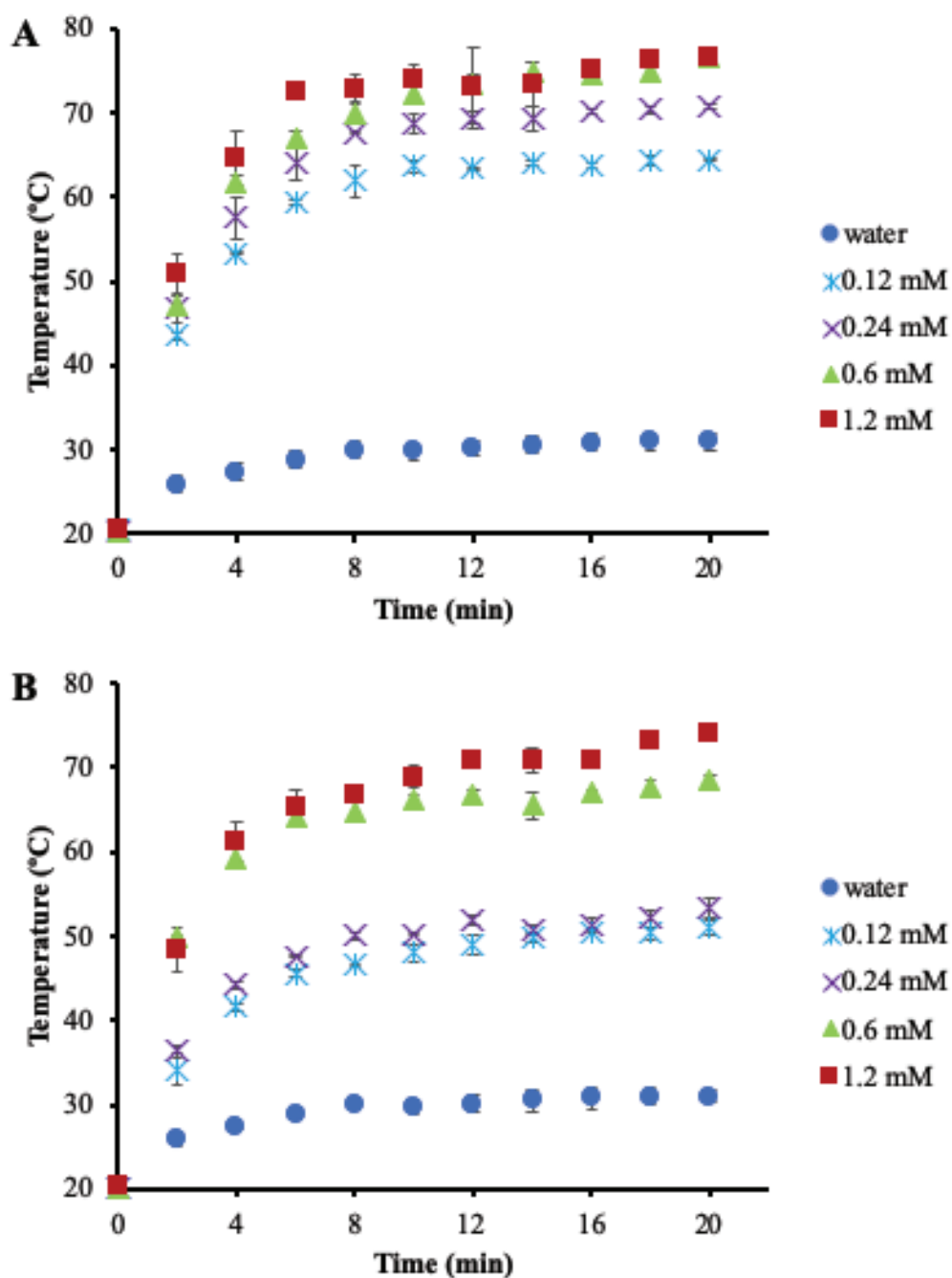


Figure 4.10. Temperature change of AuNR aqueous solutions at varying concentrations with time upon irradiation with 808 nm diode laser (500 mW). (A) AR= 4.0 and (B) AR= 7.0.

4.1.3.1. Effect of AuNRs on Cell Viability

In vitro cell viability was determined using MTT assay. First, MTT assays were performed on each cell line alone (breast cancer MCF7, breast epithelial MCF 10A, prostate cancer DU 145 and prostate epithelial RWPE-1 cell lines) by varying the cell concentrations to determine the initial number of cells that needed for testing the effect of AuNRs on the viability of cells (Figures A1 and A2 in Appendix A). According to the results, the initial cell concentration for MCF7 and MCF 10A cell lines was determined as 2.5×10^4 cell/well and for DU 145 and RWPE-1 as 5×10^4 cell/well and 10^5 cell/well, respectively. The differentiation of an initial cell concentration between the cell lines related to cell size, morphology and growing time.

To determine the effect of AuNRs with different ARs (4.0 and 7.0) on the viability of cells, four different cell lines were seeded into 96-well plates at predetermined numbers (as indicated in Materials and Methods Section 3.2.5.2). After 24 hours of incubation of cells to adhere onto plate surfaces, AuNRs (AR= 4.0 and AR= 7.0) dispersed in PBS were added to cells at varying concentrations between 0.1 mM and 1.2 mM. To the best of the author's knowledge, there is no study in the literature that examines the cytotoxic effects of modified AuNRs within a wide dose range. In the control group, only PBS was added into the cells. After 24 hours of incubation, the viability of cells was determined by MTT assay. The results are given in Figures 4.11 and 4.12. It was observed that both AuNRs showed dose and cell type-dependent cytotoxicity.

Following 24 h incubation of AuNRs, dose dependent viability was also investigated for DU 145 and RWPE-1 cell lines (Figure 4.12). Importantly, as RWPE-1 human epithelial prostate cells were easily affected by external conditions, serious problems were encountered with the growth of this cell line. As a result, the number of cells available was relatively less and the toxicity of AuNRs on RWPE-1 cells was assessed at only two concentrations.

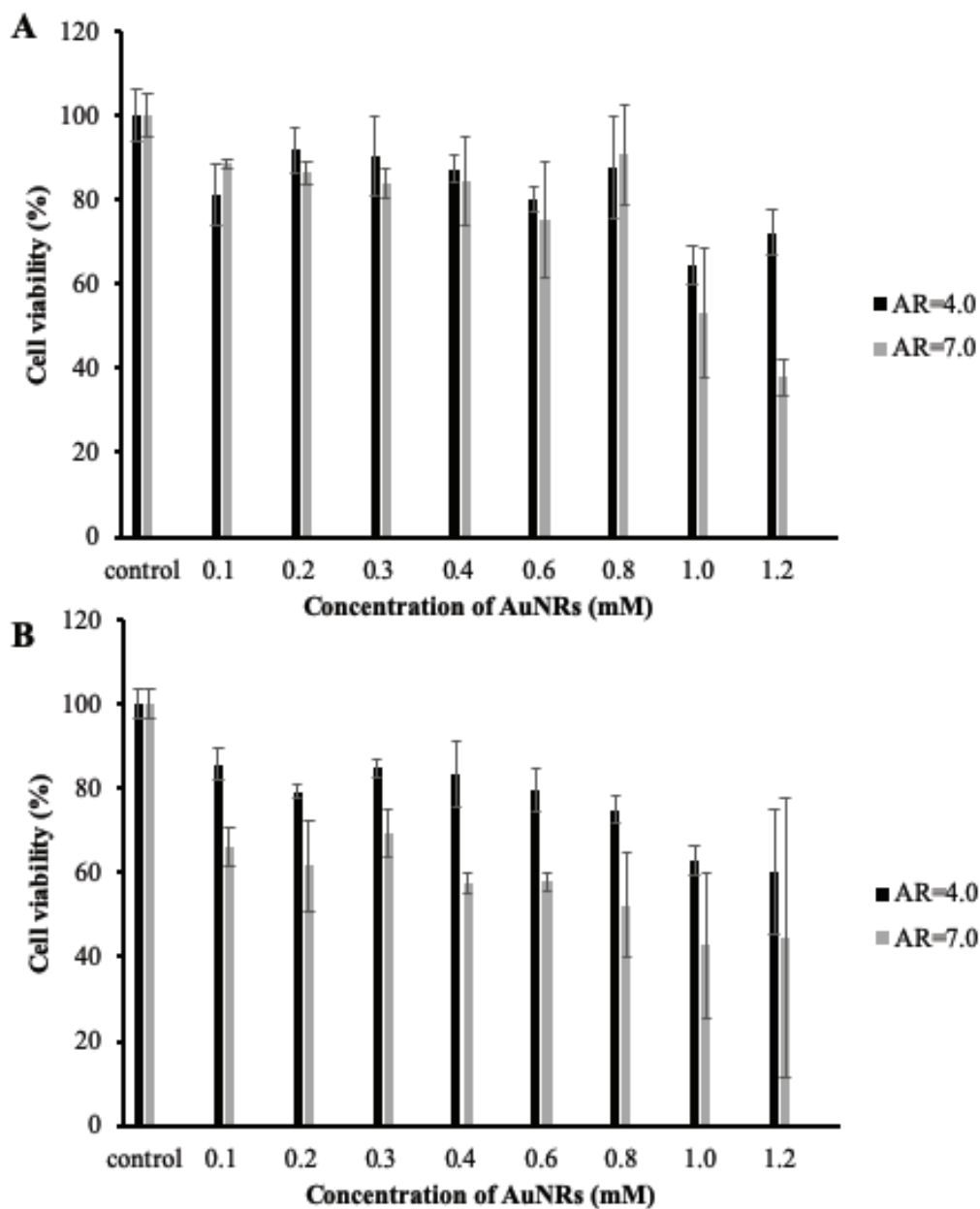


Figure 4.11. Viability of human breast (A) cancer MCF7 and (B) epithelial MCF 10A cells after 24-h incubation with varying doses of AuNRs at two different aspect ratios (AR=4.0 and AR= 7.0).

The IC_{50} value of AuNRs for each cell line is presented in Table 4.4. At the tested doses, while IC_{50} values of AuNRs with AR=4.0 were 2.2 mM and 1.6 mM, IC_{50} values of AuNRs with AR=7.0 were 1.2 mM and 0.8 mM for MCF7 and MCF 10A, respectively. According to DU 145 results, IC_{50} values of AuNRs with AR=4.0 was 1.3 mM, AuNRs

with AR=7.0 was 0.7 mM. Prostate cancer cells were observed to be affected more by AuNRs compared to breast cancer cells.

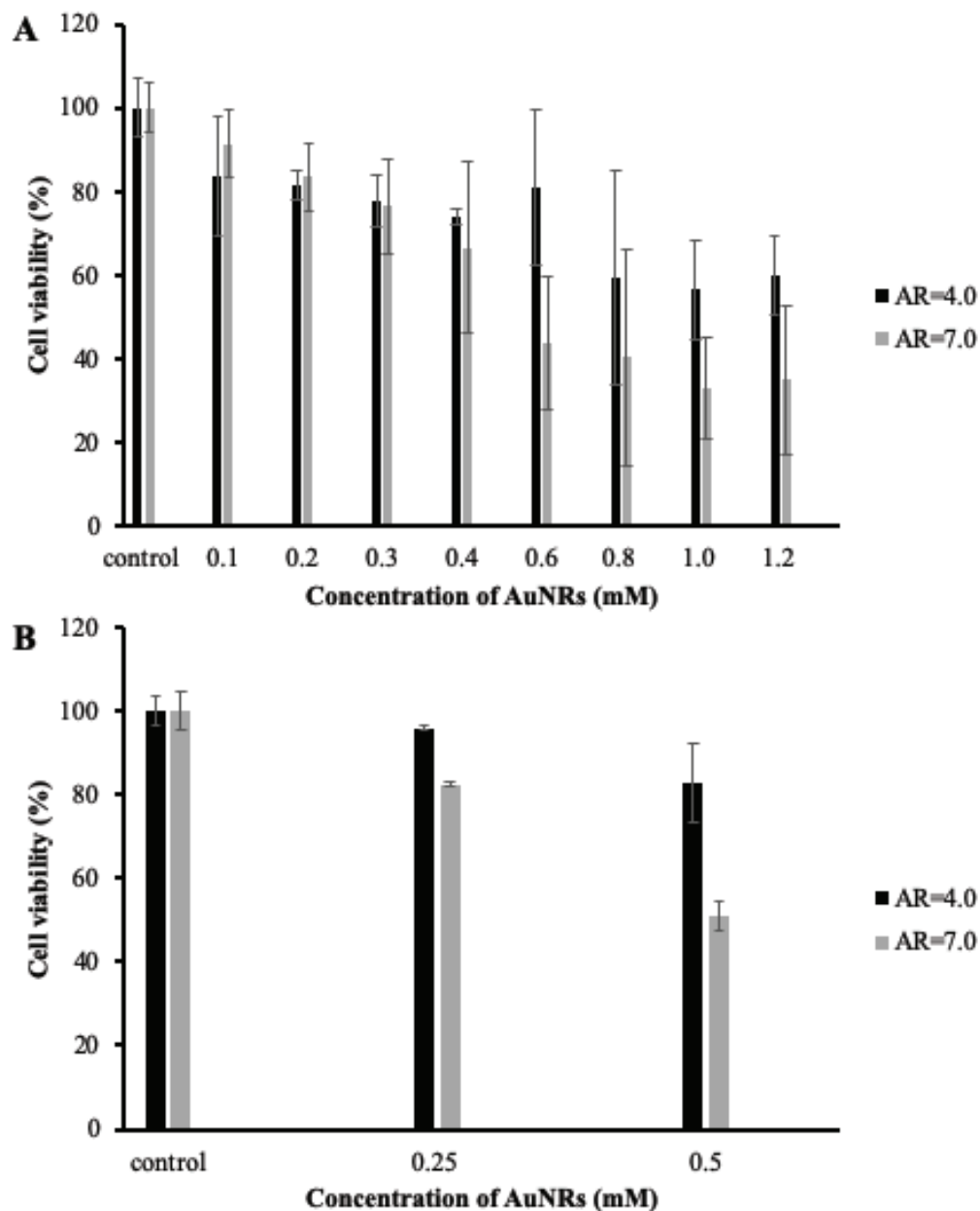


Figure 4.12. Viability of human prostate (A) cancer DU 145 and (B) epithelial RWPE-1 cells after 24-h incubation with varying doses of AuNRs at two different aspect ratios (AR=4.0 and AR= 7.0).

The cell membranes are negatively charged due to a large amount of phosphate groups on their surfaces. The positively charged of CTAB-stabilized AuNRs show strong cytotoxicity and CTAB-stabilized AuNRs can electrostatically interact and damage the cell membrane (Niidome et al., 2006). PEG-coated AuNRs show low toxicity owing to decreased unspecific binding with cell membranes. The cytotoxicity of AuNRs also depends on the aspect ratio (Wang et al., 2015). Overall the viability results showed that PEGylated AuNRs with higher AR has higher toxicity when compared to AuNRs (AR=4.0). According to the results of the cytotoxicity experiments, 0.7 mM concentration was chosen as 'safe dose' for AuNRs with AR=4.0 and 0.3 mM for AuNRs with AR=7.0.

Table 4.4. IC₅₀ values of AuNRs with different ARs (4.0 and 7.0) for each cell line.

Sample	MCF7	MCF 10A	DU 145	RWPE-1
AuNRs (AR=4.0)	2.2 mM	1.6 mM	1.3 mM	ND
AuNRs (AR=7.0)	1.2 mM	0.8 mM	0.7 mM	ND

4.1.3.2. Cell Uptake

To compare cellular uptake efficiency of PEGylated AuNRs (AR=4.0 and AR=7.0), the uptake of AuNRs was quantitatively analyzed. In the cell uptake experiments, PEGylated AuNRs (AR=4.0 and AR=7.0) (0.1 mM) were incubated with breast and prostate cancer cells for 1 hour and after incubation, the cell samples were analyzed by ICP-MS. Only cells (containing 5 % PBS) containing cells were used as a control group. The results are given in Figure 4.13.

Nanoparticles are uptaken by cells through endocytosis; phagocytosis mechanism for large particles and pinocytosis for fluids. Neutral and negatively charged NPs interact less with a negative charged cell membrane (Ahn et al., 2013).

According to the results, the uptake of AuNRs with AR ratio of 4.0 was 2 % for

MCF7 cells and 5 % for DU145 cells compared to control. For AuNRs with higher aspect ratio, the uptake was 15 % by MCF7 cells, and 25 % by DU 145 cells. PEGylated AuNRs with higher AR was taken by both cell types more than those with lower AR. This finding supports the literature indicating that nanomaterials with high aspect ratio have higher interaction with biological membranes (Lee et al., 2014; Fubini et al., 2011).

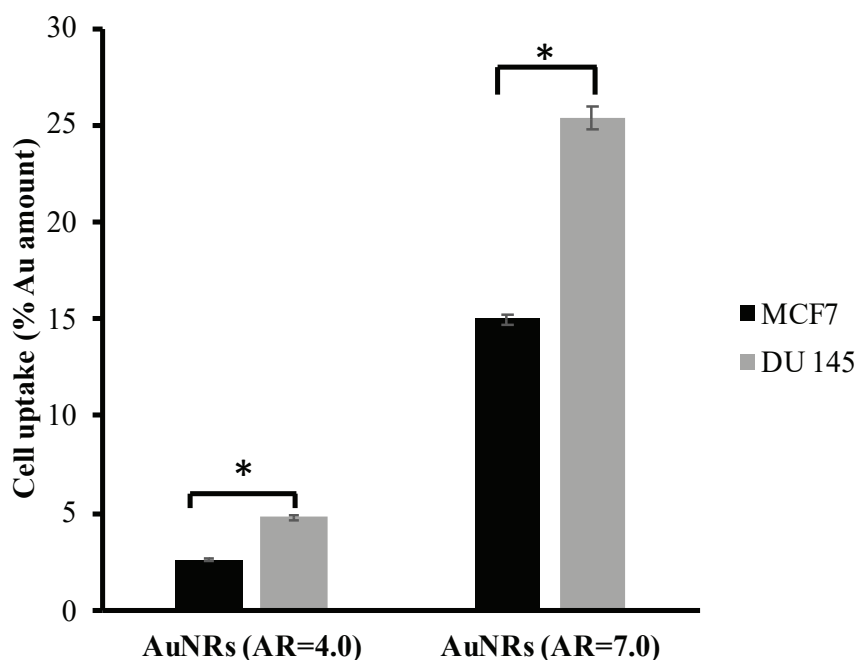


Figure 4.13. Uptake of PEGylated AuNRs (AR=4.0 and AR=7.0) by DU 145 prostate and MCF7 breast cancer cells determined by ICP-MS. Data were analyzed by t-test. (n = 3; * p < 0.05).

The cell uptake results supported the cytotoxicity results. The higher uptake of AuNRs (7.0) might be contributing to their higher toxicity. Thus, IC₅₀ values of AuNRs with AR of 7.0 were lower for all cell lines compared to AuNRs with AR of 4.0. From the cellular uptake results, it was concluded that both AuNRs were uptaken by prostate cancer cells more than breast cancer cells, which was consistent with the IC₅₀ values of AuNRs having AR of 4.0 being higher for breast cancer cells than prostate cell line.

4.1.3.3. Photothermal Ablation of Cells

AuNRs are promising materials for ablation of cancerous tumors and cells without affecting the surrounding tissues. A method reported in the literature was used in photothermal therapy experiments (Li et al., 2018). *In vitro* photothermal experiments were performed using DU 145 human prostate cancer and MCF7 human breast cancer cells. Since the heat tolerance of cancer cells is lower than healthy cells, localized hyperthermia by photothermal treatment selectively destroy the cells by denaturing the membrane of cancer cells (Luo et al., 2016). Therefore, cancer cells were chosen for photothermal therapy experiments. The reached temperature near or above 50 °C can ablate cancer cells and localized hyperthermia induce cell necrosis increasing the temperature by irradiating laser light (Niidome et al., 2006).

In these experiments, AuNRs with different aspect ratio (AR=4.0 and 7.0) were used. Briefly, cells were seeded into 96-well plates and let to adhere for 24 hours. AuNRs were then added and incubated with cells for 24 hours. AuNRs doses were chosen to be below the safe dose. Since the safe dose of AuNRs with AR of 7.0 were lower than AR of 4.0, AuNRs dose was determined as 0.2 mM concentration for both AuNRs. At the end of 24 h incubation, cells were irradiated with 808 nm diode laser (500 mW) for 15 mins without removing the medium. Control groups included cells without laser irradiation, cells after laser irradiation, and cells incubated with AuNRs (both ARs) without laser irradiation. Cell viability was measured by MTT assay. Viability results were calculated as percentage value relative to non-irradiated cells. The results are depicted in Figures 4.14 and 4.15 for AR of 4.0 and AR of 7.0, respectively.

A statistically slight decrease in the viability of MCF7 and DU 145 cells incubated with AuNRs having an AR of 4.0 (0.2 mM) after exposure to laser light was observed (Figure 4.14). Cell viability decreased to about 73 ± 4.5 % for MCF7 cells and 68 ± 2 % for DU 145 cells, relative to control after irradiation with laser light.

Photothermal effect experiments were also performed with AuNRs having an AR=7.0 (0.2 mM). No statistically significant decrease in the viability after exposure to laser light was observed in both cancer cell types (Figure 4.15).

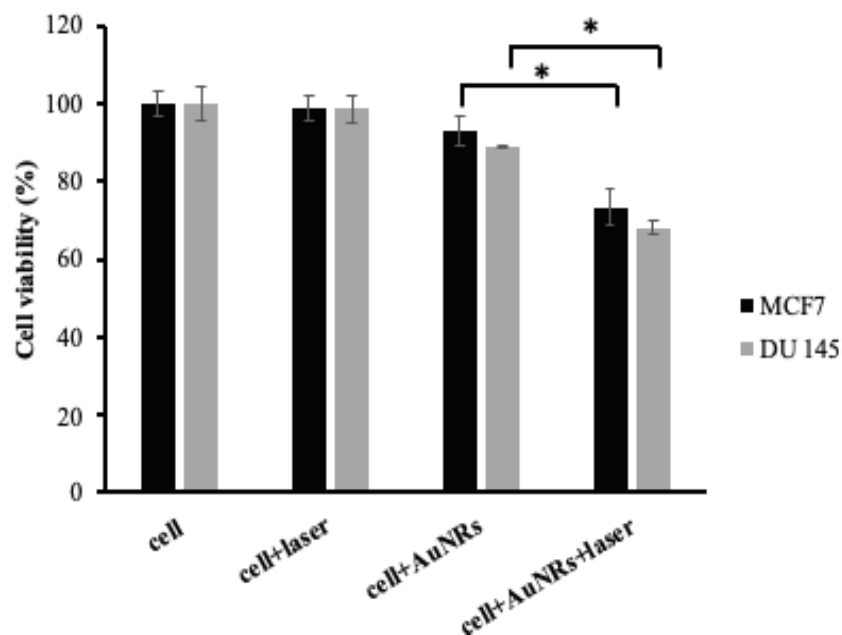


Figure 4.14. The viability of MCF7 human breast and DU 145 human prostate cancer cells incubated with AuNRs (0.2 mM) having an AR (4.0) after exposure to laser light at 808 nm (500 mW) for 15 mins. Control is the cells only. Data were analyzed by t-test. (n = 3; * p < 0.05).

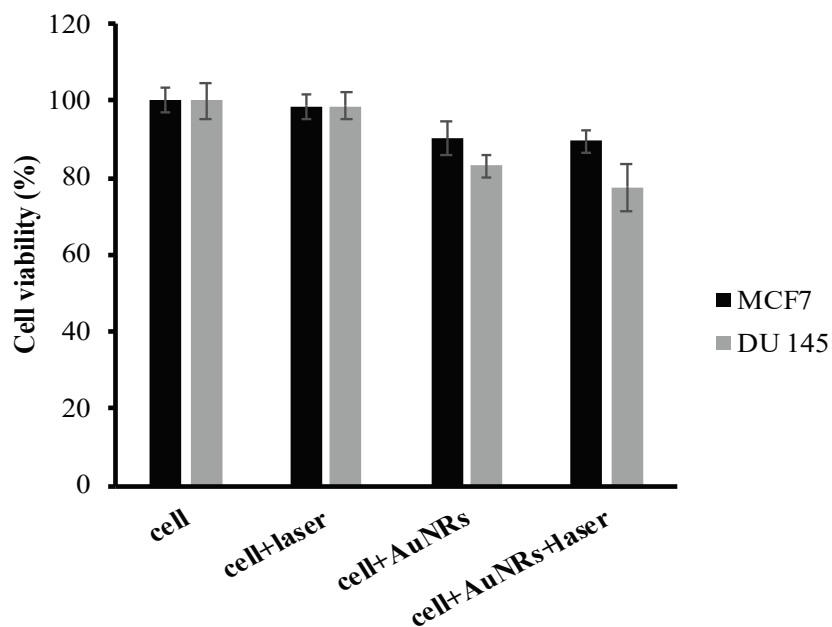


Figure 4.15. The viability of MCF7 human breast and DU 145 human prostate cancer cells incubated with AuNRs (0.2 mM) having an AR (7.0) after exposure to laser light at 808 nm (500 mW) for 15 mins. Control is the cells only. Data were analyzed by t-test. (n = 3; * p < 0.05)

Cell viability decreased to about 89 ± 3 % for MCF7 cells and 77 ± 6 % for DU 145 cells, relative to control after irradiation with laser light (Figure 4.15). However, these cell viability values obtained after laser irradiation were very close to the viability values without laser irradiation. Therefore, it is not possible to say that AuNRs with AR of 7.0 caused to cell death by hyperthermia with this laser. Since these AuNRs (AR=7.0) were taken more than AuNRs (AR=4.0), they were expected to show higher toxicity without laser treatment.

AuNRs dose was then increased to 0.5 mM for AR= 4.0. The results are presented in Figures 4.16 for MCF7 and DU 145 cells. A statistically significant decrease in the viability of MCF7 cells and DU 145 cells incubated with AuNRs having an AR of 4.0 (0.5 mM) after exposure to laser light was observed. Cell viability decreased to about 25 ± 8 % and 20 ± 4 % for MCF7 cells and DU 145 cells, respectively.

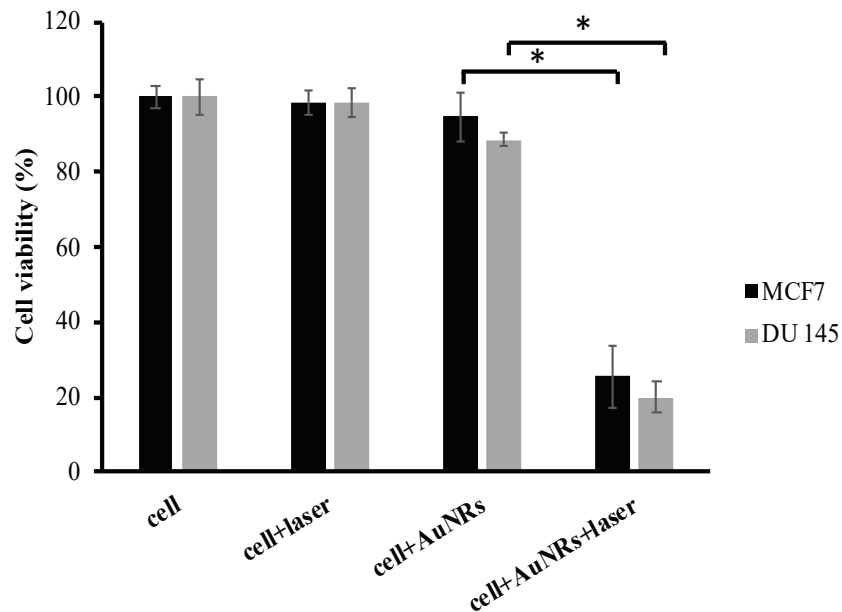


Figure 4.16. The viability of MCF7 human breast and DU 145 human prostate cancer cells incubated with AuNRs (0.5 mM) having an AR (4.0) after exposure to laser light at 808 nm (500 mW) for 15 mins. Control is the cells only. Data were analyzed by t-test. (n = 3; * p <0.05).

No significant difference in the viability of MCF7 cells was observed between the control groups. On the other hand, only a slight decrease in the viability of DU 145 cells

treated with AuNRs having an AR of 4.0 (without laser irradiation) was observed, probably due to the cytotoxic effect of AuNRs. Both in Figures 4.14 and 4.16, AuNRs (AR=4.0) effectively killed cancer cells under NIR irradiation.

Consequently, AuNRs with AR of 4.0 caused significant cell death upon irradiation under laser at 808 nm (500 mW) for 15 min, consistent with the photothermal effect results obtained with AuNR aqueous solutions. When the concentration of AuNRs increased, the amount of destroyed tumor cells increased.

4.2. Part II: Lipid-stabilized Gold Nanostructures

The aim of the second part of the thesis was to synthesize lipid-stabilized AuNR-based nanostructures. Lipids are hydrocarbon-based biomolecules which build structure and function of living cells. Lipids are widely used in therapeutic applications because of their biocompatibility and intracellular escape property. AuNR-based nanostructures stabilized with biocompatible lipids may improve therapeutic applications of AuNRs. Accordingly, in this part of the thesis, new methods have been developed to synthesize (i) AuNRs in the presence of lipid stabilizers and (ii) lipid-based nanobubbles containing multiple AuNRs (AuNBs). The resulting nanostructures were characterized via UV-Vis/NIR spectroscopy, SEM, AFM, and zeta potential measurements, as described below. The cytotoxicity and photothermal effect of AuNBs were also investigated via *in vitro* experiments.

4.2.1. Synthesis of Lipid-stabilized AuNRs

In the literature, production of gold nanoparticles (AuNPs) using lipids have been reported (Zhang et al., 2006). However, to the best of the author's knowledge, synthesis of lipid-stabilized AuNRs has not been performed yet. This thesis provides the first attempts for synthesis of lipid-stabilized AuNRs in the literature. For this purpose, an existing method reported in the literature for the AuNR synthesis was adapted with small variations (Smith and Korgel, 2008). Based on the method used for the production of

seed-mediated AuNRs, CTAB used as stabilizer was replaced with different lipids or lipid mixtures to synthesize AuNRs stabilized with lipids instead of CTAB. Lipids and lipid mixtures used in the synthesis of lipid-stabilized AuNRs are given in Table 3.2 (Chapter 3-Lipid-stabilized AuNRs Synthesis). Chemical structures of lipids were displayed in Figure 4.17.

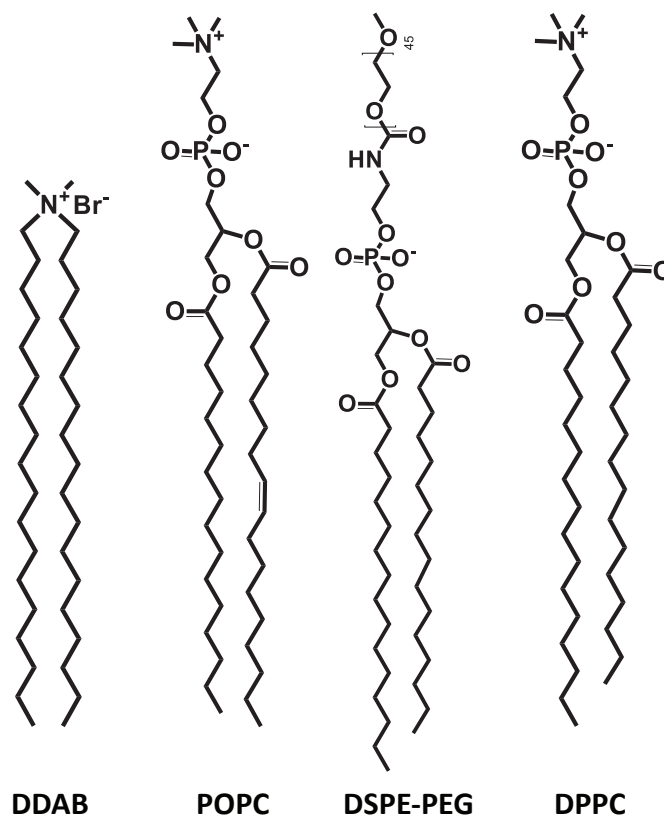


Figure 4.17. Chemical structures of DDAB, POPC, DPSE-PEG and DPPC.

Since DDAB has been used in the production of lipid-stabilized AuNPs in many studies, DDAB was first used in the experiments. DDAB is a cationic lipid and constitutes a reasonable alternative to cationic amphiphilic stabilizer CTAB, commonly used in AuNRs synthesis. When DDAB was used instead of CTAB in the AuNR synthesis method, dominantly nanospherical structures were observed at almost all concentrations (10-40 mM) tested (Figure 4.18). UV-Vis spectroscopy analysis showed that the highest yield of the AuNR production was obtained when DDAB concentration was 15 mM in

the seed solution and 40 mM in the growth solution. Figure 4.18A shows the UV-Vis spectrum of AuNPs prepared using 15 mM DDAB in seed and growth solutions. As can be seen, it is evident from the presence of a plasmon peak at only 530 nm that the AuNPs obtained are not rod-shaped. The UV-Vis spectrum of AuNRs produced using 15 mM DDAB in the seed solution and 40 mM in the growth solution is shown in Figure 4.18B. In this spectrum, the presence of transverse plasmon peak at 530 nm and longitudinal plasmon peak around 620 nm proves that there are nanorod structures along with the nanoparticles. The high intensity of the transverse plasmon peak of AuNRs compared to the longitudinal peak from the spectrum in the Figure 4.18B indicates that AuNPs formation is more than AuNRs. Figure 4.18C and 4.18D show the corresponding SEM images. The formation of AuNRs as indicated by red arrows in Figure 4.18D is clearly observed.

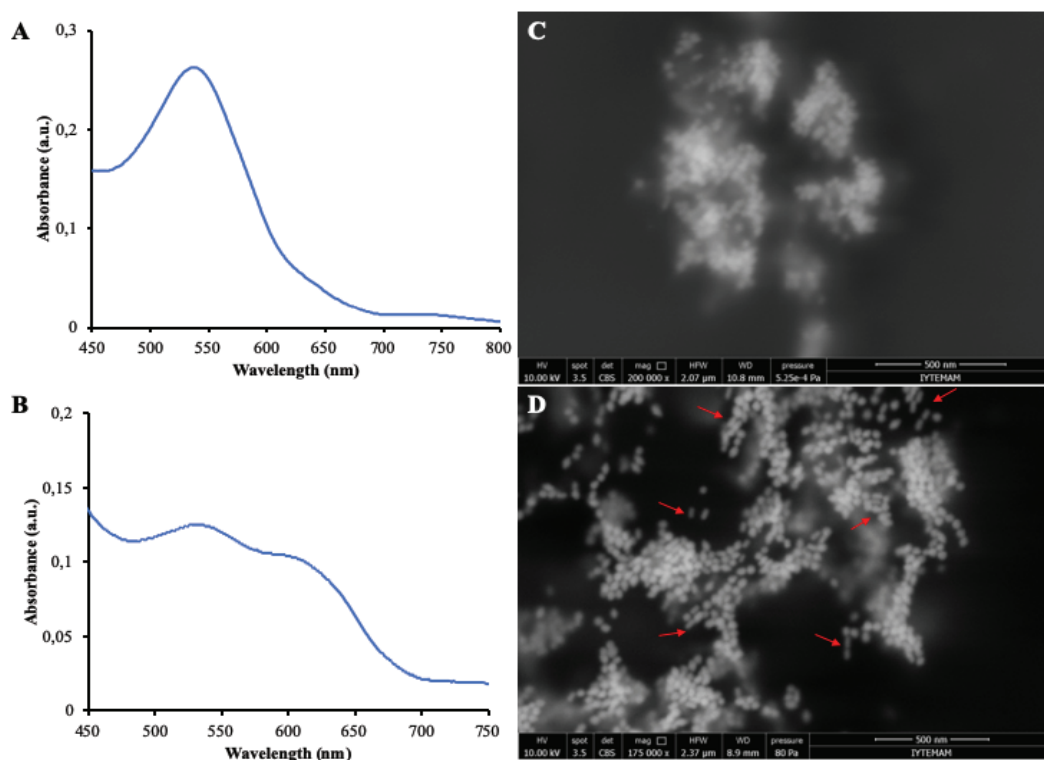


Figure 4.18. UV-Vis spectra (A-B) and SEM images (C-D) of lipid-stabilized AuNPs prepared using DDAB (A and C) 15 mM in seed and 15 mM in growth, and (B and D) 15 mM in seed solution and 40 mM in growth solution.

Separately, a PEGylated phosphoethanolamine (PE) derivative, DSPE-PEG was used for the AuNR synthesis. Experiments were performed at a concentration range between 0.5 μM and 1 mM as shown in Table 3.2. Figure 4.19A shows the UV-Vis spectrum of AuNPs produced using DSPE-PEG at a concentration of 1 mM in seed and growth solutions. Spectrum results showed a single peak at 530 nm showing the formation of AuNPs only. Also, SEM analysis showed the presence of AuNPs along with liposomal structures produced by DSPE-PEG lipids (Figures 4.19B and 4.19C).

Based on these results, DDAB was found to be a suitable lipid for synthesis of AuNRs with good yield. However, DDAB is a cationic lipid and its toxicity has been reported in the literature (Filion and Philips, 1997). To reduce the potential toxicity of DDAB-stabilized AuNRs, DDAB was mixed with biocompatible lipids such as DSPE-PEG, DPPC and POPC.

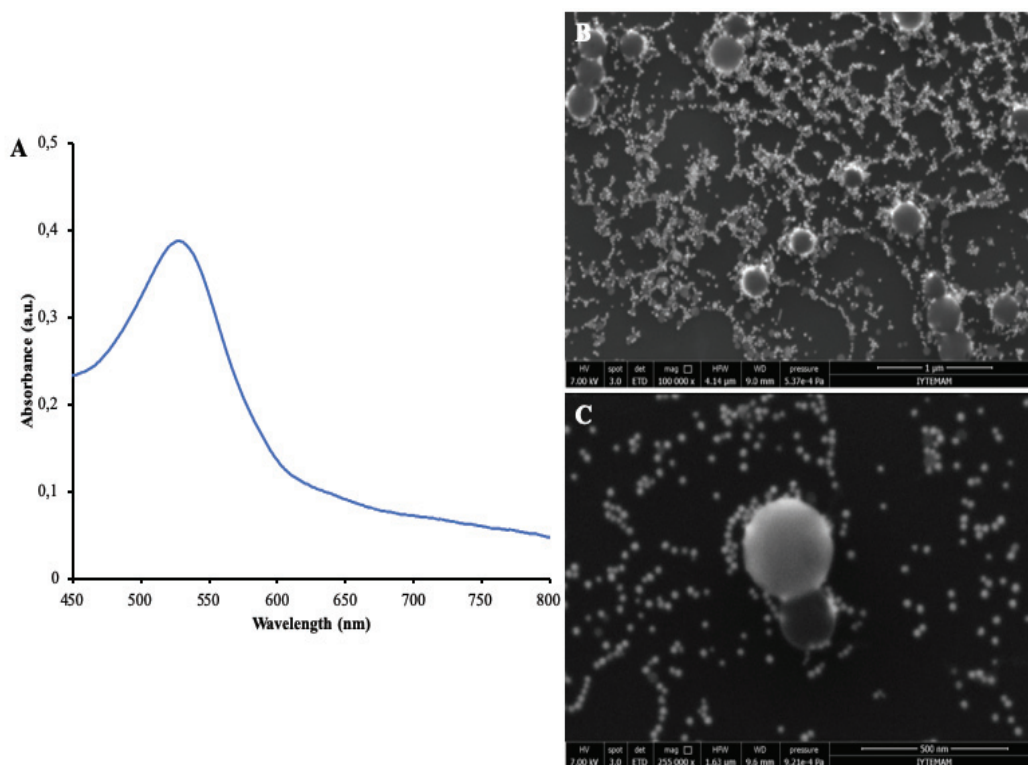


Figure 4.19. (A) UV-Vis spectra and (B-C) SEM images of lipid-stabilized AuNPs prepared with 1 mM DSPE-PEG.

First, DDAB: DSPE-PEG mixture (at a mol ratio of 3:1) was tested. Total lipid concentration was 15 mM in the seed and growth solutions. Figure 4.20A shows the UV-Vis spectrum of AuNRs produced by DDAB: DSPE-PEG mixture. Spectrum shows two peaks at 530 nm and 650 nm, showing the formation of AuNRs. Also, SEM images of AuNRs produced by this lipid mixture are given in Figures 4.20B and 4.20C. AuNRs formation at high yield was clearly observed with DDAB: DSPE-PEG mixture at a mol ratio of 3:1. Compared to the results obtained with DDAB only, the addition of DSPE-PEG to DDAB increased the length of AuNRs as well as the yield. The shift of the longitudinal plasmon peak in the UV-Vis spectrum and the increase in intensity of the longitudinal peak relative to the transverse plasmon peak (Figure 4.20A) support this finding.

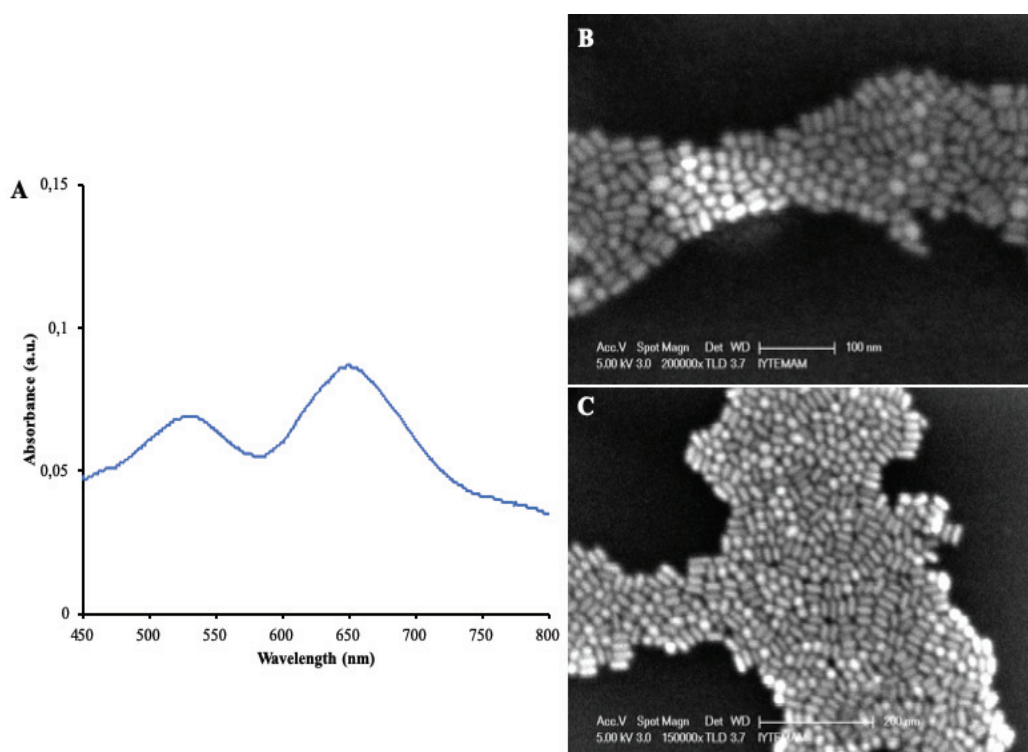


Figure 4.20. (A) UV-Vis spectrum and (B-C) SEM images of lipid-stabilized AuNRs prepared with DDAB: DSPE-PEG (at a mol ratio of 3:1) mixture.

When the mol ratio of DDAB: DSPE-PEG was increased to 14:1 (total lipid concentration=13 mM in seed and growth solutions), the length of AuNRs decreased. The

UV-Vis spectrum and SEM images of AuNRs produced using DDAB: DSPE-PEG mixture at a mol ratio of 14:1 are shown in Figure 4.21. As can be seen from the UV-Vis spectrum in Figure 4.21A, the presence of transverse plasmon peak at 530 nm and longitudinal plasmon peak around 590 nm confirms the formation of AuNRs in small size. The SEM image in Figure 4.21B also demonstrates that smaller AuNRs were obtained compared to AuNRs synthesized using a ratio of 3:1. When the amount of DSPE-PEG was decreased in the lipid mixture, AuNRs length was found to decrease, leading to the formation of AuNPs.

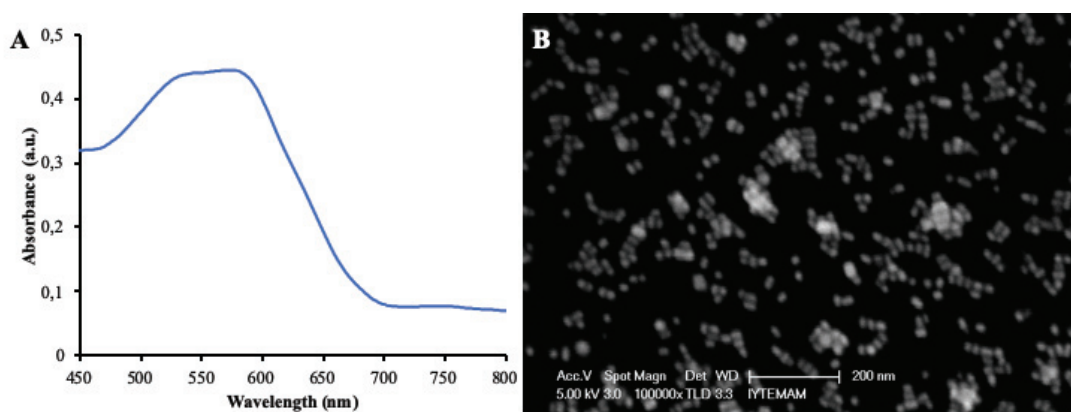


Figure 4.21. (A) UV-Vis spectrum and (B-C) SEM images of lipid-stabilized AuNRs prepared with DDAB: DSPE-PEG (at a mol ratio of 14:1) mixture.

In a new set of experiments, DDAB was mixed with POPC, a phosphatidylcholine (PC) derivative since it has a quaternary ammonium head group similar to CTAB. DDAB: POPC lipid mixture at two different mol ratios (2.7:1 and 0.9:1) was utilized. Figure 4.22 shows the UV-Vis spectrum and SEM images of AuNPs prepared with DDAB: POPC mixture at a mol ratio of 2.7:1. Total lipid concentration was 14 mM in seed and growth solutions. From the UV-Vis spectrum, there are two plasmon bands which are the transverse plasmon peak at 540 nm and longitudinal plasmon peak around 620 nm. Figures 4.22B and 4.22C present SEM images showing that AuNRs were higher amount than AuNPs.

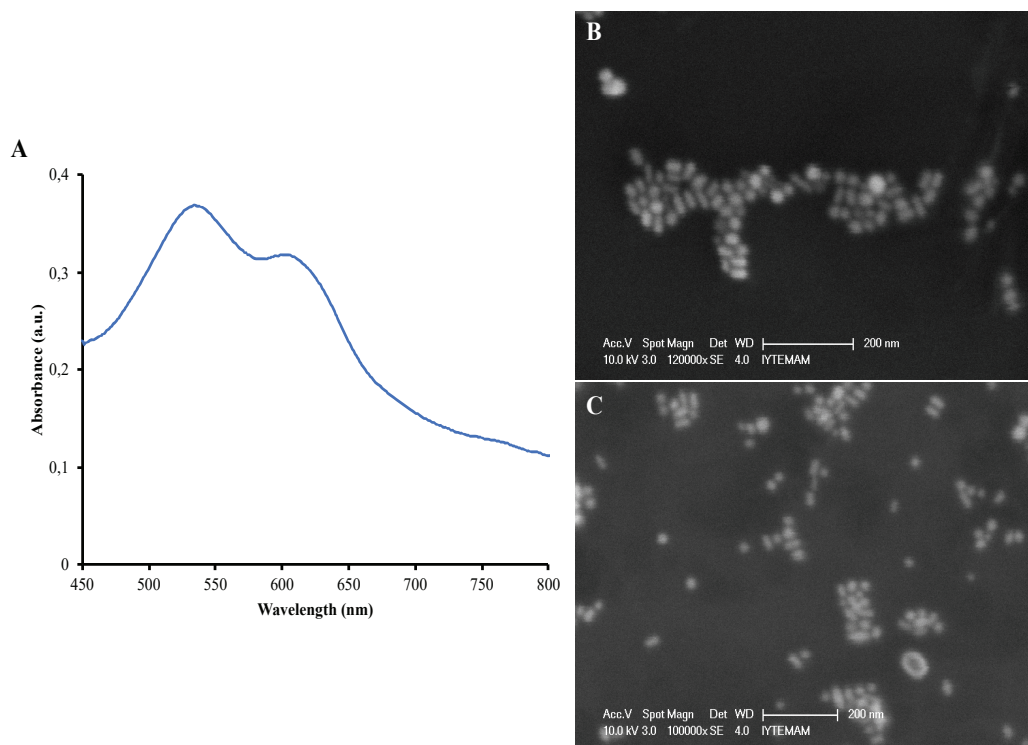


Figure 4.22. (A) UV-Vis spectrum and (B-C) SEM images of lipid-stabilized AuNRs prepared with DDAB: POPC (at a mol ratio of 2.7:1) mixture.

When the DDAB: POPC mixture was increased to a mol ratio of 27.3:1 (total lipid concentration was maintained almost the same, which was 12 mM), AuNRs were observed to form at a higher proportion with respect to AuNPs. Figure 4.23 shows the UV-Vis spectrum and SEM images of AuNRs produced by DDAB: POPC mixture at a mol ratio of 27.3:1. Two plasmon bands were acquired from the spectrum, at 530 nm and 675 nm. Also, AuNRs formation was more dominant than AuNPs, as indicated by the increase in the proportion of longitudinal band to the transverse band. SEM images of AuNRs produced by DDAB: POPC lipid mixture (at a mol ratio of 27.3:1) are given in Figure 4.23B and 4.23C. Images show the presence of AuNRs. As expected, when DDAB was increased in the lipid mixture, it led to the formation of AuNRs.

While the synthesis of AuNRs was successful using the binary lipid mixtures of DDAB, ternary lipid mixtures were also investigated to further reduce the ratio of DDAB in the final lipid-stabilized AuNR structure. For this purpose, DDAB: POPC: DSPE-PEG mixture at two different ratios (30:1:2.8 and 40:1:2.8) was investigated. Figure 4.24A exhibits the absorption spectra of AuNRs with DDAB: POPC: DSPE-PEG lipid mixture at a mol ratio of 30:1:2.8. Total lipid concentration was 10 mM in seed and growth

solutions. The spectrum presents two plasmon peaks at 530 and 640 nm, indicating the formation of AuNRs. It was seen from the SEM images that a large amount of AuNRs were produced. The presence of liposomes along with AuNRs was also evident in the SEM images. in Figures 4.24B and 4.24C.

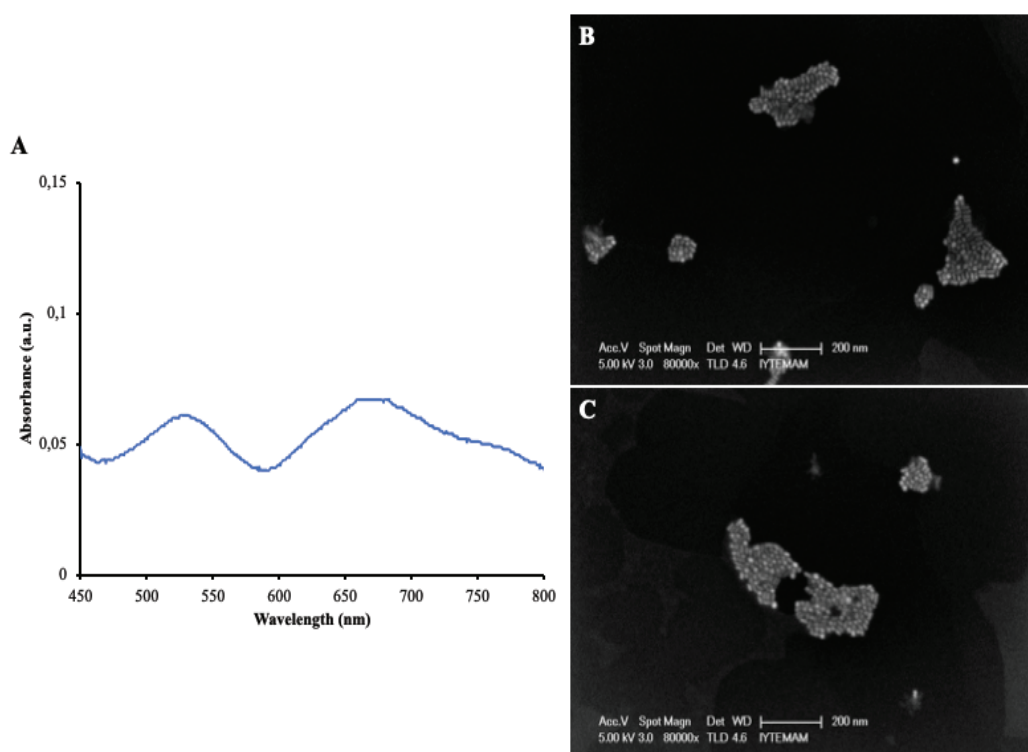


Figure 4.23. (A) UV-Vis spectrum and (B-C) SEM images of lipid-stabilized AuNRs prepared with DDAB: POPC (at a mol ratio of 27.3:1) mixture.

After the mol ratio of DDAB: POPC: DSPE-PEG mixture was increased to 40:1:2.8, the UV-Vis spectrum indicated the formation of longer AuNRs. In Figure 4.25A, lipid-stabilized AuNRs represents two peaks which are located at 530 nm and 680 nm. Thus, longer AuNRs were obtained compared to AuNRs synthesized with the same ternary lipid mixture but at a lower mol ratio (30:1:2.8). Moreover, SEM images in Figure 4.25B and 4.25C display the formation of dense AuNRs which is supported by the intensity increment in the absorbance spectrum.

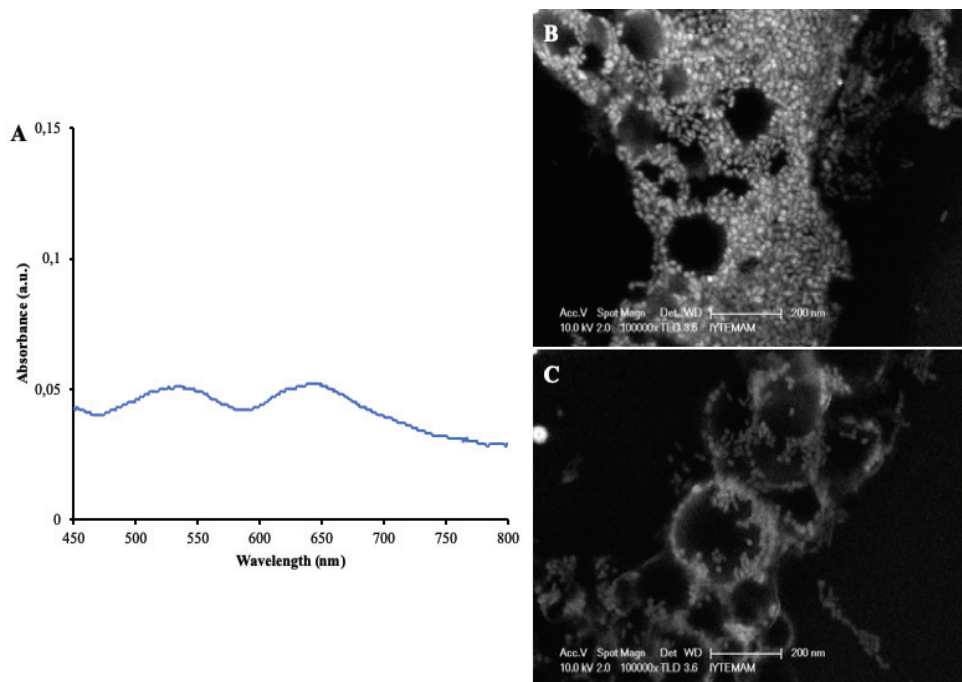


Figure 4.24. (A) UV-Vis spectrum and (B-C) SEM images of lipid-stabilized AuNRs prepared with DDAB: POPC: DSPE-PEG (at a mol ratio of 30:1:2.8) mixture.

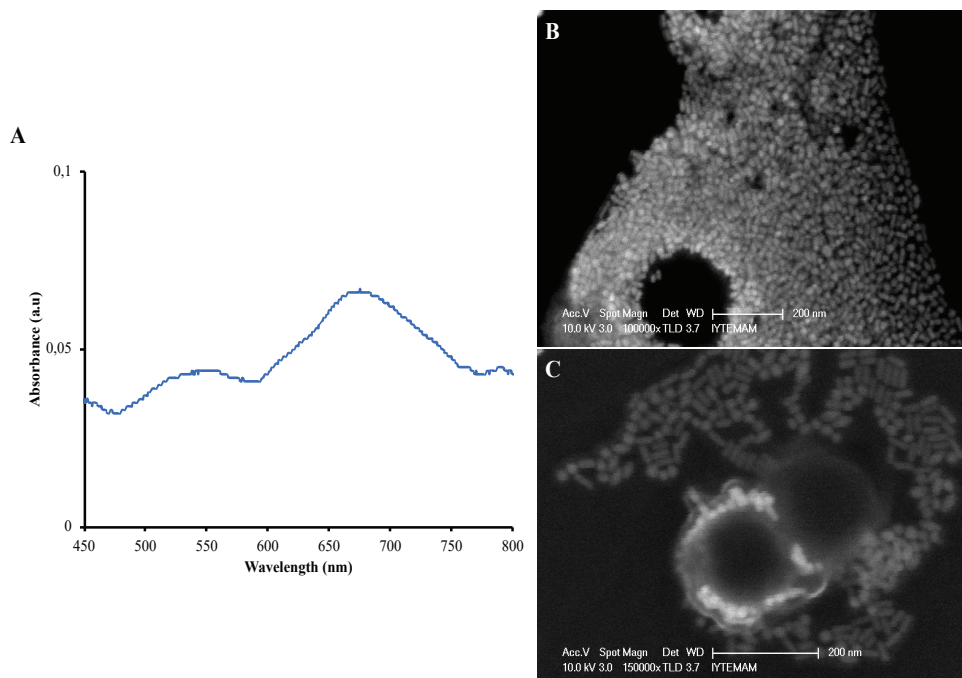


Figure 4.25. (A) UV-Vis spectrum and (B-C) SEM images of lipid-stabilized AuNRs prepared with DDAB: POPC: DSPE-PEG (at a mol ratio of 40:1:2.8) mixture.

At the final step, POPC was replaced with DPPC in experiments performed with the ternary lipid mixtures to further improve the lipid-stabilized AuNR synthesis. Hence, DDAB: DPPC: DSPE-PEG ternary mixture at a mol ratio of 30:1:2.8 was used. Figure 4.26A shows the UV-Vis spectrum of AuNRs synthesized by this lipid mixture. As a result of AuNRs production, spectrum gives two peaks at 530 nm and 680 nm. From SEM image in Figure 4.26B, the formation of AuNRs was observed.

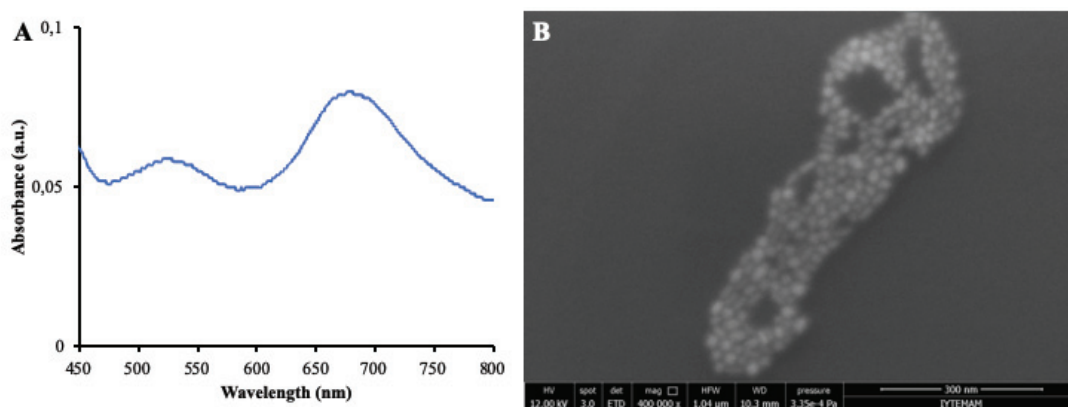


Figure 4.26. (A) UV-Vis spectrum and (B-C) SEM images of lipid-stabilized AuNRs prepared with DDAB: DPPC: DSPE-PEG (at a mol ratio of 30:1:2.8) mixture.

Overall the results showed that the best lipid-stabilized AuNRs production was obtained using DDAB: DSPE-PEG (at a mol ratio of 3:1) and DDAB: POPC: DSPE-PEG (at a mol ratio of 30:1:2.8) mixtures. As the ratio of DDAB was increased in the lipid mixture, the formation of lipid-stabilized AuNRs increased. Also, the formation efficiency of lipid-stabilized AuNRs using ternary lipid mixtures was higher among the tested lipids. In summary, lipid-stabilized AuNRs were successfully synthesized without using cationic surfactant CTAB as a stabilizer. The use of lipidic structures as stabilizing agents is anticipated to enhance the potential of AuNRs in biomedical applications.

4.2.2. Synthesis of AuNBs and Characterization

In attempts to remove DDAB completely from the formulation to minimize potential toxicity of the final gold nanostructures, lipid-stabilized nanobubble structures containing AuNRs were synthesized using a mixture of DPPC and DSPE-PEG lipids only. The formation of DPPC and DSPE-PEG based nanobubbles was analysed by UV-Vis / NIR spectroscopy, SEM, AFM and zeta potential measurements.

In the literature, the first methods for producing biocompatible metal nanomaterials include coating of particles with biocompatible polymers such as PEG (Zhao et al., 2008; Zhu et al., 2013). Apart from this method, coating nanoparticles with biocompatible lipids was an alternative method to produce biocompatible metal nanomaterials (Zhang et al., 2006). When lipids are used to coat the nanoparticle surface, it provides stabilization of nanoparticles in the medium and increases the availability of nanoparticles at the target tissue for *in vivo* studies (Matthews et al., 2015). With these effects, nanoparticles coated with biocompatible lipids display enhanced theranostic effects and decreased side effects. In the production of lipid coated nanoparticles, phospholipids and cholesterol, which are natural lipid derivatives, have generally been used (Kang and Ko, 2015).

As previously mentioned, phosphatidylethanolamine (PE) and phosphatidylcholine (PC) are two major lipid components found in all living organisms. As the hydrocarbon length in lipid structures is increased, van der Waals interactions become stronger, thus these strong intermolecular interactions bring about an increase in membrane permeability and stability due to well-ordered packing (Leekumjorn and Sum, 2006). Among the PE lipid derivatives, DSPE was chosen owing to long hydrocarbon tail (Figure 4.27). The PEG conjugated DSPE, DSPE-PEG, was utilized since the PEG chain is known to increase the stability of the liposomes, preventing the fusion and aggregation of liposomes (Zhu et al., 2018). Similarly, DPPC was selected because it has the number of hydrocarbons tail closest to DSPE. Additionally, liposomes containing PEG derivative of lipids in their composition have improved circulation time in blood. The hydrophilic PEG chains on the surface of the liposome form a hydration shell with water molecules. This hydration shell inhibits the interaction of liposome with components in the blood and also prevents clustering with other liposomes due to steric

hindrance. This prevents the recognition of liposomes by various systems in the blood and causes long-term circulation of liposomes in the blood (Abe et al., 2015).

Considering all these findings in the literature, it was attempted to produce lipid nanobubbles containing AuNRs (AuNBs). Briefly, a lipid film was formed using a mixture of 1 mM DPPC and 1 mM DSPE-PEG (50 % v/v). Then, lipid film was hydrated with PEGylated AuNRs. Subsequently, the suspension was allowed to stand at 50 °C for 1 h and sonicated under nitrogen gas. First, PEGylated AuNRs with two different aspect ratios (4.0 and 7.0) were used in these experiments. The SEM images (Figure B1 in Appendix B) of structures obtained from these experiments showed that while AuNRs with AR of 7 did not efficiently incorporate into liposomal structures, AuNRs with low AR (4.0) localized more around liposome structures. For this reason, AuNRs with slightly reduced AR (3.2) were used in order to physically facilitate the incorporation of AuNRs into the liposomal structures.

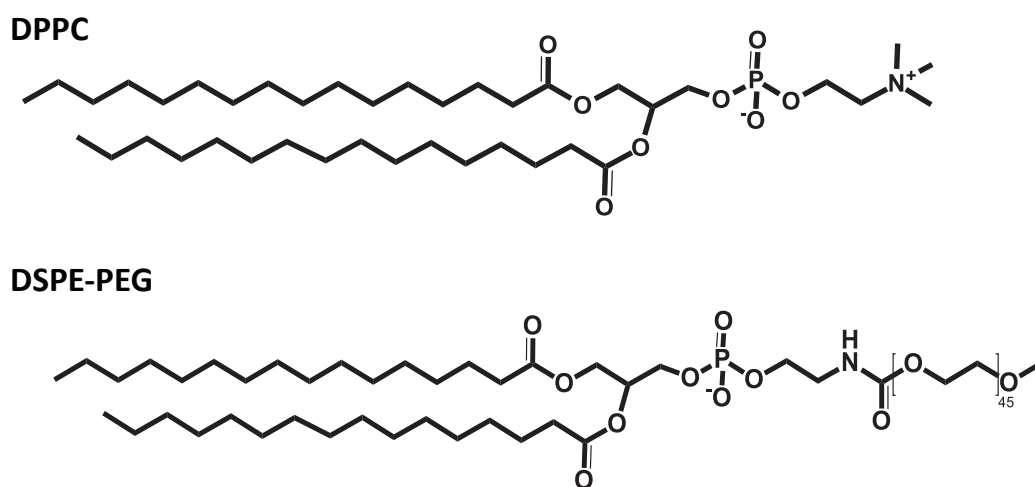


Figure 4.27. Chemical structures of DPPC and DSPE-PEG.

Typical absorbance spectra obtained in this experiment are shown in Figure 4.28. The AuNR (AR=3.2) suspension before and after PEGylation (Mn 1000 Da) showed typical UV-Vis / NIR characteristics of AuNRs, i.e., two plasmon bands corresponding to the longitudinal 710 nm and transverse 520 nm peaks before PEGylation (blue spectrum), and the longitudinal 723 nm and transverse 520 nm peaks after PEGylation

(red spectrum). The broadening of longitudinal peak after PEG modification was attributed to the use of low MW PEG (Mn 1000 Da) which provides less stability when compared with higher molecular weight PEGs (Mn 5000 Da). After PEG modification, longitudinal peak shows a significant shift of 13 nm towards the red region which was attributed to the formation of PEG layer on the surface of AuNRs. After entrapment of PEGylated AuNRs in lipid nanobubbles (green spectrum), the absorption wavelength shifted to 731 nm. This red shift of the surface plasmon band was expected because AuNRs interacted with liposomes experienced a higher refractive index (Zhu et al., 2018).

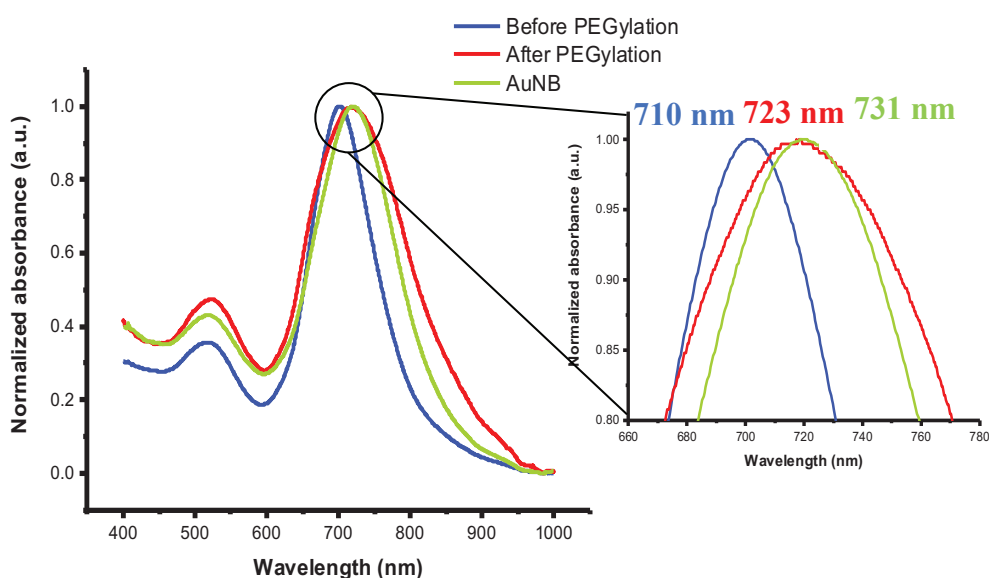


Figure 4.28. UV-Vis / NIR spectra of AuNRs (AR= 3.2) before (blue spectrum) and after PEG (Mn 1000 Da) modification (red spectrum), and AuNBs containing AuNRs (green spectrum).

Figure 4.29 represent the SEM images of AuNBs at different magnifications. These samples were studied at low voltage with high sensitivity due to the tendency of liposomes to burn during SEM measurement. In Figure 4.29A, it was observed in the large area SEM micrograph that the AuNB structures were produced intensively. According to the SEM micrographs, spherical nanobubbles having diameters between approx. 200 and 400 nm were produced.

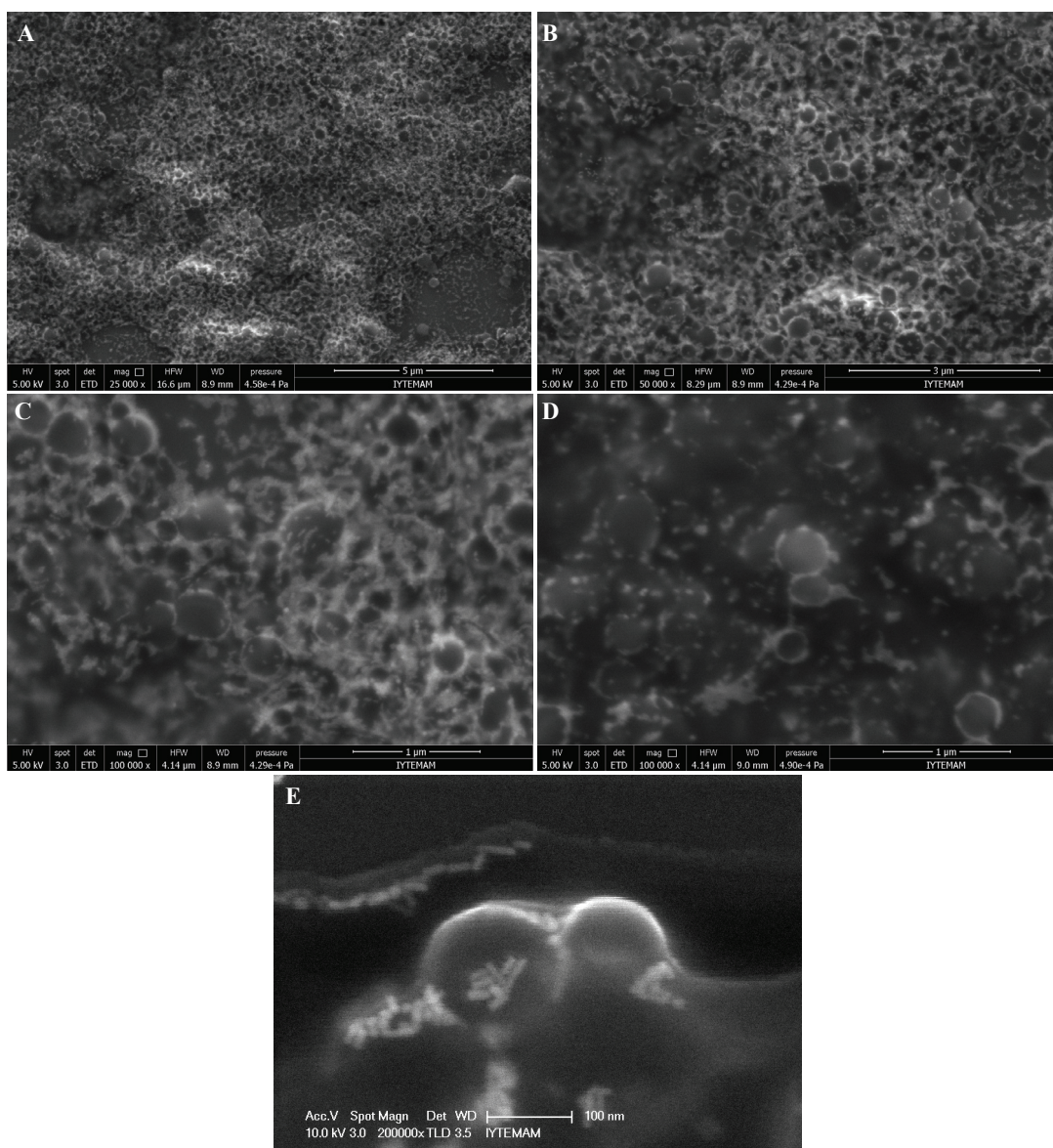


Figure 4.29. SEM images of AuNBs containing AuNRs at different magnifications.

In higher magnification micrograph (Figure 4.29C-E), the presence of multiple nanorods in a single lipid nanobubble and on its wall is clear. The attachment of AuNRs to the walls of the nanobubbles may be attributed to the interaction of PEG chains on AuNRs with lipidic structures through Van der Waals interactions and hydrogen bonding. Moreover, since PEGs are not expected to be involved in hydrophobic portions of lipidic structures, it might be difficult that PEGylated AuNRs enter into the lipid nanobubble interior. On the other hand, during the preparation of AuNBs, suspension was heated above the phase transition temperature of lipid mixture and the mixture transform into the fluid phase (Attwood et al., 2013; Avanti Polar Lipids, Inc.). The phase transition

temperature is described as the required temperature which changes the physical state of lipids from the ordered gel phase to the disordered liquid phase. The phase transition temperature values are approximately 42 °C and 74 °C for DPPC and DSPE, respectively. At the fluid phase, the hydrocarbon chains of lipids are randomly oriented. AuNRs were expected to easily fuse into the lipidic fluid phase when compared with the ordered gel phase. Also, the synthesis of AuNBs without applying nitrogen gas during the synthesis was analysed with SEM. The SEM images (Figure B2 in Appendix B) of structures obtained from these experiments showed that a small number of liposome structures were formed and PEGylated AuNRs did not efficiently interact with liposomes.

The zeta potentials measurements of AuNBs were also performed. The results are shown in Table 4.5. While the PEGylated AuNRs possessed a zeta potential of -5.4 mV AuNBs sample exhibited zeta potential of -13.7 mV. AuNBs were slightly negatively charged due to the negatively charged DSPE lipids (Figure 4.27) (Chibowski and Szczes', 2016).

Table 4.5. Zeta potential measurements of PEGylated AuNRs and AuNBs containing AuNRs (n=3).

Sample (PBS)	Zeta Potential (mV)
PEGylated AuNRs	-5.4 ± 0.9
AuNBs	-13.7 ± 0.17

4.2.3. Photothermal Effects of AuNBs

First of all, it was determined whether AuNBs displayed a photothermal effect similar to AuNRs in an aqueous medium. The temperature changes of AuNB aqueous solutions at varying concentrations were examined under 808 nm (200 mW or 500 mW) diode laser irradiation for 20 minutes (Figure 4.30).

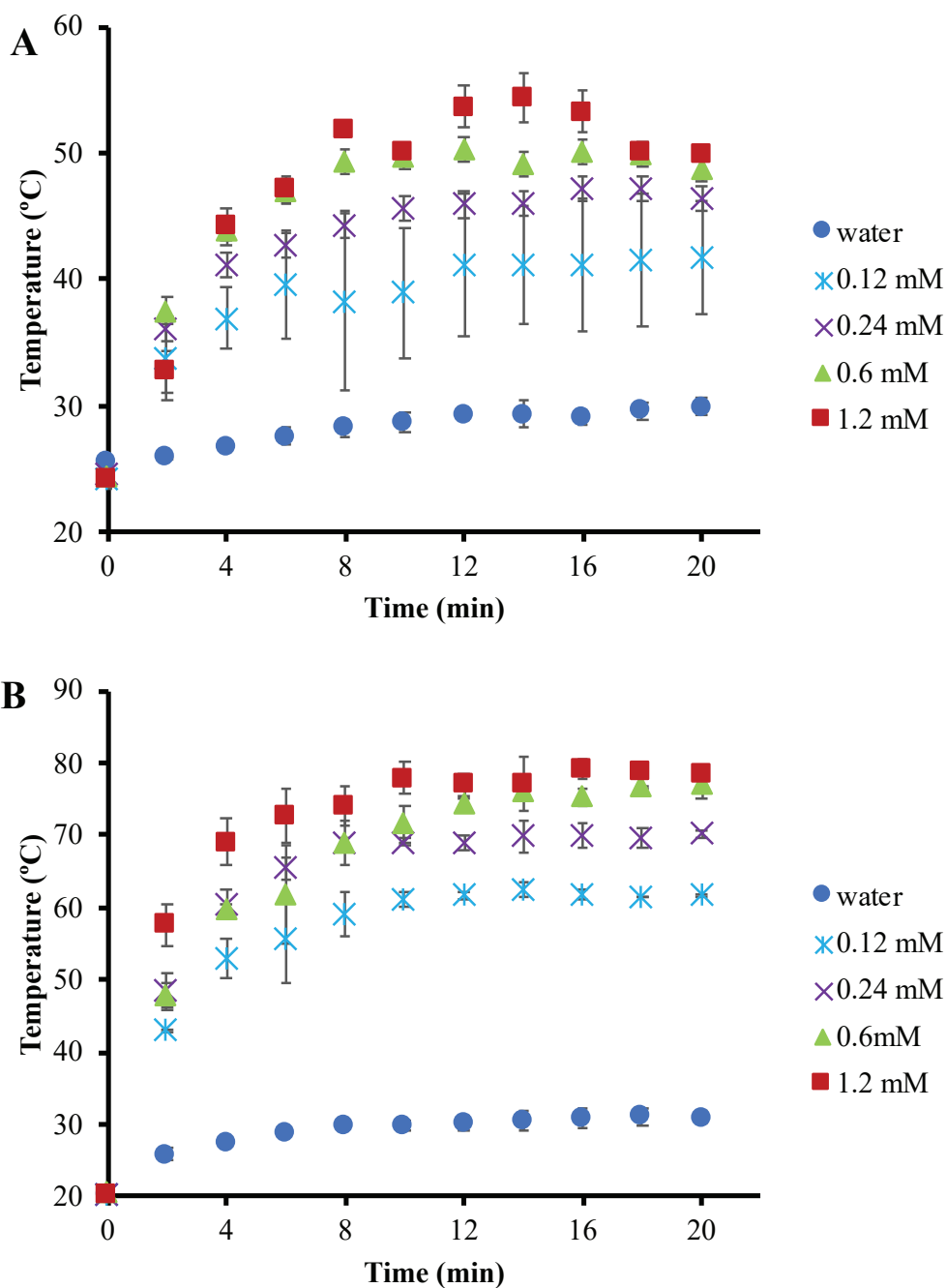


Figure 4.30. Temperature change of AuNB aqueous solutions at varying concentrations with time upon irradiation with 808 nm diode laser. (A) 200 mW and (B) 500 mW.

The temperature of this solution at 1.2 mM concentration increased to 53.6 °C under 200 mW laser irradiation (Figure 4.30A). When the laser power was increased to 500 mW (Figure 4.30B), the temperature of the AuNB solution at 1.2 mM concentration was observed to increase to 79.5 °C, indicating the efficient photothermal effect of

AuNRs present in nanobubble structures. At the lowest concentration (0.12 mM), the temperature increased to 41.8 °C with the low-power laser (200 mW), while the temperature increased to 61.9 °C with the high-power laser (500 mW). The temperature of control (water) reached only 30 °C under the same conditions. Since absorption of the light and generation of the heat increase as a result of the increasing amount of AuNRs, the rise in temperature is an expected result with the increasing concentration of AuNRs. Overall results showed that AuNBs exposed to the laser significantly increased the surrounding temperature above 50 °C which is the minimum temperature required for cell death in photothermal treatment.

Similar to the results of AuNRs (Chapter 4-Part I), when high-power laser was used, it was observed that the temperature of AuNB solutions rose more profoundly with respect to the temperature rises upon irradiation with low-power laser. For both laser powers, the temperature rise at all concentrations reached constant value between 10 and 16 minutes. Considering all these results, it was concluded that the irradiation using 808 nm laser at high power (500 mW) for 15 min yielded the strongest photothermal effect. Hence these conditions were chosen to be utilized for *in vitro* cell culture experiments. When high-power laser results of AuNRs (AR 4.0) and GNBs (with AuNRs AR=3.2) are compared, both AuNRs and AuNBs increased the solution temperature approximately to the same maximum value at all concentrations tested. However, since the surrounding lipidic structures may reduce the heat transfer. The results obtained from AuNBs can be considered to be promising.

4.2.4. *In vitro* Assessments of AuNBs

After AuNBs were successfully characterized, *in vitro* cell culture experiments were performed. First, the effect of AuNBs at varying concentrations on cell viability of breast and prostate epithelial and cancer cell lines were investigated. After determination of the 'safe dose' from cytotoxicity assays, *in vitro* cell uptake experiments were performed at the safe dose Photothermal therapy experiments were finally performed by applying laser on breast and prostate cancer cells in the range of safe doses.

4.2.4.1. Effect of AuNBs on Cell Viability

Cell viability experiments were performed to determine the IC_{50} value of AuNBs. For cell viability, AuNBs in PBS at varying concentrations (0.1---1.2 mM) were incubated with each cell type for 24 hours. While IC_{50} value of AuNBs was determined to be 1.2 mM for MCF 10A epithelial cell line, AuNBs did not display lethal effects at the tested doses for MCF7 cancer cell line (Figure 4.31). It is not surprising that the cancer cell viability is less affected by the treatment when compared with the epithelial cell line probably due to the enhanced metabolic activity. When compared with the toxicity of AuNRs (AR=4), the toxicity of AuNBs was found to be less.

Dose dependent-cytotoxicity of AuNBs was also investigated on prostate cell lines, DU 145 cancer and RWPE-1 epithelial cells (Figure 4.32). Since the growth of RWPE-1 cell line has taken a long time, dose studies could not be done in a wide range of concentrations. IC_{50} value of AuNBs was determined as 3.3 mM for DU 145 cells. For RWPE-1 cells, AuNBs show no toxicity at the tested doses.

The IC_{50} values of AuNRs and AuNBs for each cell line is presented in Table 4.6. When compared with AuNRs (AR=4.0), the newly produced AuNBs showed a less toxic effect on DU 145 cells and no toxic effect on MCF7 cells. According to the overall results of the cell viability experiments, the safe dose for AuNBs was determined as 0.5 mM.

Table 4.6. IC_{50} values of AuNBs and AuNRs (AR=4.0) for each cell line.

Sample	MCF7	MCF 10A	DU 145	RWPE-1
AuNBs	No toxicity	1.2 mM	3.3 mM	ND
AuNRs (AR=4.0)	2.2 mM	1.6 mM	1.3 mM	ND

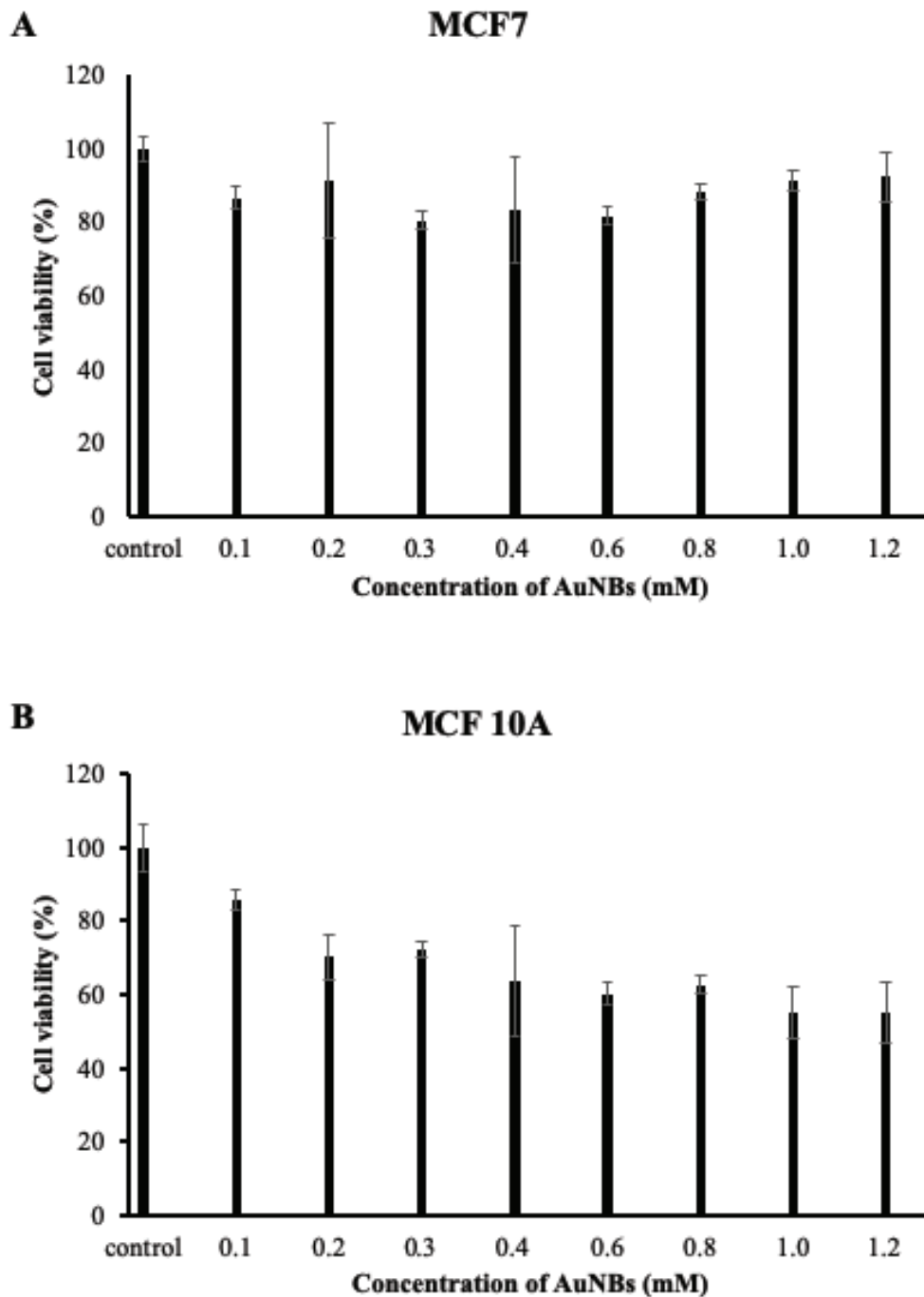


Figure 4.31. Viability of human breast (A) MCF7 cancer and (B) MCF 10A epithelial cells after 24-h incubation with varying doses of AuNBs.

AuNB structures showed direct advantage over AuNRs alone because this structure represented lower toxicity or similar toxicity depending on cell type. Additionally, AuNB structures depicted comparable temperature increase in solution after laser irradiation with respect to PEGylated AuNRs.

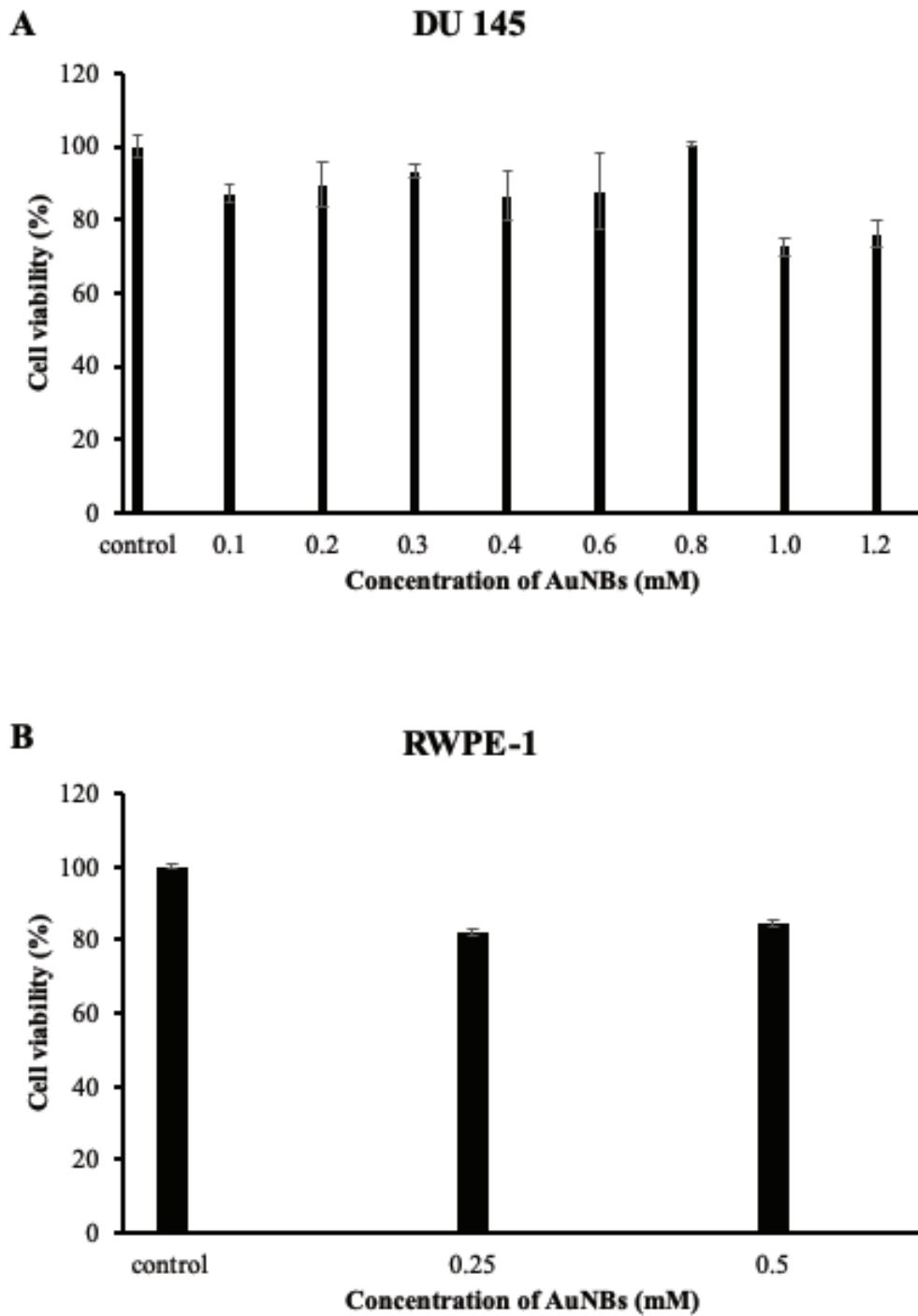


Figure 4.32. Viability of human prostate (A) DU 145 cancer and (B) RWPE-1 epithelial cells after 24-h incubation with varying doses of AuNBs.

4.2.4.2. Cell Uptake

The cell uptake profiles of AuNBs in epithelial and cancer cell lines were determined by flow cytometry. For this purpose, AuNBs were first labeled with Alexa Fluor® fluorescence dye. Breast and prostate cell lines were incubated for 1 h with fluorescent-labeled AuNBs. The concentration of AuNBs in this study was kept constant at 100 μ M which was below the IC₅₀ dose. Cells containing only 5 % (v/v) PBS were used as a control group. Experiments were performed in triplicate. The cell uptake histograms obtained from breast cell lines are given in Figure 4.33. As can be seen from the histograms, the average cellular uptake of fluorescent-labeled AuNBs was 36 ± 1 % for MCF 10A epithelial and to 76 ± 1 % for MCF7 cancer cell lines.

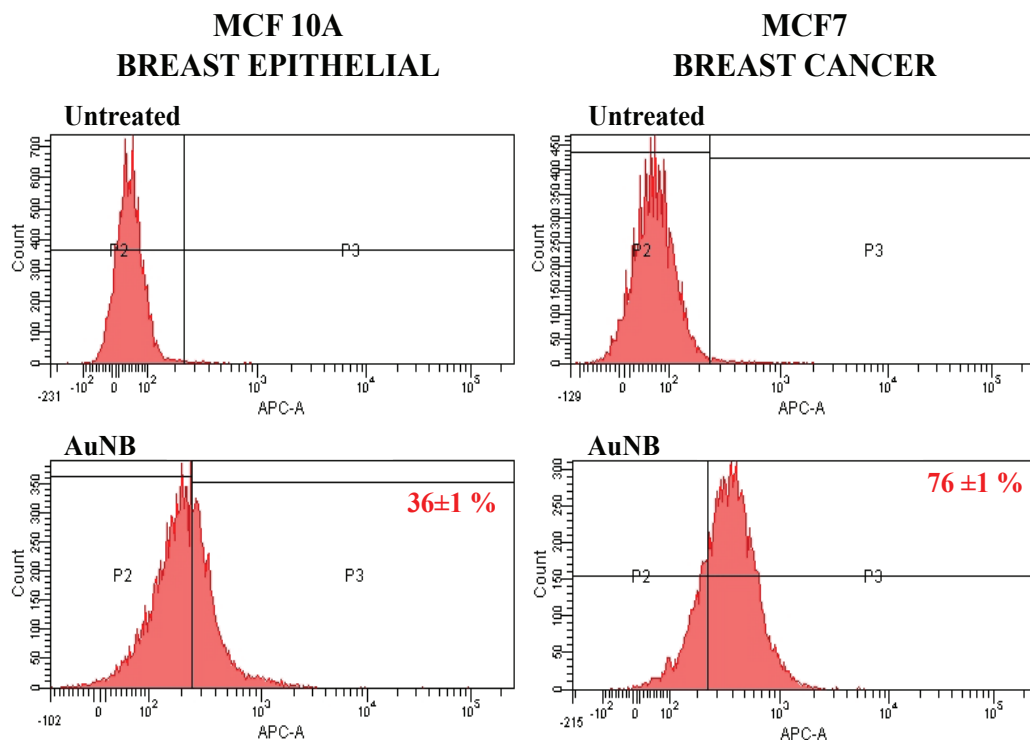


Figure 4.33. Cell uptake histogram examples of MCF 10A breast epithelial and MCF7 cancer cells after 1 h incubation with fluorescent-labeled AuNBs.

The cell uptake histograms obtained from prostate cell lines are given in Figure 4.34. From the histograms, the average cellular uptake of fluorescent-labeled AuNBs was

57 ± 10 % for RWPE-1 prostate epithelial and 90 ± 6% for DU 145 prostate cancer cell lines. While the human prostate cells take up AuNBs more when compared with human breast cells, the difference in the uptake of AuNBs between cancer and epithelial cells was significant in both breast and prostate cells. AuNBs were efficiently taken up by cancer cells more than epithelial cells because of their nature. This may have important advantages in terms of diagnosis and passive targeted therapy applications. Lipid coating on AuNRs may interact with the cell membrane to increase the uptake of gold nanoparticles. In previous studies, it has been found that lipid nanoparticles spread well in the cytosol of cancer cells without being collected or trapped by endosomes. It has been shown that gold nanoparticles embedded in liposomes can inhibit endosome-mediated uptake (Rengan et al., 2014). The cell uptake mechanisms of AuNBs need to be investigated in the future.

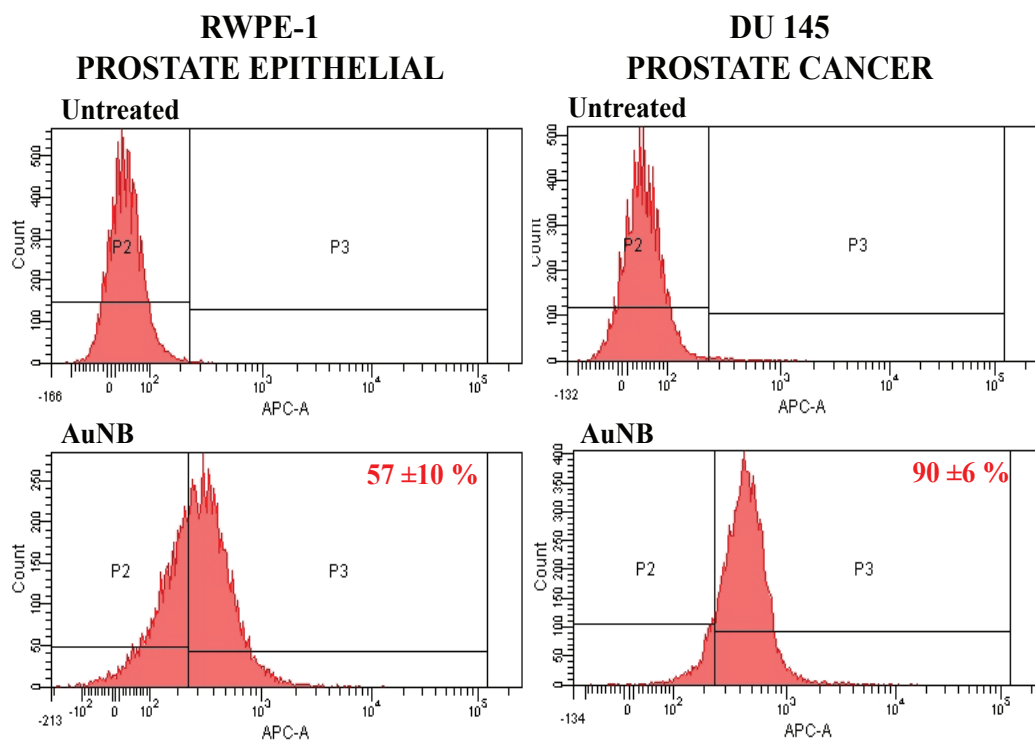


Figure 4.34. Cell uptake histogram examples of RWPE-1 prostate epithelial and DU 145 prostate cancer cells after 1 h incubation with fluorescent-labeled AuNBs.

4.2.4.3. Photothermal Ablation of Cells

In the next step, the cell viability was determined after exposing 808 nm (500 mW) laser to MCF7 breast and DU 145 prostate cancer cell lines incubated with AuNBs. Breast and prostate cancer cells were seeded into 96-well plates. After 24 h, the AuNB was added at two different doses (0.5 mM and 1.0 mM) and incubated with cells. At the end of the incubation time, cells were irradiated with 808 nm diode laser with 500 mW power for 15 mins. As control groups, only PBS and AuNB containing cells without laser irradiation were used. In addition, only PBS containing cells were exposed to laser as a control group.

The cell viability results obtained after photothermal therapy experiments are given in Figure 4.35. While the cell viability as a result of the AuNB incubation at 0.5 mM concentration did not show a statistically significant difference in cell lines compared to cells only. The cell viability after the AuNB incubation at 1.0 mM concentration demonstrated a slight decrease to 85-90 % of the cells only. The viability upon laser irradiation of cells incubated with AuNBs at 0.5 mM concentration decreased to 70 % and 60 % in MCF7 and DU 145 cells, respectively. In the case of 1.0 mM AuNBs dose, cell viability of MCF7 and DU 145 cells decreased to 45 % and 30 %, respectively, upon laser irradiation. No significant difference in viability was observed in the laser-treated control cells (control+laser) with respect to nontreated control cells (control-laser). For both cancer cell lines, as the amount of the AuNB increased, the number of destroyed cells also increased. Cancer cells are destroyed by localized hypothermia, loosening cell membranes and degrading proteins. Meanwhile, heat causes that the bio-membranes are transformed from the gel phase to the liquid phase, killing cancer cells (Luo et al., 2016). The change of liposomal membranes in the AuNB structure with heat may also provide an advantage for drug release.

Among the cell lines, the viability of DU 145 prostate cancer cells was affected more significantly compared with MCF7 breast cancer cells. Since AuNBs were taken up more by DU 145 cells, the photothermal therapy results were consistent with the cell uptake results.

AuNBs showed effective photothermal effect upon laser irradiation depending on the dose. It was observed that the cell viability at a concentration of 1 mM decreased

below 50 %. All photothermal experiments in the literature also have shown that breast cancer cells are resistant to the effects of hyperthermia (Burke et al., 2012).

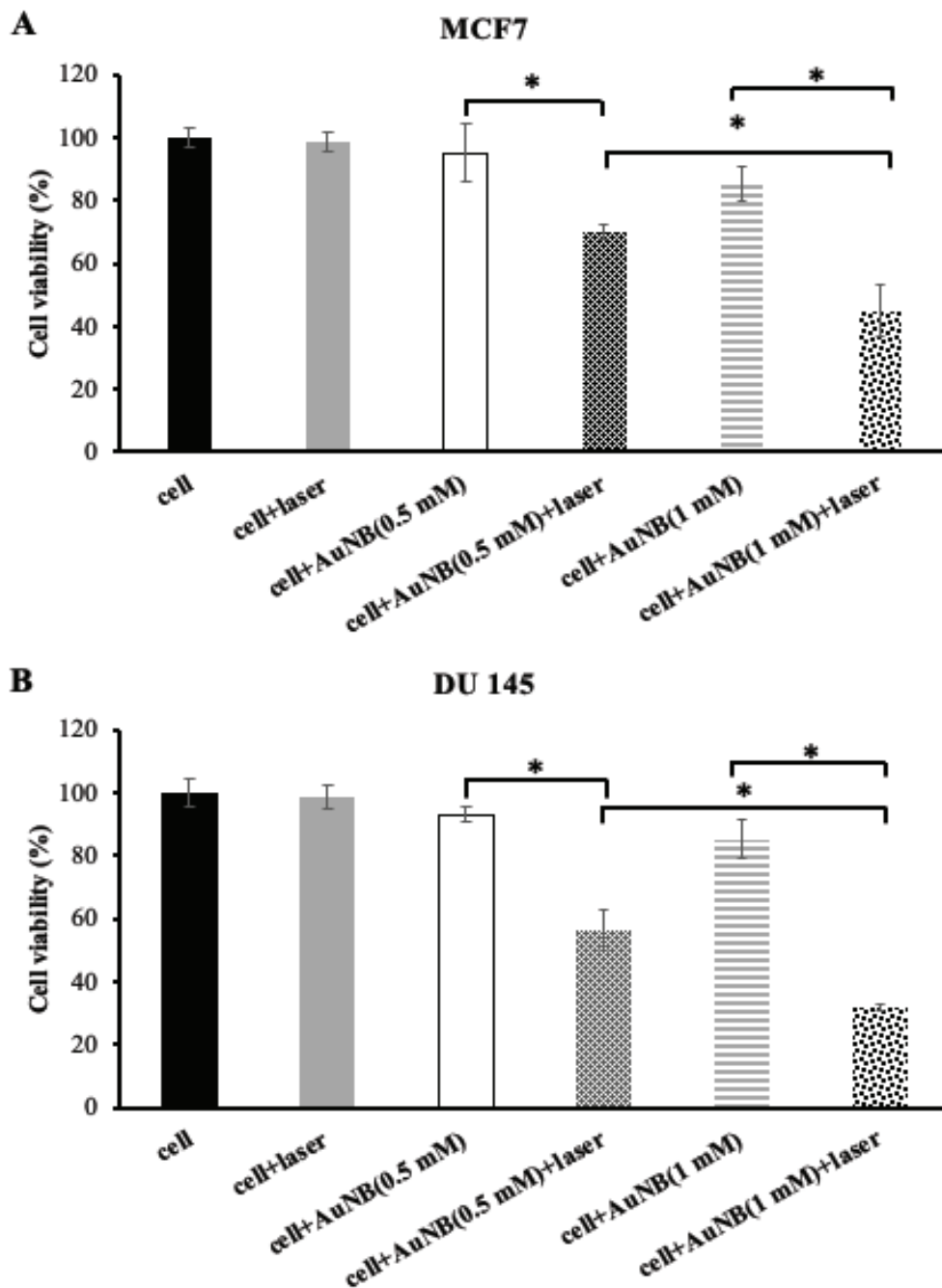


Figure 4.35. The viability of (A) MCF7 breast and (B) DU 145 prostate cancer cells incubated with AuNBs after exposure to laser light at 808 nm (500 mW) for 15 mins. Control is the cells only. Data were analyzed by t-test. (n = 3; * p < 0.05).

4.3. Part III: Cell-Specific Antibody Functionalized AuNRs

In the final part of the thesis, surface functionalization of AuNRs (AR=4.0) with antibodies (Abs) specific to cancer cells was performed for potential cell-targeting photothermal therapy applications. As presented in Part I, PEGylated AuNRs having an AR of 4.0 showed the best photothermal effect with negligible toxicity and therefore were chosen to be further functionalized with antibodies. A rabbit immunoglobulin G against a sialic acid derivative overexpressed on the plasma membrane of human breast and prostate cancer cells was used for the functionalization of PEGylated AuNRs. The conjugation of Abs to PEGylated AuNRs was performed via EDC/NHS chemistry and characterized using UV-Vis/NIR spectroscopy, XPS and zeta potential measurements, as described below. The specific cell uptake of Ab-functionalized PEGylated AuNRs was then investigated via *in vitro* experiments.

4.3.1. Antibody Conjugation to AuNRs and Characterization

Antibody (Ab) conjugation was performed after modification of AuNRs with a mixture of amine- and methoxy-terminated PEGs (methoxy: amine ratio= 4:1). Ab was conjugated to PEGylated AuNRs via EDC/Sulfo-NHS chemistry. This non-commercial, cell-specific Ab, which is a rabbit immunoglobulin G, is against a sialic acid derivative expressed on the plasma membrane of mammalian cells at very low levels. However, it is thought to be overexpressed on certain mammalian cancer cells including ovarian, breast and prostate cancer cells. To the best of author's knowledge, gold nanorods targeted with this non-commercial antibody has not yet been investigated in the literature.

The amine end-group of PEGs on the AuNR surface was reacted with carboxylic acid groups of Ab's acidic amino acids using EDC and NHS. The reaction of the carboxylic acid groups with EDC results in an unstable acylisourea intermediate and followed by the reaction using NHS forming amine-reactive succinimide ester. This reacts with the amino groups on the PEGylated AuNRs to form a stable amide bond (Centi et al., 2014).

Antibody conjugation of AuNRs was confirmed via UV-Vis / NIR spectrometry, zeta potential and XPS measurements. Conjugation was first recorded by UV-Vis / NIR spectroscopy (Figure 4.36). The longitudinal band of PEGylated AuNRs was measured at 769 nm (blue spectrum). After conjugation with Ab, the peak shifted to 774 nm (red spectrum). This 5 nm red shift was indicative of the surface functionalization. This shift was expected due to the antibody conjugation and is consistent with the literature (Joshi et al., 2013). As mentioned in the previous part, molecular binding on AuNRs surface causes a change in the refractive index of an environment, thus, a wavelength peak shift in the spectrum was detected (Truong et al., 2012). After conjugation of Ab to AuNRs, the longitudinal peak intensity showed a slight decrease probably due to the removal of some AuNRs during the purification procedure by centrifugation.

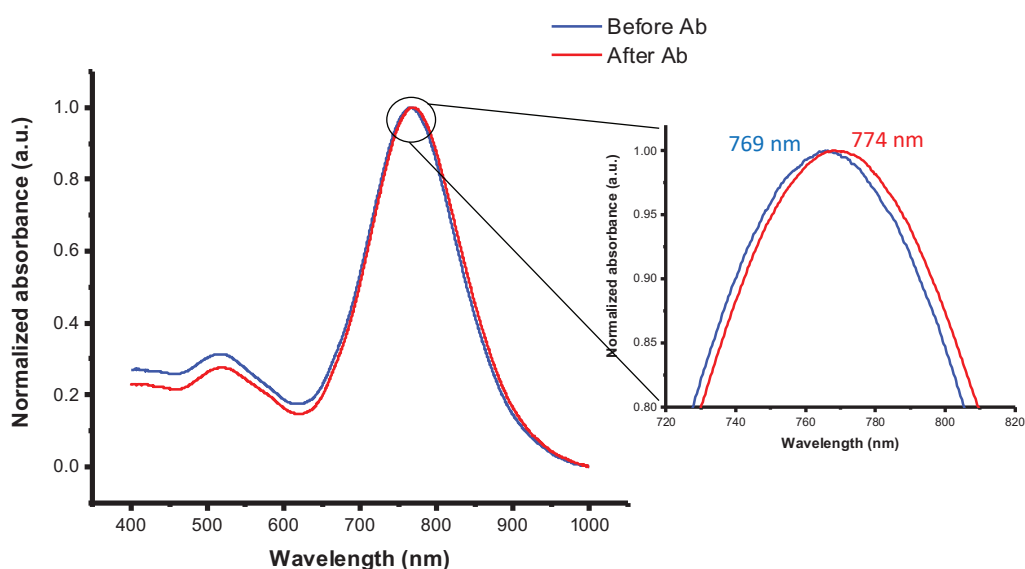


Figure 4.36. UV-Vis /NIR spectra of PEGylated AuNRs, before (blue spectrum) and after Ab conjugation (red spectrum).

Zeta potential of AuNRs was measured before and after PEGylation, and after Ab conjugation. Table 4.7 depicts the results after each surface functionalization step. After the modification of AuNRs with PEG, the zeta potentials of AuNRs in water decreased from 20.4 mV to -3.6 mV. The reduction in zeta-potential was attributed to the removal of cationic CTAB molecules and the successful binding of PEG molecules to AuNRs

surface. After PEGylation, PEG-modified AuNRs showed a nearly neutral surface due to PEG structure (Liopo et al., 2012; Ba et al., 2010). Although the amine groups are expected to be positively charged at low pH values, the almost neutral zeta potential of PEGylated AuNRs was attributed to the embedment of amine end-groups in the polymer chains on the surface (Kumar et al. 2014).

Table 4.7. Zeta potential measurements of AuNRs, PEGylated AuNRs and Ab-conjugated AuNRs (n=3).

Sample	Zeta Potential in water (mV)	Zeta Potential in PBS (mV)	Zeta Potential in PBS / 10% FBS (mV)
AuNRs	20.4 ± 2.3	10.6 ± 1.6	-8.5 ± 1.0
PEGylated AuNRs	-3.6 ± 0.9	-5.7 ± 2.0	-6.8 ± 0.5
Ab-conjugated AuNRs	-1.6 ± 0.7	-1.9 ± 0.4	-7.4 ± 0.8

Antibodies are known to bear a net positive charge at neutral pH (Boswell et al., 2010). Theoretically, the zeta potential of PEGylated AuNRs is expected to increase with antibody conjugation since the net charge of the antibodies is positive. However, the net charge of this antibody was negative (-5.2 ± 0.6 mV). As a result of Ab conjugation, the zeta potential of PEGylated AuNRs was measured to increase from -3.6 mV to -1.6 mV (increase in positive charge), which indicated the conjugation of the antibodies. In order to mimic the physiological conditions, zeta measurements were also taken in PBS and serum-containing PBS media. Compared the zeta potential results in water and PBS, the zeta potentials of PEGylated AuNRs and antibody-conjugated AuNRs (Ab-AuNRs) were nearly at the same value, but the decrease in charge of AuNRs was observed due to possible adsorption of positively charged AuNRs and phosphate anions in PBS through electrostatic interactions.

When PBS contained 10 % serum, the zeta potential of AuNRs decreased due to possible adsorption of serum proteins (most abundantly albumin). After PEGylation of AuNRs, the zeta potential slightly increased indicating less interactions with serum

proteins, which was attributed to the non-fouling character of PEG. After Ab conjugation, the zeta potential increased slightly, possibly due to the electrostatic interactions of positively charged Ab's on the surface with serum proteins. Since PEG layers provide a protein-repellent feature on the surface of PEGylated AuNRs, the zeta potential slightly increased as expected showing the binding of amine-terminated PEGs. PEGylation of AuNRs inhibits the aggregation as well as adsorption of serum proteins on its surface. As a conclusion, positively charged groups on the surface of CTAB-stabilized AuNRs and Ab-AuNRs facilitated the non-specific adsorption of negatively charged serum proteins (Alkilany et al., 2009). Study supported that positively charged AuNRs absorbed serum proteins (Liu et al., 2016).

Additionally, the conjugation of antibody to PEGylated AuNRs was also confirmed via XPS measurements. XPS spectra showing the C1s and N1s regions of PEGylated AuNRs and Ab-AuNRs were shown in Figure 4.37. In C1s spectrum, before Ab conjugation, the major carbon peak at 283 eV was assigned to the C-C bonds and at 284 eV was assigned to C-O bonds in PEG molecules. After Ab conjugation, in addition to these peaks, the carbon peak was assigned to the C=O bonds within the antibody molecules. In N1s spectrum, before Ab conjugation, the nitrogen peak at 400 eV corresponded to the amine groups within the PEG molecules, and after Ab conjugation, in addition to this peak, the peak at 402 eV corresponded to the amine groups in aromatic structures within the antibody molecules.

From XPS experiments, the elemental composition was also determined by normalizing all measured values to Au quantity. The atomic percentages of the elements within the tested samples are summarized in Table 4.8. After PEG modification of AuNRs, the S atoms of PEG molecules that anchored to the gold surface were also observed. Besides, the low atomic percentage of Br indicates the replacement of CTAB molecules with PEG molecules on the surface of AuNRs. The low atomic percentage of nitrogen was attributed to the embedding of the functional end-group of PEG molecules in the macromolecular chain (5000 g/mol). While nitrogen and sulfur atoms were observed at a low percentage in PEGylated AuNRs, their percentages profoundly increased after antibody conjugation. This result was expected since antibodies are protein structures containing amine and sulfur residues. A high quantity of oxygen and carbon atoms in the composition of antibodies led to an increase in the number of their atomic percentages after antibody conjugation.

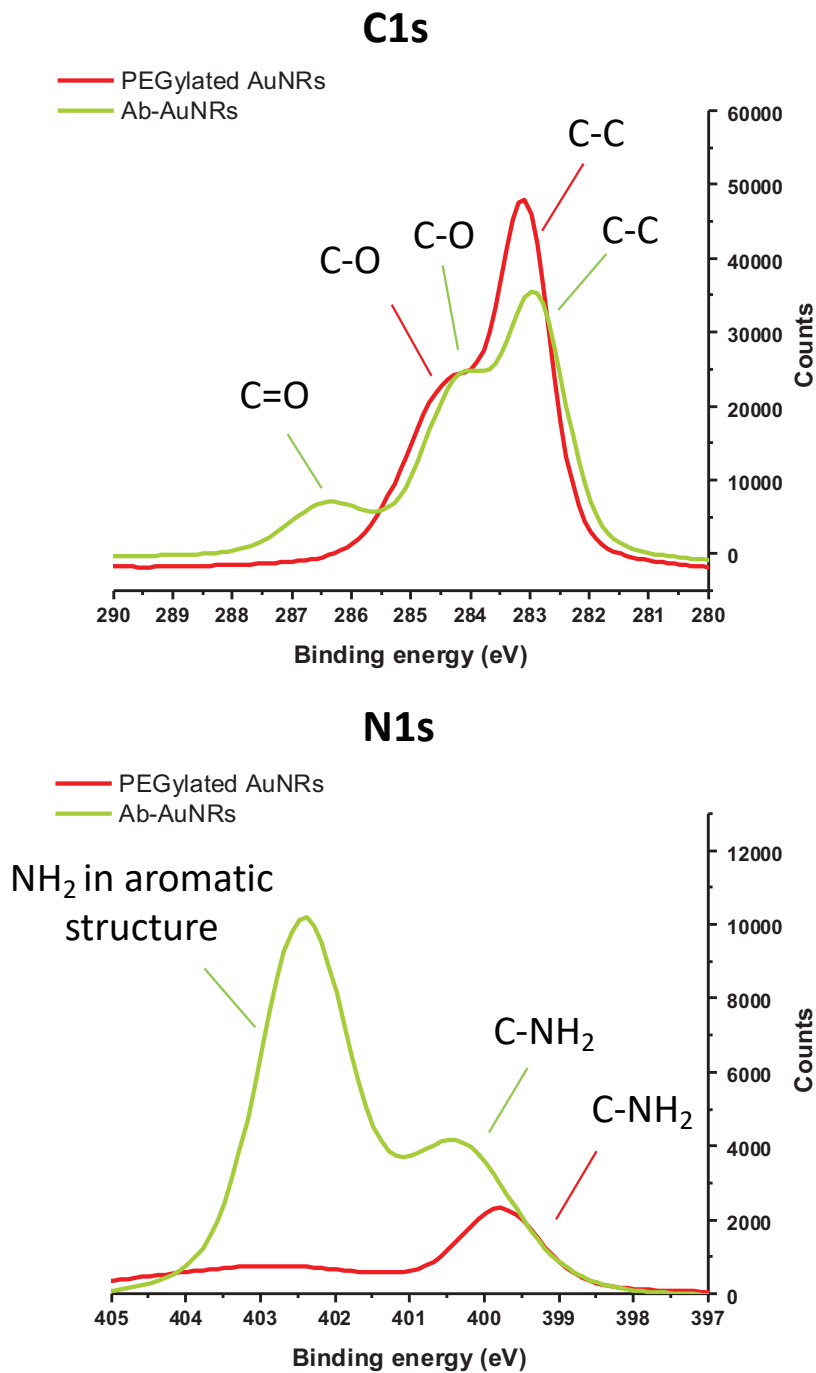


Figure 4.37. XPS spectra showing the C1s and N1s regions of PEGylated AuNRs and Ab-AuNRs.

Overall UV-Vis / NIR spectroscopy, zeta-potentials and XPS results confirmed the binding of antibody molecules onto PEGylated AuNRs surfaces.

Table 4.8. Elemental composition and atomic percentages of PEGylated AuNRs and Ab-AuNRs obtained by XPS.

Element	PEGylated AuNRs	Ab-AuNRs
C1s	26.9	33.6
O1s	4.9	11.0
N1s	0.1	5.1
S2p	0.1	1.2
Br3d	0.2	-

4.3.2. *In vitro* Assessments of Ab-AuNRs

First, the effect of Ab conjugation to AuNRs on the viability of breast and prostate cells was investigated at varying concentrations. Next, *in vitro* cell uptake experiments were performed to determine the targeting ability of Ab-conjugated AuNRs.

4.3.2.1. Effect of Ab-AuNRs on Cell Viability

The safe dose of PEGylated AuNRs was found to be 0.7 mM as shown in Part I. The cell viability of Ab-conjugated AuNRs was tested below the safe dose of PEGylated AuNRs and compared with that of PEGylated AuNRs. For cytotoxicity assays, breast and prostate cell lines were incubated with the AuNR samples prepared in PBS at two different gold concentrations (0.25 and 0.5 mM). After 24 h incubation, the viability of cells was determined via MTT assay (Figure 4.38). As can be seen, antibody conjugation to AuNRs did not cause any effect on the viability of MCF7 breast and DU 145 prostate cancer cells at the tested doses. But the viability of MCF 10A breast and RWPE-1 prostate epithelial cells was found to be affected by the presence of antibodies on the gold surface. However, there were no lethal effects at the tested doses.

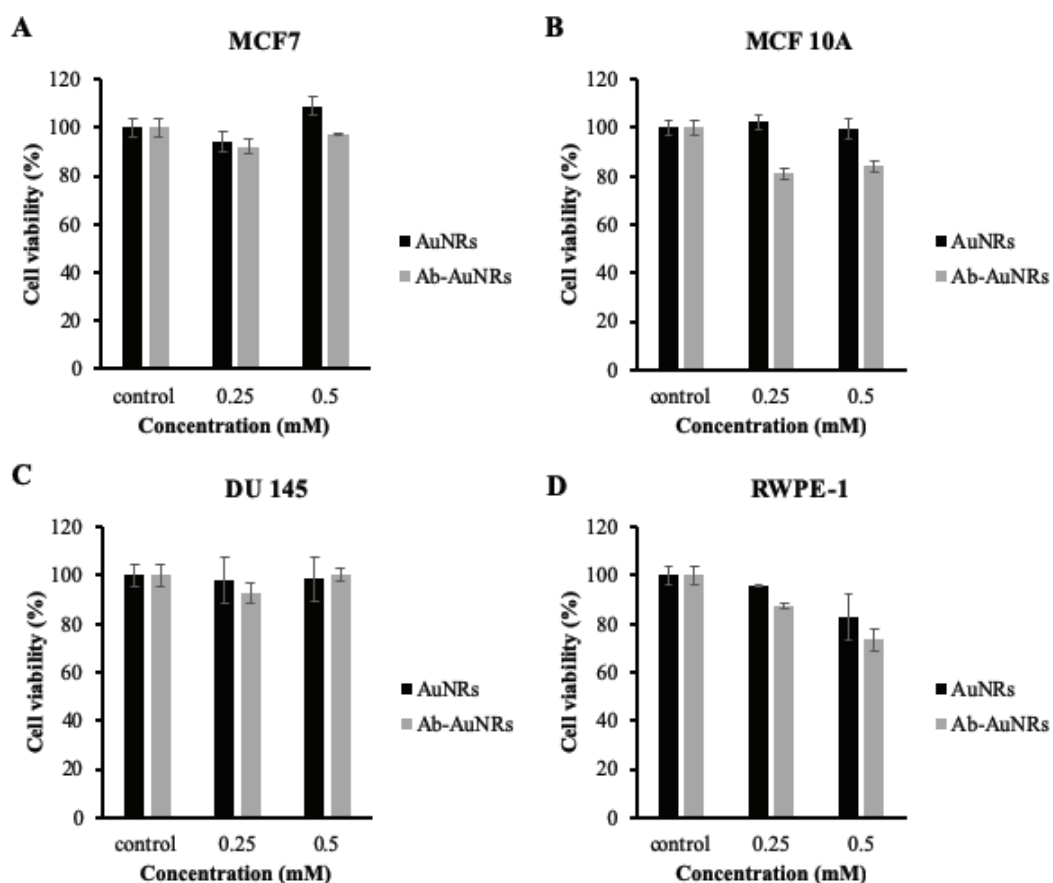


Figure 4.38. Viability results of (A) MCF7, (B) MCF 10A, (C) DU 145 and (D) RWPE-1 after 24 h incubation with PEGylated and Ab-conjugated AuNRs.

4.3.2.2. Cell Uptake

The cell uptake of antibody-conjugated AuNRs was investigated via flow cytometry. For this purpose, the antibody was first labeled with Alexa Fluor and then conjugated to AuNRs (AR=4.0). Separately, PEGylated AuNRs were labeled by conjugating Alexa Fluor to PEG amine end-groups. The fluorescence labeling degree of PEGylated AuNRs was normalized according to the labeling degree of Ab-conjugated AuNRs. Both breast and prostate epithelial and cancer cells were incubated with fluorescent-labeled AuNRs with or without Ab conjugation for 1 h. The concentration of AuNRs in this study was kept constant at 0.1 mM which was below the IC_{50} dose. The cell uptake histograms obtained from the experiments are given in Appendix C.

Firstly, the uptake of fluorescent-labeled PEGylated AuNRs and fluorescent-labeled Ab conjugated AuNRs by breast epithelial MCF 10A and breast cancer MCF7

cells was investigated. Figure 4.39 shows that the uptake of fluorescent-labeled AuNRs by breast cancer cells after 1 h of incubation was almost the same with the uptake by breast epithelial cells. When compared with PEGylated AuNRs, Ab-conjugated AuNRs were taken up more by both cell types. However, there was no significant difference between the uptake of Ab-conjugated AuNRs by cancer and epithelial cells. While the cell uptake percentage of fluorescent-labeled Ab-conjugated AuNRs in MCF 10A was $76 \pm 7 \%$, the cell uptake of fluorescent-labeled Ab-conjugated AuNRs was $85 \pm 1 \%$ in MCF7 at the end of 1 h. This might be due to the fact that both epithelial and cancer cell lines express the same level of sialic acid derivative targeted by the antibody used in this study. This needs to be investigated in future research. Overall, the result showed that Ab-conjugated AuNRs did not show targeting capability for breast cells.

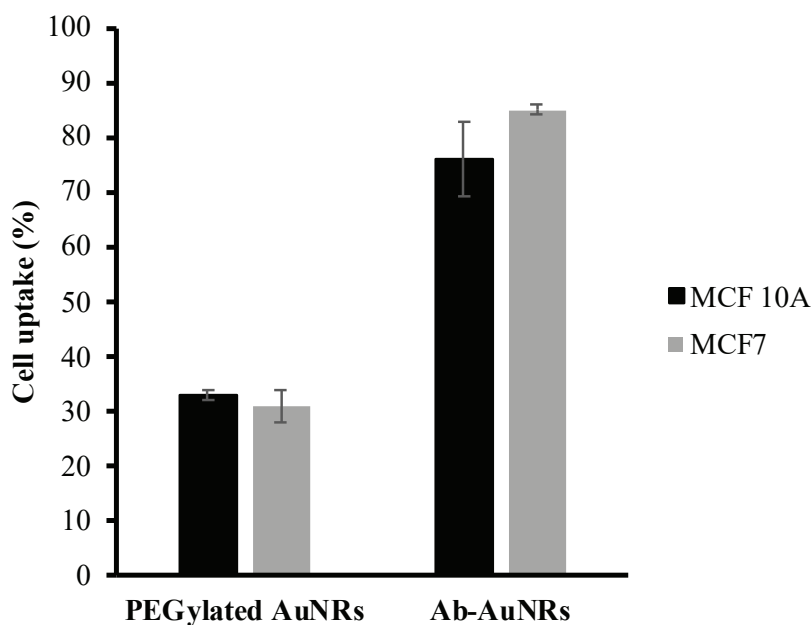


Figure 4.39. Uptake of fluorescent-labeled PEGylated AuNRs and fluorescent-labeled Ab conjugated AuNRs by MCF 10A breast epithelial and MCF7 breast cancer cells determined by flow cytometry.

The uptake of fluorescent-labeled PEGylated AuNRs and fluorescent-labeled Ab conjugated PEGylated AuNRs by prostate epithelial RWPE-1 and prostate cancer DU 145 cells was investigated. As can be seen in Figure 4.40, the uptake of PEGylated AuNRs by prostate cancer cells was almost the same with the uptake by prostate epithelial

cells. Interestingly, while the uptake of Ab-conjugated AuNRs by RWPE-1 epithelial cells was 27 ± 1 %, the uptake by DU 145 cancer cells was 74 ± 2 %. The uptake of Ab-conjugated AuNRs by DU 145 cancer cells was significantly higher when compared with RWPE-1 epithelial cells, which evidenced the cell-specific targeting ability of Ab-conjugated AuNRs. It is also well-known that certain receptors in cancer cells are overexpressed compared to healthy cells (Centi et al., 2014).

Nanoparticle delivery strategies may use passive and/or active targeting mechanisms. In passive targeting mechanism, non-targeted nanoparticles are accumulated and retained in the tumor with the enhanced permeability and retention (EPR) effect of tumors. Active targeting mechanism occurs using specific ligands (i.e. antibodies, peptides, or small molecules) which recognize specific surface receptors on certain cells. After binding the tumor cells, nanoparticles are uptaken by receptor-mediated endocytosis and internalized (Huang et al., 2010; Wang et al., 2015). Overall, it is known that the cellular uptake of nanoparticles generally depends on the size, shape and surface properties of the nanoparticles (Salatin and Khosroushahi, 2017).

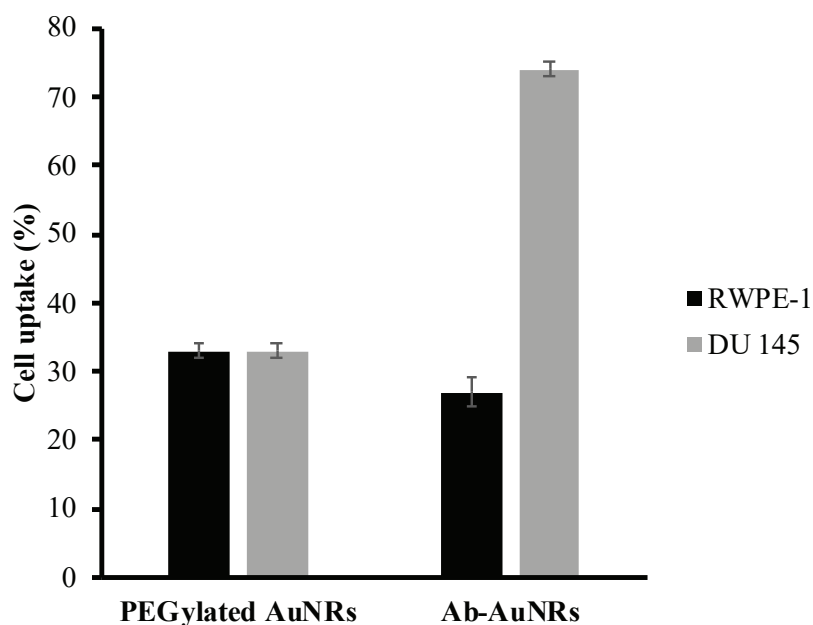


Figure 4.40. Uptake of fluorescent-labeled PEGylated AuNRs and fluorescent-labeled Ab conjugated AuNRs by RWPE-1 prostate epithelial and DU 145 prostate cells determined by flow cytometry.

Among cancer and epithelial cell lines, breast and prostate cancer cells take more fluorescent-labeled Ab-AuNRs. The uptake or binding of antibody-conjugated nanoparticles is thought to be dependent on the level of receptor expression and ligand-receptor binding affinity of the cells as well as other factors such as steric inhibition and receptor-mediated endocytosis (Huang et al., 2010). The difference in uptake or binding of Ab-AuNRs in prostate and breast cells may be due to the difference in the amount of receptor expression on the cell membrane. Considering that prostate cancer cells took up more Ab-AuNRs than breast cancer cells, it can be said that Ab-specific receptors are overexpressed on prostate cancer cell surfaces. However, further experiments need to be performed to confirm this statement. As a result, the cell-specific antibody-conjugated AuNRs have the capability of selective targeting prostate cancer cells.

CHAPTER 5

CONCLUSION

The aim of this thesis is to synthesize gold nanorods (AuNRs) and lipid-stabilized nanobubbles containing AuNRs and investigate the potential of these plasmonic nanostructures as photothermal therapy agents for breast and prostate cancer through *in vitro* cell culture experiments.

Firstly, AuNRs with varying aspect ratios (AR= 2.7, 3.2, 4.0 and 7.0) were successfully synthesized by varying the concentration of co-surfactant and AgNO₃ in the growth solution used in the AuNR synthesis. The characterization of synthesized AuNRs was carried out by UV-Vis/NIR spectroscopy, SEM, AFM, ICP-MS, ELS and XPS. These investigations showed that AuNRs with a width of approximately 12 nm and a length varying between 30 nm and 100 nm were synthesized at high yield. The increase in the length of AuNRs associated with the shift of longitudinal absorption peaks in the UV-Vis/NIR spectra towards the red region.

After producing AuNRs with varying ARs, the surface of AuNRs was modified with PEG to make to eliminate the well-known toxicity of CTAB surfactant used to stabilize AuNRs while maintaining their colloidal stability. After PEGylation, it was observed that the longitudinal peak shifted to the red region in all of AuNRs samples with different aspect ratios (Niidome *et al.*, 2009), indicating PEGylation of the surface. Additionally, the absence of broadening in the longitudinal peak after PEGylation indicated that PEG-functionalized AuNRs were well-dispersed in water. (Oyelere *et al.*, 2007). Furthermore, AFM images before and after modification of AuNRs with PEG clearly demonstrated the PEG layers around AuNRs visually.

ELS measurements of AuNRs before modification with PEG showed a positive zeta potential value. Since CTAB is a cationic molecule, CTAB stabilized AuNRs showed cationic surface properties. After modification with PEG, the zeta potential shifted from positive to slightly negative values, indicating that CTAB molecules were replaced by PEG molecules on AuNRs surface (Liopo *et al.*, 2012; Zhang *et al.*, 2014).

XPS analysis showed the presence of S atoms on the AuNR surface after PEG modification. It also indicated the decrease in the Br atomic percentage suggesting the

replacement of CTAB molecules with PEG molecules on the surface of AuNRs. As a result; all of UV-Vis/NIR spectra, zeta potential and XPS results proved that CTAB on the surface of AuNRs was successfully replaced with PEG.

PEGylated AuNRs displayed photothermal effect in a concentration, AR, laser wavelength and power-dependent manner. Under laser irradiation at 808 nm with 500 mW power, PEGylated AuNRs with two different ARs (4 and 7) at all concentrations tested (0.12, 0.24, 0.6 and 1.2 mM) increased the solution temperature above 50 °C, which is the minimum temperature required for effective photothermal therapy. The temperature increases caused by AuNRs with AR of 7.0 remained relatively low. It was determined that the use of AuNRs with lower aspect ratio at high power laser (500 mW, 808 nm) and irradiation duration of 15 mins was suitable for *in vitro* photothermal therapy experiments.

For *in vitro* experiment, first, the effects of AuNRs on cell viability and their safe doses were determined via MTT assay. PEGylated AuNRs showed dose and cell type-dependent cytotoxicity. When AuNRs with different aspect ratios were compared, it was found that AuNRs with AR of 4.0 were the least toxic and the toxicity increased with increasing the AR of AuNRs. AuNRs with high AR (7.0) showed almost 2 times higher toxicity compared to AuNRs with low AR (4.0). Based on the cytotoxicity results, a safe dose of AuNRs with AR of 4.0 and AR of 7.0 was determined to be 0.7 and 0.3 mM, respectively.

It was proven by ICP-MS measurements that AuNRs having AR of 4.0 and 7.0 were both effectively taken by breast cancer MCF7 and prostate cancer DU 145 cells. The cell uptake of AuNRs with AR of 7.0 is much faster than that of AuNRs with AR of 4.0. This finding supports the literature indicating that nanomaterials with high aspect ratio have higher interaction with biological membranes (Lee et al., 2014; Fubini et al., 2011). In addition, cell uptake results supported cell viability results. As expected, AuNRs with a higher aspect ratio showed more toxic effect because of higher cell uptake.

The photothermal effect caused by AuNRs on *in vitro* cell cultures was identified by MTT cell viability test. At 0.2 mM concentration, AuNRs (AR= 4.0) caused a statistically significant slight decrease in cell viability upon NIR laser irradiation. When AuNRs dose was increased to 0.5 mM, AuNRs (AR= 4.0) effectively killed cancer cells upon NIR laser irradiation. In contrast, AuNRs with higher AR caused no statistically significant decrease in cell viability upon NIR laser irradiation. When all results were evaluated, it was concluded that AuNRs having an AR of 4.0 were superior than AuNRs

having an AR of 7.0 in terms of toxicity and photothermal effect. Therefore, it was decided to examine only AuNRs having an AR of 4.0 for modification with a selective antibody against a sialic acid derivative receptors of human cancer cells.

In the final part of the thesis, surface functionalization of AuNRs (AR=4.0) with a non-commercial antibody (Ab) specific to breast and prostate cancer cells was performed for potential cell-targeting photothermal therapy applications. Cell-specific antibody conjugation to AuNRs was verified by UV-Vis/NIR spectroscopy, ELS and XPS measurements.

Antibody conjugation to AuNRs did not cause any toxic effect on the cells at the tested doses.

The cell uptake of antibody-conjugated AuNRs was investigated to determine the targeting ability of Ab-conjugated AuNRs. While the uptake of fluorescent-labeled Ab-conjugated AuNRs by MCF 10A cells was 76 %, the uptake of the same AuNRs by MCF 7 cells was 85 %. From this result, it was concluded that Ab-conjugated AuNRs did not show sufficient improvement in targeting breast cancer cells, which needs to be investigated in the future. The uptake of fluorescent-labeled AuNRs by prostate cancer DU 145 cells was 74 %, while the cell uptake of the same AuNRs by prostate epithelial RWPE-1 cells was 27 %. The uptake of Ab-conjugated AuNRs by DU 145 cancer cells was significantly higher when compared with RWPE-1 epithelial cells.

Considering that prostate cancer cells received more Ab-AuNRs than breast cancer cells, it can be said that more receptors are overexpressed on prostate cancer cell surfaces. However, further experiments need to be performed to confirm this statement. As a result, the cell-specific antibody-conjugated AuNRs showed the capability of selective targeting prostate cancer cells.

In the second part of the thesis, lipid-stabilized AuNRs were obtained for the first time in the literature using binary (DDAB: DSPE-PEG) or ternary (DDAB: POPC: DSPE-PEG; DDAB: DPPC: DSPE-PEG) lipid mixtures.

Also, lipid-stabilized nanobubbles containing more than one AuNRs (AuNBs) were successfully synthesized in the size range between 200 and 400 nm using a mixture of DPPC and DSPE-PEG lipids which are biocompatible / non-toxic phosphatidylcholine derived lipids, as characterized by UV-Vis-NIR spectroscopy, SEM, AFM, ICP-MS and ELS, and AFM images proved that nanobubbles were produced with multiple AuNRs located inside or on the wall of lipid nanobubbles.

Importantly, it was observed that AuNBs significantly increased the temperature of the aqueous solutions in a concentration-dependent manner. Compared to AuNRs (AR=4.0), AuNBs increased the solution temperature to the same maximum temperature under laser irradiation at 808 nm with 500 mW power.

AuNBs did not show a significant toxic effect even at high concentrations such as 0.12 mM in cancer and epithelial cell lines used in the study. AuNBs showed a direct advantage over AuNRs because this structure presented significantly lower or at least similar toxicity depending on cancer cell type. Based on the cytotoxicity results, the safe dose of AuNBs was determined to be 0.5 mM.

AuNBs were efficiently taken up by both prostate and breast cancer cells. The uptake by prostate and breast epithelial cells was relatively less.

AuNBs showed a less photothermal effect on cell viability when compared with AuNRs (4.0). The cell viability upon treatment with at 1.0 mM AuNBs under laser irradiation on MCF7 and DU 145 cells decreased to 45 % for MCF7 cells and 30 % for DU145 cells.

Overall results demonstrated the great potential of gold nanostructures as photothermal therapy agents.

The following suggestions can be made for further improving this study;

1. A suitable laser at 950 nm or higher may be used to determine the photothermal effect of AuNRs with higher AR.
2. Different lipid types for liposome preparation may be tried and compared in order to improve cell interactions.
3. AuNBs containing a higher number and different lengths of AuNRs may be synthesized. These structures can be characterized in detail to determine the effect of the physical properties on the photothermal effect.
4. The targeted AuNRs can be investigated as contrast agents for the diagnosis of cancer.

REFERENCES

- Abe, K.; Higashi, K.; Watabe, K.; Kobayashi, A.; Limwikrant, W.; Yamamoto, K.; Moribe, K. "Effects of the PEG molecular weight of a PEG-lipid and cholesterol on PEG chain flexibility on liposome surfaces." *Colloids and Surfaces A: Physicochem. Eng. Aspects* **2015**, 474, 63–70.
- Ahmed, W.; Glass, C.; van Ruitenbeek, J. M. "Facile synthesis of gold nanoworms with a tunable length and aspect ratio through oriented attachment of nanoparticles." *Nanoscale* **2014**, 6, 13222-13227.
- Ahn, S.; Seo, E.; Kim, K.; Lee, S. J. "Controlled cellular uptake and drug efficacy of nanotherapeutics." *Scientific Reports* **2013**, 3(1997), 1-10.
- Alagiri, M.; Rameshkumar, P.; Pandikumar, A. "Gold nanorod-based electrochemical sensing of small biomolecules: A review." *Microchimica Acta* **2017**, 184(9), 3069–3092.
- Alkilany, A. M.; Murphy, C. J. "Toxicity and cellular uptake of gold nanoparticles: What we have learned so far?." *J Nanopart Res* **2010**, 12, 2313–2333.
- Alkilany, A. M.; Nalaria, P. K.; Hexel, C. R.; Shaw, T. J.; Murphy, C. J.; Wyatt, M. D. "Cellular Uptake and Cytotoxicity of Gold Nanorods: Molecular Origin of Cytotoxicity and Surface Effects." *Small* **2009**, 5(6), 701–708.
- Alkilany, A. M.; Thompson, L. B.; Boulos, S. P.; Sisco, P. N.; Murphy, C. J. "Gold nanorods: their potential for photothermal therapeutics and drug delivery, tempered by the complexity of their biological interactions." *Advanced drug delivery reviews* **2012**, 64(2), 190-199.
- American Cancer Society: Cancer Facts and Figures. Atlanta, Ga: American Cancer Society, **2018**.
- Attwood, S. J.; Choi, Y.; Leonenko, Z. "Preparation of DOPC and DPPC Supported Planar Lipid Bilayers for Atomic Force Microscopy and Atomic Force Spectroscopy." *International Journal of Molecular Sciences* **2013**, 14, 3514-3539.
- Atwater, H. A.; Polman, A. "Plasmonics for Improved Photovoltaic Devices." *Nat. Mater.* **2010**, 9, 205–213.
- Ba, H.; Rodríguez-Fernández, J.; Stefani, F. D.; Feldmann, J. "Immobilization of Gold Nanoparticles on Living Cell Membranes upon Controlled Lipid Binding." *Nano Lett.* **2010**, 10, 3006–3012.
- Basiruddin, S.; Saha, A.; Pradhan, N.; Jana, N. R. "Functionalized Gold Nanorod Solution via Reverse Micelle Based Polyacrylate Coating." *Langmuir* **2010**, 26(10), 7475-7481.

- Battaglia, L.; Ugazio, E. "Lipid Nano- and Microparticles: An Overview of Patent-Related Research." *Hindawi Journal of Nanomaterials* **2019**, Article ID 2834941, 22 pages.
- Boca, S. C.; Astilean, S. "Detoxification of gold nanorods by conjugation with thiolated poly (ethylene glycol) and their assessment as SERS- active carriers of Raman tags." *Nanotechnology* **2010**, 21(23), 235601.
- Boisselier, E.; Astruc, D. "Gold nanoparticles in nanomedicine: preparations, imaging, diagnostics, therapies and toxicity." *Chem. Soc. Rev.* **2009**, 38, 1759–1782.
- Boswell, C. A.; Tesar, D. B.; Mukhyala, K.; Theil, F.-P.; Fielder, P. J.; Khawli, L. A. "Effects of Charge on Antibody Tissue Distribution and Pharmacokinetics." *Bioconjugate Chem.* **2010**, 21, 2153–2163.
- Burke, A. R.; Singh, R. N.; Carroll, D. L.; Wood, J. C. S.; D'Agostino Jr., R. B.; Ajayan, P. M.; Torti, F. M.; Torti, S. V. "The resistance of breast cancer stem cells to conventional hyperthermia and their sensitivity to nanoparticle-mediated photothermal therapy." *Biomaterials* **2012**, 33(10), 2961-2970.
- Busbee, B. D.; Obare, S. O.; Murphy, C. J. "An Improved Synthesis of High-Aspect-Ratio Gold Nanorods." *Advanced Materials* **2003**, 15(5), 414-416.
- Campion, A.; Kambhampati, P. "Surface-enhanced Raman scattering." *Chem. Soc. Rev.* **1998**, 27(4), 241-250.
- Cao, J.; Suna, T.; Grattan, K. T.V. "Gold nanorod-based localized surface plasmon resonance biosensors: A review." *Sensors and Actuators B* **2014**, 195, 332–351.
- Carpin, L.; Bickford, L.; Agollah, G.; Yu, T.-K.; Schiff, R.; Li, Y.; Drezek, R. "Immunoconjugated gold nanoshell-mediated photothermal ablation of trastuzumab-resistant breast cancer cells." *Breast Cancer Res Treat* **2011**, 125(1), 27-34.
- Centi, S.; Tatini, F.; Ratto, F.; Gnerucci, A.; Mercatelli, R.; Romano, G.; Landini, I.; Nobili, S.; Ravalli, A.; Marrazza, G.; Mini, E.; Fusi, F.; Pini, R. "In vitro assessment of antibody-conjugated gold nanorods for systemic injections." *Journal of Nanobiotechnology* **2014**, 12(55), 1-10.
- Chanda, N.; Shukla, R.; Katti, K. V.; Kannan, R. "Gastrin Releasing Protein Receptor Specific Gold Nanorods: Breast and Prostate Tumor Avid Nanovectors for Molecular Imaging." *Nano Lett.* **2009**, 9(5), 1798-1805.
- Charan, S.; Sanjiv, K.; Singh, N.; Chien, F.-C.; Chen, Y.-F.; Nergui, N. N.; Huang, S.-H.; Kuo, C. W.; Lee, T.-C.; Chen, P. "Development of Chitosan Oligosaccharide-Modified Gold Nanorods for *in vivo* Targeted Delivery and Noninvasive Imaging by NIR Irradiation." *Bioconjugate Chemistry* **2012**, 23(11), 2173-2182.
- Chauhan, D. S.; Prasad, R.; Devrukhkar, J.; Selvaraj, K.; Srivastava, R. "Disintegrable NIR Light Triggered Gold Nanorods Supported Liposomal Nanohybrids for Cancer Theranostics." *Bioconjugate Chem.* **2018**, 29, 1510–1518.

- Chen, C.-D.; Cheng, S.-F.; Chau, L.-K.; Wang, C. R. C. "Sensing capability of the localized surface plasmon resonance of gold nanorods." *Biosensors and Bioelectronics* **2007**, 22(6), 926-932.
- Chen, H.; Shao, L.; Li, Q.; Wang, J. "Gold Nanorods and their plasmonic properties." *Chem. Soc. Rev.* **2013**, 42, 2679-2724.
- Chen, Q.; Wen, J.; Li, H.; Xu, Y.; Liu, F.; Sun, S. "Recent advances in different modal imaging-guided photothermal therapy." *Biomaterials* **2016**, 106, 144-166.
- Chhatre, A.; Thaokar, R.; Mehra, A. "Formation of Gold Nanorods by Seeded Growth: Mechanisms and Modeling." *Cryst. Growth Des.* **2018**, 18, 3269–3282.
- Chibowski, E.; Szczes, A. "Zeta potential and surface charge of DPPC and DOPC liposomes in the presence of PLC enzyme." *Adsorption* **2016**, 22, 755–765.
- Chithrani, B. D., Ghazani, A. A., and Chan, W. C. "Determining the size and shape dependence of gold nanoparticle uptake into mammalian cells." *Nano Lett.* **2006**, 6, 662–668.
- Cho, S. K.; Emoto, K.; Su, L.-J.; Yang, X.; Flaig, T. W.; Park, W. "Functionalized Gold Nanorods for Thermal Ablation Treatment of Bladder Cancer." *Journal of Biomedical Nanotechnology* **2014**, 10(7), 1267-1276.
- Choi, W. I.; Kim, J.-Y.; Kang, C.; Byeon, C. C.; Kim, Y. H.; Tae, G. "Tumor regression *in vivo* by photothermal therapy based on gold-nanorod-loaded, functional nanocarriers." *ACS Nano* **2011**, 5(3), 1995-2003.
- Connor, E. E.; Mwamuka, J.; Gole, A.; Murphy, C. J.; Wyatt, M. D. "Gold Nanoparticles Are Taken Up by Human Cells but Do Not Cause Acute Cytotoxicity." *Small* **2005**, 1(3), 325-327.
- Cortie, M. B.; Cortie, D. L.; Timchenko, V. "Heat transfer from nanoparticles for targeted destruction of infectious organisms." *International Journal of Hyperthermia* **2018**, 34(2), 157–167.
- Curado, M. P. "World incidence and mortality of breast cancer." *Artículo de revision* **2011**, 53, 372-384.
- Daniel, M.-C.; Astruc, D. "Gold Nanoparticles: Assembly, Supramolecular Chemistry, Quantum-Size-Related Properties, and Applications toward Biology, Catalysis, and Nanotechnology." *Chemical Reviews* **2003**, 104(1), 293-346.
- Dickerson, E. B.; Dreaden, E. C.; Huang, X.; El-Sayed, I. H.; Chu, H.; Pushpanketh, S.; McDonald, J. F.; El-Sayed, M. A. "Gold nanorod assisted near-infrared plasmonic photothermal therapy (PPTT) of squamous cell carcinoma in mice." *Cancer Letters* **2008**, 269(1), 57-66.
- Eghtedari, M.; Liopo, A. V.; Copland, J. A.; Oraevsky, A. A.; Motamedi, M. "Engineering of Hetero-Functional Gold Nanorods for the *in vivo* Molecular Targeting of Breast Cancer Cells." *Nano Letters* **2009**, 9(1), 287-291.
- El-Sayed, I. H.; Huang, X.; El-Sayed, M. A. "Surface Plasmon Resonance Scattering and Absorption of anti-EGFR Antibody Conjugated Gold Nanoparticles in Cancer

- Diagnostics: Applications in Oral Cancer.” *Nano Letters* **2005**, 5(5), 829-834. 190.
- Esumi, K.; Matsuhisa, K.; Torigoe, K. “Preparation of Rodlike Gold Particles by UV Irradiation Using Cationic Micelles as a Template.” *Langmuir* **1995**, 11(9), 3285-3287.
- Eustis, S.; El-Sayed, M. “Aspect Ratio Dependence of the Enhanced Fluorescence Intensity of Gold Nanorods: Experimental and Simulation Study.” *The Journal of Physical Chemistry B* **2005**, 109(34), 16350-16356.
- Eustis, S.; El-Sayed, M. A. “Determination of the aspect ratio statistical distribution of gold nanorods in solution from a theoretical fit of the observed inhomogeneously broadened longitudinal plasmon resonance absorption spectrum.” *J. Appl. Phys.* **2006**, 100, 044324.
- Fantechi, E.; Innocenti, C.; Zanardelli, M.; Fittipaldi, M.; Falvo, E.; Carbo, M. “A smart platform for hyperthermia application in cancer treatment: cobalt-doped ferrite nanoparticles mineralized in human ferritin cages.” *ACS Nano* **2014**, 8, 4705–4719.
- Faraday, M. “The Bakerian Lecture: Experimental Relations of Gold (and Other Metals) to Light.” *Philosophical Transactions of the Royal Society of London* **1857**, 147, 145-181.
- Filion, M. C., Philips, N. C. “Toxicity and immunomodulatory activity of liposomal vectors formulated with cationic lipids toward immune effector cells.” *Biochimica et Biophysica Acta* **1997**, 1329, 345–356.
- Freestone, I.; Meeks, N.; Sax, M.; Higgitt, C. “The Lycurgus Cup — A Roman nanotechnology.” *Gold Bulletin* **2007**, 40(4), 270-277.
- Foss Jr, C. A.; Hornyak, G. L., Stockert, J. A.; Martin, C. R. “Template-synthesized nanoscopic gold particles: optical spectra and the effects of particle size and shape.” *The Journal of Physical Chemistry* **1994**, 98(11), 2963-2971.
- Fratoddi, I.; Venditti, I.; Cametti, C.; Russo, M. V. “Gold nanoparticles and gold nanoparticle-conjugates for delivery of therapeutic molecules. Progress and challenges.” *J. Mater. Chem. B* **2014**, 2, 4204-4220.
- Fubini, B.; Fenoglio, I.; Turci, F. “Effect of chemical composition and state of the surface on the toxic response to high aspect ratio nanomaterial.” *Nanotoxicology: Materials & Methods* **2011**, 6(5), 899–920.
- Gao, J.; Bender, C. M.; Murphy, C. J. “Dependence of the Gold Nanorod Aspect Ratio on the Nature of the Directing Surfactant in Aqueous Solution.” *Langmuir* **2003**, 19(21), 9065-9070.
- Gormley, A. J.; Malugin, A.; Ray, A.; Robinson, R.; Ghandehari, H. “Biological evaluation of RGDfK-gold nanorod conjugates for prostate cancer treatment.” *Journal of Drug Targeting* **2011**, 19(10), 915–924.

- Grabinski, C.; Schaeublin, N.; Wijaya, A.; D’Couto, H.; Baxamusa, S. H.; Hamad-Schifferli, K.; Hussain, S. M. “Effect of Gold Nanorod Surface Chemistry on Cellular Response.” *ACS Nano* **2011**, 5(4), 2870–2879.
- Gole, A.; Murphy, C. J. “Seed-Mediated Synthesis of Gold Nanorods: Role of the Size and Nature of the Seed.” *Chemistry of Materials* **2004**, 16(19), 3633–3640.
- Green, H. N.; Martyshkin, D. V.; Rodenburg, C. M.; Rosenthal, E. L.; Mirov, S. B. “Gold Nanorod Bioconjugates for Active Tumor Targeting and Photothermal Therapy.” *Journal of Nanotechnology* **2011**.
- Heidari, Z.; Sariri, R.; Salouti, M. “Gold nanorods-bombesin conjugate as a potential targeted imaging agent for detection of breast cancer.” *Journal of Photochemistry and Photobiology B: Biology* **2014**, 130, 40–46.
- Hermanson, G. T. *Bioconjugate Techniques*. Academic Press: **2008**.
- Hirsch, L. R.; Stafford, R. J.; Bankson, J. A.; Sershen, S. R.; Rivera, B.; Price, R. E.; Hazle, J. D.; Halas, N. J.; West J. L. “Nanoshell-mediated near-infrared thermal therapy of tumors under magnetic resonance guidance.” *Proc. Natl. Acad. Sci. USA* **2003**, 100, 13549–13554.
- Hou, H.; Chen, L.; He, H.; Chen, L.; Zhao, Z.; Jin, Y. “Fine-tuning the LSPR response of gold nanorod–polyaniline core–shell nanoparticles with high photothermal efficiency for cancer cell ablation.” *Journal of Materials Chemistry B* **2015**, 3(26), 5189–5196.
- Huang, N.; Wang, H.; Zhao, J.; Lui, H.; Korbelik, M.; Zeng, H. “Single-wall carbon nanotubes assisted photothermal cancer therapy: animal study with a murine model of squamous cell carcinoma.” *Lasers Surg. Med.* **2010**, 42, 638–648.
- Huang, X.; El-Sayed, M. “Gold nanoparticles: Optical properties and implementations in cancer diagnosis and photothermal therapy.” *Journal of Advanced Research* **2010**, 1(1), 13–28.
- Huang, X.; Peng, X.; Wang, Y.; Wang, Y.; Shin, D. M.; El-Sayed, M. A.; Nie, S. “A Reexamination of Active and Passive Tumor Targeting by Using Rod-Shaped Gold Nanocrystals and Covalently Conjugated Peptide Ligands.” *ACS Nano* **2010**, 4(10), 5887–5896.
- Huang, X.; Tang, S.; Liu, B.; Ren, B.; Zheng, N. “Enhancing the Photothermal Stability of Plasmonic Metal Nanoplates by a Core-Shell Architecture.” *Advanced Materials* **2011**, 23(30), 3420–3425.
- Huang, X. H.; El-Sayed, I. H.; Qian, W.; El-Sayed, M. A. “Cancer Cell Imaging and Photothermal Therapy in the Near-Infrared Region by Using Gold Nanorods.” *J. Am. Chem. Soc.* **2006**, 128, 2115–2120.
- Huang, X. H.; Jain, P. K.; El-Sayed, I. H.; El-Sayed, M. “Plasmonic photothermal therapy (PPTT) using gold nanoparticles.” *Laser Med. Sci.* **2008**, 23, 217–228.
- Hubert, F.; Testard, F.; Rizza, G.; Spalla, O. “Nanorods versus Nanospheres: A Bifurcation Mechanism Revealed by Principal Component TEM Analysis.” *Langmuir* **2010**, 26(10), 6887–6891.

- Jain, P. K.; Lee, K. S.; El-Sayed, I. H.; El-Sayed, M. A. “Calculated absorption and scattering properties of gold nanoparticles of different size, shape, and composition: applications in biological imaging and biomedicine.” *The Journal of Physical Chemistry B* **2006**, 110(14), 7238-7248.
- Jakša, G. “AFM and XPS Study of Aminosilanes on Si.” *Imaging & Microscopy* **2014**.
- Jana, N. R.; Gearheart, L.; Murphy, C. J. “Wet chemical synthesis of high aspect ratio cylindrical gold nanorods.” *The Journal of Physical Chemistry B* **2001**, 105(19), 4065-4067.
- Jana, N. R. “Gram-Scale Synthesis of Soluble, Near-Monodisperse Gold Nanorods and Other Anisotropic Nanoparticles.” *Small* **2005**, 1(8-9), 875-882.
- Jemal A.; Siegel, R.; Ward, E.; Hao, Y.; Xu, J.; Murray, T.; Thun, M. J. “Cancer statistics.” *CA Cancer J Clin.* **2008**, 58(2), 71-96.
- Jiang, K.; Smith, D. A.; Pinchuk, A. “Size-Dependent Photothermal Conversion Efficiencies of Plasmonically Heated Gold Nanoparticles.” *J. Phys. Chem. C* **2013**, 117(51), 27073–27080.
- Jiang, W.; Kim, B. Y.; Rutka, J. T.; Chan, W. C. “Nanoparticle-mediated cellular response is size-dependent.” *Nat. Nanotechnol.* **2008**, 3, 145–150.
- Jin, H.; Yang, P.; Cai, J.; Wang, J.; Liu, M. “Photothermal effects of folate-conjugated Au nanorods on HepG2 cells.” *Applied microbiology and biotechnology* **2012**, 94(5), 1199-1208.
- Jokerst, J. V.; Lobovkina, T.; Zare, R. N.; Gambhir, S. S. “Nanoparticle PEGylation for imaging and therapy.” *Nanomedicine* **2011**, 6(4), 715-728.
- Joshi, P. P.; Yoon, S. J.; Hardin, W. G.; Emelianov, S.; Sokolov, K. V. “Conjugation of Antibodies to Gold Nanorods through Fc Portion: Synthesis and Molecular Specific Imaging.” *Bioconjugate Chem.* **2013**, 24(6), 878–888.
- Kabashin, A. V.; Evans, P.; Pastkovsky, S.; Hendren, W.; Wurtz, G. A.; Atkinson, R.; Pollard, R.; Podolskiy, V. A.; Zayats, A. V. “Plasmonic Nanorod Metamaterials for Biosensing.” *Nat. Mater.* **2009**, 8, 867–871.
- Kang, J. H.; Ko, Y. T. “Lipid-coated gold nanocomposites for enhanced cancer therapy.” *International Journal of Nanomedicine* **2015**, 10, 33-45.
- Kang, X., Guo, X., Niu, X., An, W., Li, S., Liu, Z., Yang, Y., Wang, N., Jiang, Q., Yan, C., Wang, H., Zhang, Q. “Photothermal therapeutic application of gold nanorodsporphyrin- trastuzumab complexes in HER2-positive breast cancer.” *Sci Rep.* **2017**, 7, 42069.
- Kapp, D.; Hahn, G.; Carlson, R. “Principles of hyperthermia.” *Cancer medicine* **2000**, 5(5).
- Kaur, P.; Aliru, M. L.; Chadha, A. S.; Asea, A.; Krishnan, S. “Hyperthermia using nanoparticles—promises and pitfalls.” *Int. J. Hyperthermia* **2016**, 32, 76–88.

- Kim, C. K.; Ghosh, P.; Pagliuca, C.; Zhu, Z.-J.; Menichetti, S.; Rotello, V. M. "Entrapment of hydrophobic drugs in nanoparticle monolayers with efficient release into cancer cells." *Journal of the American Chemical Society* **2009**, 131(4), 1360-1361.
- Kim, F.; Song, J. H.; Yang, P. "Photochemical Synthesis of Gold Nanorods." *Journal of the American Chemical Society* **2002**, 124(48), 14316-14317.
- Kim, M.; Lee, J.-H.; Nam, J.-M. "Plasmonic Photothermal Nanoparticles for Biomedical Applications." *Adv. Sci.* **2019**, 6, 1900471, 1-23.
- Kiziltepe, T., Ashley, J. D.; Stefanick, J. F.; Qi, Y. M.; Alves, N. J.; Handlogten, M. W.; Suckow, M. A.; Navari, R. M.; Bilgicer, B. "Rationally engineered nanoparticles target multiple myeloma cells, overcome cell-adhesion-mediated drug resistance, and Show enhanced efficacy *in vivo*." *Blood Cancer Journal.* **2012**, 2(4), e64.
- Kneipp, K.; Kneipp, H.; Itzkan, I.; Dasari, R. R.; Feld, M. S. "Ultrasensitive chemical analysis by Raman spectroscopy." *Chemical Reviews* **1999**, 99(10), 2957-2976.
- Kopwiththaya, A.; Yong, K.-T.; Hu, R.; Roy, I.; Ding, H.; Vathy, L. A.; Bergey, E. J.; Prasad, P. N. "Biocompatible PEGylated gold nanorods as colored contrast agents for targeted *in vivo* cancer applications." *Nanotechnology* **2010**, 21, 315101 (10pp).
- Kumar, A.; Boruah, B. M.; Liang, X.-J. "Gold Nanoparticles: Promising Nanomaterials for the Diagnosis of Cancer and HIV/AIDS." *Journal of Nanomaterials* **2011**, Article ID 202187, 17 pages.
- Kumar, V.; Qin, J.; Jiang, Y.; Duncan, R. G.; Brigham, B.; Fishman, S.; Nair, J. K.; Akinc, A.; Barros, S. A.; Kasperkovitz, P. V. "Shielding of Lipid Nanoparticles for siRNA Delivery: Impact on Physicochemical Properties, Cytokine Induction, and Efficacy." *Molecular Therapy-Nucleic Acids* **2014**, 3, e210.
- Kuo, T.-R.; Hovhannisyanyan, V. A.; Chao, Y.-C.; Chao, S.-L.; Chiang, S.-J.; Lin, S.-J.; Dong, C.-Y.; Chen, C.-C. "Multiple release kinetics of targeted drug from gold nanorod embedded polyelectrolyte conjugates induced by near-infrared laser irradiation." *Journal of the American Chemical Society* **2010**, 132(40), 14163-14171.
- Lal, S. L.; Clare, S. E.; Halas, N. J. "Nanoshell-enabled photothermal cancer therapy: impending clinical impact." *Acc. Chem. Res.* 2008, 41(12), 1842–1851.
- Lal, S.; McCart Reed, A.; de Luca, X.; Simpson, P. "Molecular signatures in breast cancer." *Methods* **2017**, 131, 135-146.
- Lee, J. H.; Jang, J. T.; Choi, J. S.; Moon, S. H.; Noh, S. H.; Kim, J. W. "Exchange-coupled magnetic nanoparticles for efficient heat induction." *Nat. Nanotechnol.* **2011**, 6, 418–422.
- Lee, J. H.; Ju, J. E.; Kim, B. I.; Pak, P. J.; Choi, E. K.; Lee, H. S.; Chung, N. "Rod-shaped iron oxide nanoparticles are more toxic than sphere-shaped nanoparticles to murine macrophage cells." *Environ Toxicol Chem* **2014**, 33(12), 2759-66.

- Leekumjorn, S.; Sum, A. K. "Molecular Simulation Study of Structural and Dynamic Properties of Mixed DPPC/DPPE Bilayers." *Biophysical Journal* **2006**, 90, 3951-3965.
- Li, X.; Zhou, J.; Dong, X.; Cheng, W.-Y.; Duan, H.; Cheung, P. C. K. "In Vitro and In Vivo Photothermal Cancer Therapeutic Effects of Gold Nanorods Modified with Mushroom β Glucan." *J. Agric. Food Chem.* **2018**, 66, 4091–4098.
- Li, Z.; Huang, P.; Zhang, X.; Lin, J.; Yang, S.; Liu, B.; Gao, F.; Xi, P.; Ren, Q.; Cui, D. "RGD-Conjugated Dendrimer-Modified Gold Nanorods for *in vivo* Tumor Targeting and Photothermal Therapy." *Mol. Pharmaceutics* **2010**, 7, 1, 94-104.
- Libutti, S. K.; Paciotti, G. F.; Byrnes, A. A.; Alexander, H. R.; Gannon, W. E.; Walker, M.; Seidel, G. D.; Yuldasheva, N.; Tamarkin, L. "Phase I and Pharmacokinetic Studies of CYT-6091, a Novel PEGylated Colloidal Gold-rhTNF Nanomedicine." *Clinical Cancer Research* **2010**, 16(24), 6139-6149.
- Link, S.; El-Sayed, M. A. "Spectral properties and relaxation dynamics of surface plasmon electronic oscillations in gold and silver nanodots and nanorods." *The Journal of Physical Chemistry B* **1999**, 103(40), 8410- 8426.
- Link, S.; El-Sayed, M. "Shape and size dependence of radiative, non-radiative and photothermal properties of gold nanocrystals." *Int. Rev. in Phys. Chem.* **2000**, 19, 409-453.
- Liopo, A.; Conjuteau, A.; Tsyboulski, D.; Ermolinsky, B.; Kazansky, A.; Oraevsky, A. "Biocompatible Gold Nanorod Conjugates for Preclinical Biomedical Research." *Journal of Nanomedicine & Nanotechnology* **2012**, S2.
- Liu, J.; Liang, H.; Li, M.; Luo, Z.; Zhang, J.; Guo, X.; Cai, K. "Tumor acidity activating multifunctional nanoplatfor for NIR-mediated multiple enhanced photodynamic and photothermal tumor therapy." *Biomaterials* **2018**, 157, 107-124.
- Liu, Z.; Wang, L.; Zhang, L.; Wu, X.; Nie, G.; Chen, C.; Tang, H.; and Wang, Y. "Metabolic Characteristics of 16HBE and A549 Cells Exposed to Different Surface Modified Gold Nanorods." *Adv. Healthcare Mater.* **2016**, 1-13.
- Luo, L.; Bian, Y.; Liu, Y.; Zhang, X.; Wang, M.; Xing, S.; Li, L.; Gao, D. "Combined Near Infrared Photothermal Therapy and Chemotherapy Using Gold Nanoshells Coated Liposomes to Enhance Antitumor Effect." *Small* **2016**, 12(30), 4103-4112.
- Matthews, J. R., Payne, C. M. and Hafner, J. H. "Analysis of Phospholipid Bilayers on Gold Nanorods by Plasmon Resonance Sensing and Surface-Enhanced Raman Scattering." *Langmuir* **2015**, 31, 9893–9900.
- Merchant, B. "Gold, the Noble Metal and the Paradoxes of its Toxicology." *Biologicals* **1998**, 26(1), 49-59.
- Murphy, C. J.; Thompson, L. B.; Chernak, D. J.; Yang, J. A.; Sivapalan, S. T.; Boulos, S. P.; Huang, J.; Alkilany, A. M.; Sisco, P. N. "Gold nanorod crystal growth: From seed-mediated synthesis to nanoscale sculpting." *Current Opinion in Colloid & Interface Science* **2011**, 16, 128–134.

- Murphy, C. J.; Gole, A. M.; Hunyadi, S. E.; Stone, J. W.; Sisco, P. N.; Alkilany, A.; Kinard, B. E.; Hankins, P. "Chemical sensing and imaging with metallic nanorods." *Chem. Commun.* **2008**, 544-557.
- Niidome, T.; Yamagata, M.; Okamoto, Y.; Akiyama, Y.; Takahashi, H.; Kawano, T.; Katayama, Y.; Niidome, Y. "PEG-modified gold nanorods with a stealth character for *in vivo* applications." *Journal of Controlled Release* **2006**, 114(3), 343-347.
- Nikoobakht, B.; El-Sayed, M. A. "Preparation and Growth Mechanism of Gold Nanorods (NRs) Using Seed-Mediated Growth Method." *Chemistry of Materials* **2003**, 15(10), 1957-1962.
- Nikoobakht, B.; Wang, J.; El-Sayed, M. A. "Surface-enhanced Raman scattering of molecules adsorbed on gold nanorods: off-surface plasmon resonance condition." *Chemical Physics Letters* **2002**, 366 (1-2), 17-23.
- Ochsner, M. "Photophysical and photobiological processes in the photodynamic therapy of tumours." *J. Photochem. Photobiol. B Biol.* **1997**, 39, 1-18.
- Orendorff, C. J.; Alam, T. M.; Sasaki, D. Y.; Bunker, B. C.; Voigt, J. A. "Phospholipid-Gold Nanorod Composites." *ACS Nano* **2009**, 3(4), 971-983.
- Oyelere, A. K.; Chen, P. C.; Huang, X.; El-Sayed, I. H.; El-Sayed, M. "Peptide-Conjugated Gold Nanorods for Nuclear Targeting." *Bioconjugate Chem.* **2007**, 18, 1490-1497.
- Oyelere, A. K.; El-Sayed, M. A.; Dreaden, E. C. Targeted Cellular Delivery of Nanoparticles. Google Patents US20110077581A1, **2010**.
- Paciotti, G. F.; Myer, L.; Weinreich, D.; Goia, D.; Pavel, N.; McLaughlin, R. E.; Tamarkin, L. "Colloidal Gold: A Novel Nanoparticle Vector for Tumor Directed Drug Delivery." *Drug Delivery* **2004**, 11(3), 169-183.
- Papavassiliou, G. C. "Optical properties of small inorganic and organic metal particles." *Progress in Solid State Chemistry* **1979**, 12(3), 185-271.
- Paramasivam, G.; Kayambu, N.; Rabel, A. M.; Sundramoorthy, A. K.; Sundaramurthy, A. "Anisotropic noble metal nanoparticles: Synthesis, surface functionalization and applications in biosensing, bioimaging, drug delivery and theranostics." *Acta Biomaterialia* **2017**, 49, 45-65.
- Park, K. "Synthesis, Characterization, and Self-Assembly of Size Tunable Gold Nanorods" Georgia Institute of Technology **2006**.
- Park, K.; Drummy, L. F.; Wadams, R. C.; Koerner, H.; Nepal, D.; Fabris, L.; Vaia, R. A. "Growth Mechanism of Gold Nanorods." *Chem. Mater.* **2013**, 25, 555-563.
- Pelicano, H.; Martin, D.; Xu, R.; Huang, P. "Glycolysis inhibition for anticancer treatment." *Oncogene* **2006**, 25(34), 4633-4646.
- Perez-Juste, J.; Pastoriza-Santos, I.; Liz-Marzan, L. M.; Mulvaney, P. "Gold nanorods: synthesis, characterization and applications." *Coordination Chemistry Reviews* **2005**, 249(17), 1870-1901.

- Pérez-Juste, J.; Liz-Marzán, L. M.; Carnie, S.; Chan, D. Y. C.; Mulvaney, P. "Electric-Field-Directed Growth of Gold Nanorods in Aqueous Surfactant Solutions." *Advanced Functional Materials* **2004**, 14(6), 571-579.
- Pissuwan, D., Valenzuela, S. M., Cortie, M. B. "Prospects for Gold Nanorod Particles in Diagnostic and Therapeutic Applications." *Biotechnology and Genetic Engineering Reviews* **2008**, 25(1), 93-112.
- Prasad, V.; Mikhailovsky, A.; Zasadzinski, J. A. "Inside-out disruption of silica/gold core-shell nanoparticles by pulsed laser irradiation." *Langmuir* **2005**, 21(16), 7528-7532.
- Pollard, A. M.; Heron, C. *Archaeological Chemistry*. Royal Society of Chemistry: Cambridge, **2008**.
- Qian, X.; Peng, X.-H.; Ansari, D. O.; Yin-Goen, Q.; Chen, G. Z.; Shin, D. M.; Yang, L.; Young, A. N.; Wang, M. D.; Nie, S. "In vivo tumor targeting and spectroscopic detection with surface-enhanced Raman nanoparticle tags." *Nature Biotechnology* **2007**, 26(1), 83-90.
- Qiu, Y.; Liu, Y.; Wang, L.; Xu, L.; Bai, R.; Ji, Y.; Wu, X.; Zhao, Y.; Li, Y.; Chen, C. "Surface chemistry and aspect ratio mediated cellular uptake of Au nanorods." *Biomaterials* **2010**, 31(30), 7606-7619.
- Ray, P. C.; Khan, S. A.; Singh, A. K.; Senapati, D.; Fan, Z. "Nanomaterials for targeted detection and photothermal killing of bacteria." *Chem. Soc. Rev.* **2012**, 41, 3193-3209.
- Rayavarapu, R. G.; Petersen, W.; Hartsuiker, L.; Chin, P.; Janssen, H.; van Leeuwen, F. W. B.; Otto, C.; Manohar, S.; van Leeuwen, T. G. "In vitro toxicity studies of polymer-coated gold nanorods." *Nanotechnology* **2010**, 21, 145101 (10pp).
- Rejiya, C, S.; Kumar, J.; Raji, V.; Vibin, M. and Abraham, A. "Laser immunotherapy with gold nanorods causes selective killing of tumour cells." *Pharmacol Res* **2012**, 65(2), 261-269.
- Rengan, A. K.; Bukhari, A. B.; Pradhan, A.; Malhotra, R.; Banerjee, R.; Srivastava, R.; De, A. "In Vivo Analysis of Biodegradable Liposome Gold Nanoparticles as Efficient Agents for Photothermal Therapy of Cancer." *Nano Lett.* **2015**, 15, 842-848.
- Rengan, A. K.; Jagtap, M.; De, A.; Banerjee, R.; Srivastava, R. "Multifunctional gold coated thermo-sensitive liposomes for multimodal imaging and photo-thermal therapy of breast cancer cells." *Nanoscale* **2014**, 6, 916-923.
- Riley, R.; Day, E. "Gold nanoparticle-mediated photothermal therapy: applications and opportunities for multimodal cancer treatment." *Wiley Interdisciplinary Reviews: Nanomedicine and Nanobiotechnology* **2017**, 9(4), 1449.
- Roberts, M.; Bentley, M.; Harris, J. *Chemistry for peptide and protein PEGylation*. *Advanced drug delivery reviews* **2012**.

- Root, S. W.; Andrews, G.A.; Kniseley, R.M.; Tyor, M. P. “The distribution and radiation effects of intravenously administered colloidal gold-198 in man.” *Cancer* **1954**, 7, 856–866.
- Rosi, N. L.; Mirkin, C. A. “Nanostructures in biodiagnostics.” *Chem. Rev.* **2005**, 105, 1547–1562.
- Salatin, S.; Khosroushahi, A. Y. “Overviews on the cellular uptake mechanism of polysaccharide colloidal nanoparticles.” *J. Cell. Mol. Med.* **2017**, 21(9), 1668-1686.
- Santhosh, P. B.; Thomas, N.; Sudhakar, S.; Chadha, A.; Mani, E. “Phospholipid stabilized gold nanorods: towards improved colloidal stability and biocompatibility.” *Phys. Chem. Chem. Phys.* **2017**, 19, 18494-18504.
- Sau, T. K.; Murphy, C. J. “Room temperature, high-yield synthesis of multiple shapes of gold nanoparticles in aqueous solution.” *Journal of the American Chemical Society* **2004**, 126(28), 8648-8649.
- Sau, T. K.; Murphy, C. J. “Seeded High Yield Synthesis of Short Au Nanorods in Aqueous Solution.” *Langmuir* **2004**, 20(15), 6414-6420.
- Scarabelli, L.; Grzelczak, M.; Liz-Marzán, L. M. “Tuning Gold Nanorod Synthesis through Prereduction with Salicylic Acid.” *Chem. Mater.* **2013**, 25(21), 4232-4238.
- Sharma, V.; Park, K.; Srinivasarao, M. “Colloidal dispersion of gold nanorods: Historical background, optical properties, seed-mediated synthesis, shape separation and self-assembly.” *Materials Science and Engineering R* **2009**, 65, 1–38.
- Shukla, R.; Bansal, V.; Chaudhary, M.; Basu, A.; Bhonde, R. R.; Sastry, M. “Biocompatibility of Gold Nanoparticles and Their Endocytotic Fate Inside the Cellular Compartment: A Microscopic Overview.” *Langmuir* **2005**, 21(23), 10644-10654.
- Smith, D. K.; Korgel, B. A. “The Importance of the CTAB Surfactant on the Colloidal Seed-Mediated Synthesis of Gold Nanorods.” *Langmuir* **2008**, 24(3), 644- 649.
- Strickland, A. D.; Batt, C. A. “Detection of carbendazim by surface- enhanced Raman scattering using cyclodextrin inclusion complexes on gold nanorods.” *Analytical chemistry* **2009**, 81(8), 2895-2903.
- Stuchinskaya, T.; Moreno, M.; Cook, M. J.; Edwards, D. R.; Russell, D. A. “Targeted photodynamic therapy of breast cancer cells using antibody-phthalocyanine-gold nanoparticle conjugates.” *Photochem. Photobiol. Sci.* **2011**, 10, 822–831.
- Takahashi, H., Niidome, Y.; Niidome, T.; Kaneko, K.; Kawasaki, H.; Yamada, S. “Modification of gold nanorods using phosphatidylcholine to reduce cytotoxicity.” *Langmuir* **2006**, 22(1), 2-5.

- Takahashi, H.; Niidome, T.; Kawano, T.; Yamada, S.; Niidome, Y. "Surface modification of gold nanorods using layer-by-layer technique for cellular uptake." *Journal of Nanoparticle Research* **2008**, 10(1), 221-228.
- Tomak, A. Nanostructures For Plasmonic Biosensors. MSc. Thesis, Gediz University, Izmir, Turkey, **2013**.
- Tong, L.; Zhao, Y.; Huff, T. B.; Hansen, M. N.; Wei, A.; Cheng, J. X. "Gold nanorods mediate tumor cell death by compromising membrane integrity." *Adv. Mater.* **2007**, 19, 3136– 3141.
- Truong, P. L.; Kima, B. W.; Sim, S. J. "Rational aspect ratio and suitable antibody coverage of gold nanorod for ultra-sensitive detection of a cancer biomarker." *Lab Chip* **2012**, 12, 1102-1109.
- Troutman, T. S.; Barton, J. K.; Romanowski, M. "Biodegradable Plasmon Resonant Nanoshells." *Adv. Mater.* **2008**, 20(13), 2604-2608.
- Tsai, M.-F.; Chang, S.-H. G.; Cheng, F.-Y.; Shanmugam, V.; Cheng, Y.-S.; Su, C.-H.; Yeh, C.-S. "Au Nanorod Design as Light-Absorber in the First and Second Biological Near-Infrared Windows for *in vivo* Photothermal Therapy." *ACS Nano* **2013**, 7(6), 5330-5342.
- Turkevitch, J.; Stevenson, P. C.; Hillier, J. "A study of the nucleation and growth processes in the synthesis of colloidal gold." *Discussions of the Faraday Society* **1951**, 11, 55–75.
- Vendrell, M.; Maiti, K. K.; Dhaliwal, K.; Chang, Y.-T. "Surface-enhanced Raman scattering in cancer detection and imaging." *Trends in biotechnology* **2013**, 1(4), 249-257.
- Vigderman, L.; Khanal, B. P.; Zubarev, E. R. "Functional Gold Nanorods: Synthesis, Self-Assembly, and Sensing Applications." *Advanced Materials* **2012**, 24(36), 4811-4841.
- Vines, J. B.; Yoon, J.-H.; Ryu, N.-E.; Lim, D.-J.; Park, H. "Gold Nanoparticles for Photothermal Cancer Therapy." *Front. Chem.* **2019**, 7(167), 1-16.
- Von Maltzahn, G.; Park, J.-H.; Agrawal, A.; Bandaru, N. K.; Das, S. K.; Sailor, M. J.; Bhatia, S. N. "Computationally guided photothermal tumor therapy using long-circulating gold nanorod antennas." *Cancer research* **2009**, 69(9), 3892-3900.
- Wang, H.; Thorling, C. A.; Liang, X.; Bridle, K. R.; Grice, J. E.; Zhu, Y.; Crawford, D. H. G.; Xu, Z. P.; Liu, X.; Roberts, M. S. "Diagnostic imaging and therapeutic application of nanoparticles targeting the liver." *J. Mater. Chem. B* **2015**, 3, 939–958.
- Wang, L. B.; Zhu, Y. Y.; Xu, L. G.; Chen, W.; Kuang, H.; Liu, L. Q.; Agarwal, A.; Xu, C. L.; Kotov, N. A. "Side-by-Side and End-to-End Gold Nanorod Assemblies for Environmental Toxin Sensing." *Angew. Chem., Int. Ed.* **2010**, 49, 5472–5475.
- Wang, P.; Wang, X.; Wang, L.; Hou, X.; Liu, W.; Chen, C. "Interaction of gold nanoparticles with proteins and cells." *Sci. Technol. Adv. Mater.* **2015**, 16, 034610 (15pp).

- Wang, X.; Li, J.; Kawazoe, N.; Chen, G. “Photothermal Ablation of Cancer Cells by Albumin-Modified Gold Nanorods and Activation of Dendritic Cells.” *Materials* **2019**, 12(31), 1-12.
- Wang, X.; Wang, Y. Q.; Chen, Z.; Shin, D. M. “Advances of Cancer Therapy by Nanotechnology.” *Cancer Research and Treatment* **2009**, 41(1), 1-11.
- Webb, J. A.; Bardhan, R. “Emerging advances in nanomedicine with engineered gold nanostructures.” *Nanoscale* **2014**, 6, 2502–2530.
- Wijaya, A.; Schaffer, S. B.; Pallares, I. G.; Hamad-Schifferli, K. “Selective Release of Multiple DNA Oligonucleotides from Gold Nanorods.” *ACS Nano* **2009**, 3, 80–86.
- Wilson, B. C.; Patterson, M. S. “The physics, biophysics and technology of photodynamic therapy.” *Phys. Med. Biol.* **2008**, 53, R61–R109.
- Wu, H.-Y.; Chu, H.-C.; Kuo, T.-J.; Kuo, C.-L.; Huang, M. H. “Seed-Mediated Synthesis of High Aspect Ratio Gold Nanorods with Nitric Acid.” *Chemistry of Materials* **2005**, 17(25), 6447-6451.
- Wust, P.; Hildebrandt, B.; Sreenivasa, G.; Rau, B.; Gellermann, J.; Riess, H.; Felix, R.; Schlag, P. “Hyperthermia in combined treatment of cancer.” *The lancet oncology* **2002**, 3(8), 487-497.
- Xiao, Y.; Hong, H.; Matson, V. Z.; Javadi, A.; Xu, W.; Yang, Y.; Zhang, Y.; Engle, J. W.; Nickles, R. J.; Cai, W. “Gold nanorods conjugated with doxorubicin and cRGD for combined anticancer drug delivery and PET imaging.” *Theranostics* **2012**, 2(8), 757.
- Xu, W.; Qian, J.; Hou, G.; Wang, Y.; Wang, J.; Sun, T.; Ji, L.; Suo, A.; Yao, Y. “PEGylated hydrazided gold nanorods for pH-triggered chemo/photodynamic/photothermal triple therapy of breast cancer.” *Acta Biomaterialia* **2018**, 82, 171–183.
- Xue, X.; Wang, F.; Liu, X. “Emerging Functional Nanomaterials for Therapeutics.” *J. Mater. Chem.* **2011**, 21, 13107–13127.
- Ye, X.; Jin, L.; Caglayan, H.; Chen, J.; Xing, G.; Zheng, C.; Doan-Nguyen, V.; Kang, Y.; Engheta, N.; Kagan, C. R.; Murray, C. B. “Improved Size-Tunable Synthesis of Monodisperse Gold Nanorods through the Use of Aromatic Additives.” *ACS Nano* **2012**, 6(3), 2804–2817.
- Ye, X.; Zheng, C.; Chen, J.; Gao, Y.; Murray, C. B. “Using Binary Surfactant Mixtures To Simultaneously Improve the Dimensional Tunability and Monodispersity in the Seeded Growth of Gold Nanorods.” *Nano Lett.* **2013**, 13(2), 765–771.
- Yeh, Y.; Creran, B.; Rotello, V. “Gold nanoparticles: preparation, properties, and applications in bionanotechnology.” *Nanoscale* **2012**, 4(6), 1871-1880.

- Yoo, J.-H., Han, H. S., Lee, C., Yoo, K.-P., Kang, T. "Surface-Enhanced Raman Scattering-Based Detection of Molecules in an Aqueous Solution via Lipid-Modified Gold Nanorods." *Journal of Nanoscience and Nanotechnology* **2013**, 13(11), 7239-7244.
- Yu, C.; Irudayaraj, J. "Multiplex Biosensor Using Gold Nanorods." *Analytical Chemistry* **2006**, 79(2), 572-579.
- Yu; Chang, S.-S.; Lee, C.-L.; Wang, C. R. C. "Gold Nanorods: Electrochemical Synthesis and Optical Properties." *The Journal of Physical Chemistry B* **1997**, 101(34), 6661-6664.
- Yuan, H.; Fales, A. M.; Vo-Dinh, T. "TAT Peptide-Functionalized Gold Nanostars: Enhanced Intracellular Delivery and Efficient NIR Photothermal Therapy Using Ultralow Irradiance." *Journal of the American Chemical Society* **2012**, 134(28), 11358-11361.
- Zhang, L.; Sun, X.; Song, Y.; Jiang, X.; Dong, S.; Wang, E. "Didodecyldimethylammonium Bromide Lipid Bilayer-Protected Gold Nanoparticles: Synthesis, Characterization, and Self-Assembly." *Langmuir* **2006**, 22, 2838-2843.
- Zhang, Z.; Lin M. "Fast loading of PEG-SH on CTAB-protected gold nanorods." *RSC Adv.* **2014**, 4, 17760.
- Zhang, Z.; Wang, J.; Chen, C. "Gold Nanorods Based Platforms for Light-Mediated Theranostics." *Theranostics* **2013**, 3(3), 223-238.
- Zhao, J.; Bradbury, C. R.; Fermin J. D. "Long-Range Electronic Communication between Metal Nanoparticles and Electrode Surfaces Separated by Polyelectrolyte Multilayer Films." *J. Phys. Chem. C* **2008**, 112, 6832-6841.
- Zhu, D.; Wang, Z.; Zong, S.; Zhang, Y.; Chen, C.; Zhang, R.; Yun, B.; Cui, Y. "Investigating the Intracellular Behaviors of Liposomal Nanohybrids via SERS: Insights into the Influence of Metal Nanoparticles." *Theranostics* **2018**, 8(4), 941-954.
- Zhu, J.; Gong, T.; Kopwiththaya, A.; Hu, R.; Law, W. C.; Roy, I.; Huang, H.; Yong, K. T. "Synthesis of PEGylated gold nanorods (Au NRs) as absorption nanoprobes for near-infrared optical imaging." *RSC Advances* **2013**, 3, 12280.
- Zijlstra, P.; Bullen, C.; Chon, J. W. M.; Gu, M. "High-Temperature Seedless Synthesis of Gold Nanorods." *The Journal of Physical Chemistry B* **2006**, 110(39), 19315-19318.
- Zijlstra, P.; Chon, J. W. M.; Gu, M. "Five-Dimensional Optical Recording Mediated by Surface Plasmons in Gold Nanorods." *Nature* **2009**, 459, 410-413.
- Zweifel, D. A.; Wei, A. "Sulfide-Arrested Growth of Gold Nanorods." *Chemistry of Materials* **2005**, 17(16), 4256-4261.

APPENDIX A

CELL NUMBER DETERMINATION

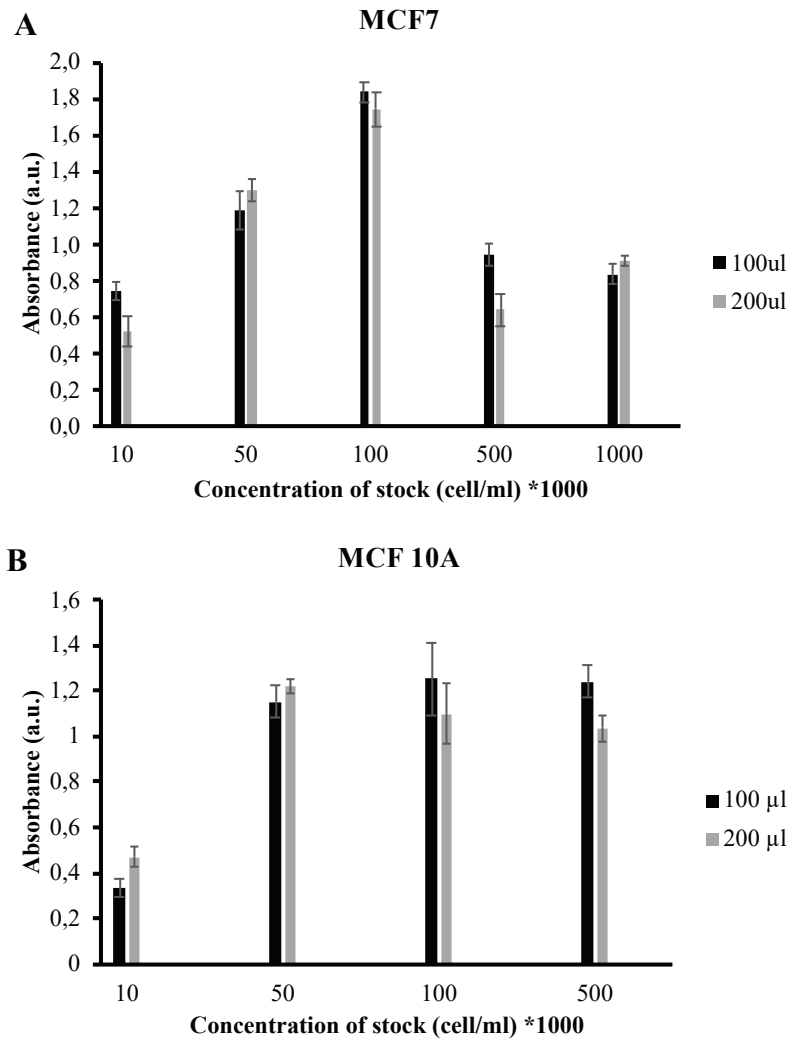


Figure A1. Cell number determination results of (A) MCF7 and (B) MCF 10A cells after 24 h incubation with varying cell concentrations.

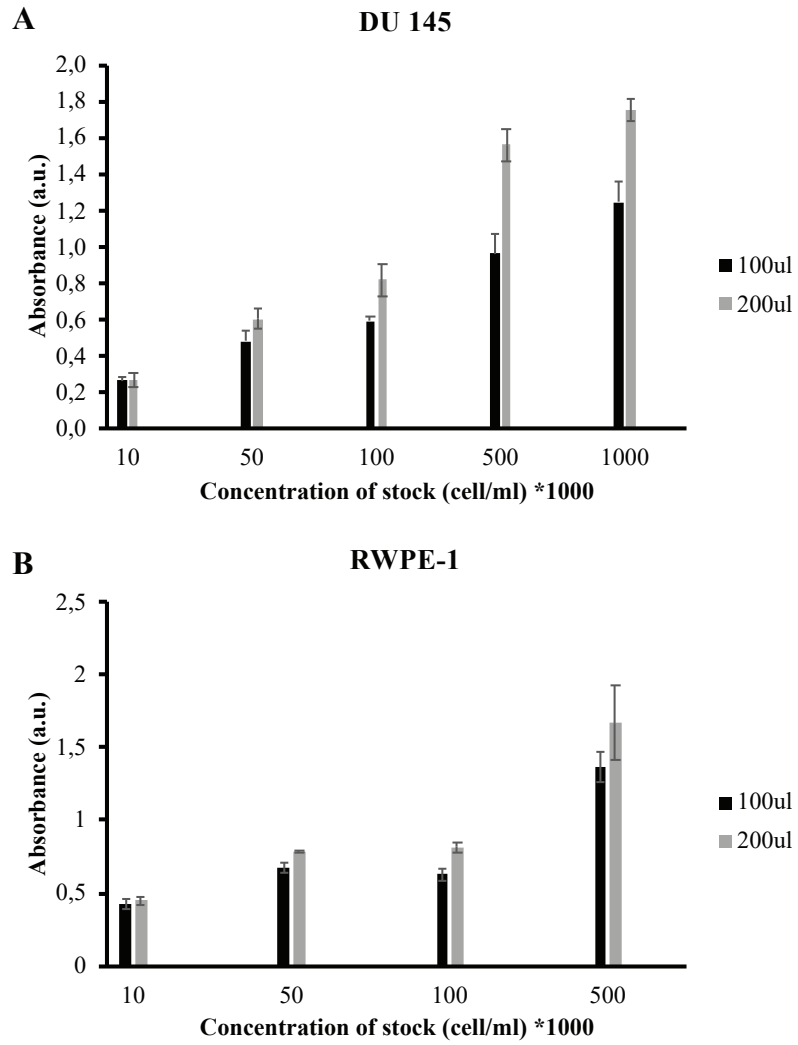


Figure A2. Cell number determination results of (A) DU 145 and (B) RWPE-1 cells after 24 h incubation with varying cell concentrations.

APPENDIX B

SEM IMAGES OF AuNBs

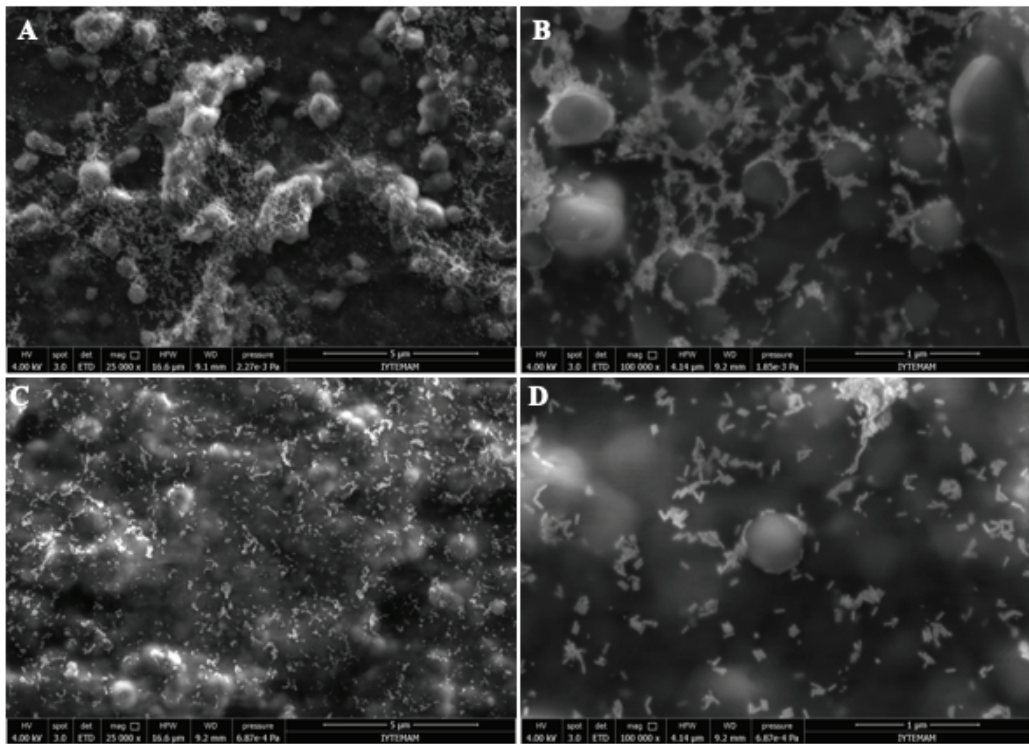


Figure B1. SEM images of AuNBs containing AuNRs with AR of 4.0 (A-B) and 7.0 (C-D).

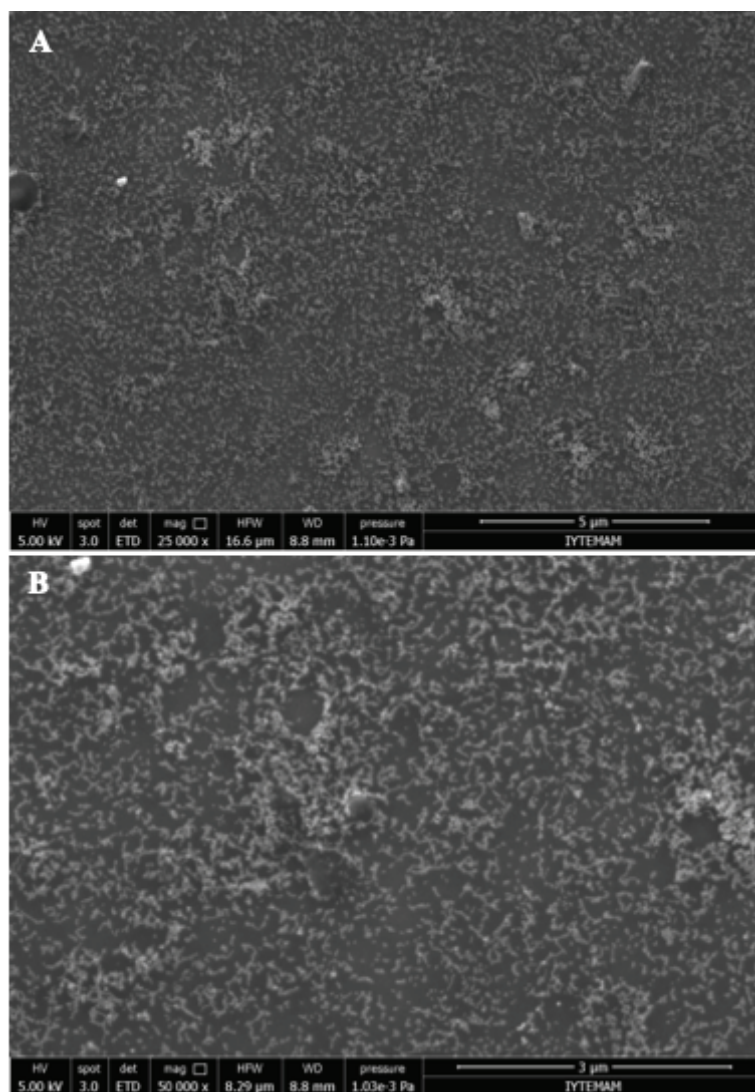


Figure B2. SEM images of AuNBs without applying nitrogen gas during the synthesis.

APPENDIX C

CELL UPTAKE HISTOGRAMS

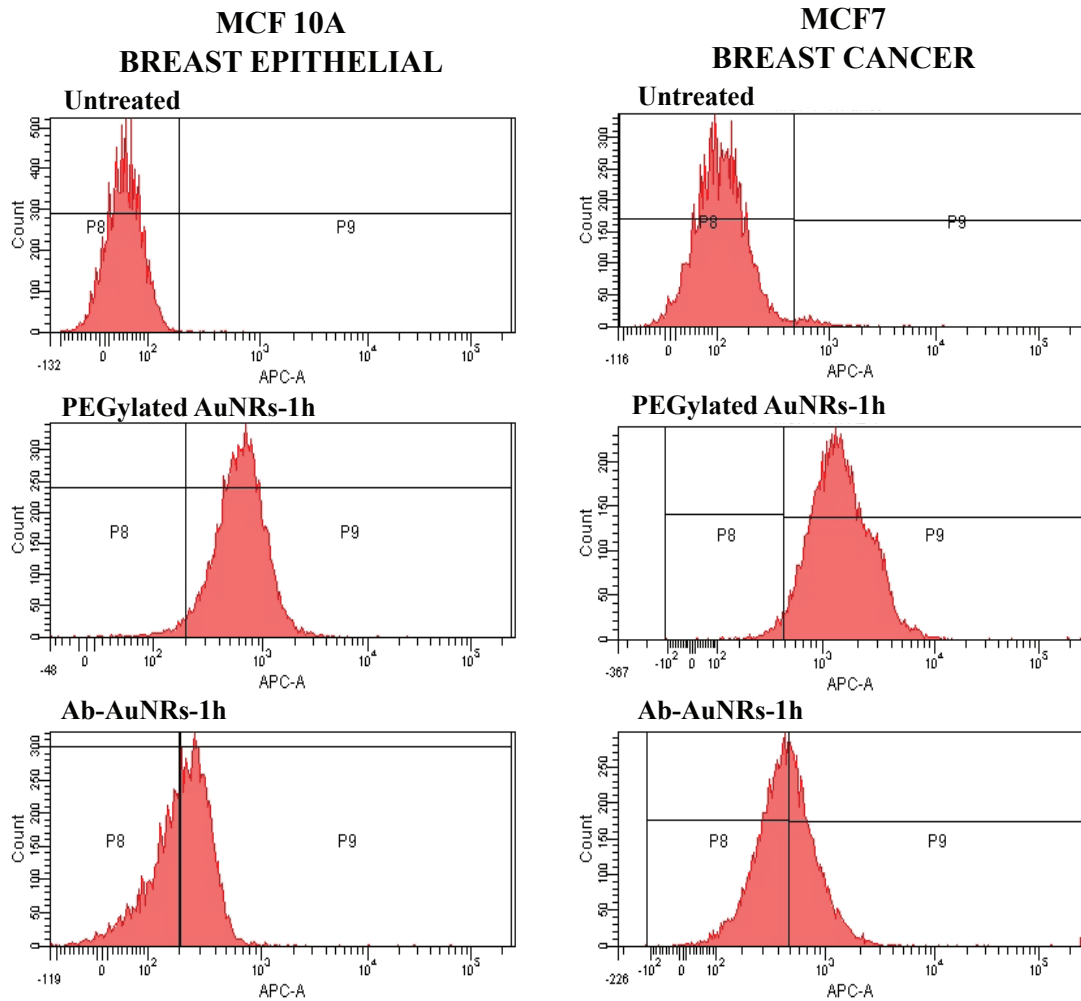


Figure C1. Cellular uptake histograms of MCF 10A breast epithelial and MCF7 breast cancer cells. Top: untreated, Middle: after incubation with fluorescent-labeled PEGylated AuNRs for 1 h and Bottom: after incubation with fluorescent-labeled Ab-AuNRs for 1 h.

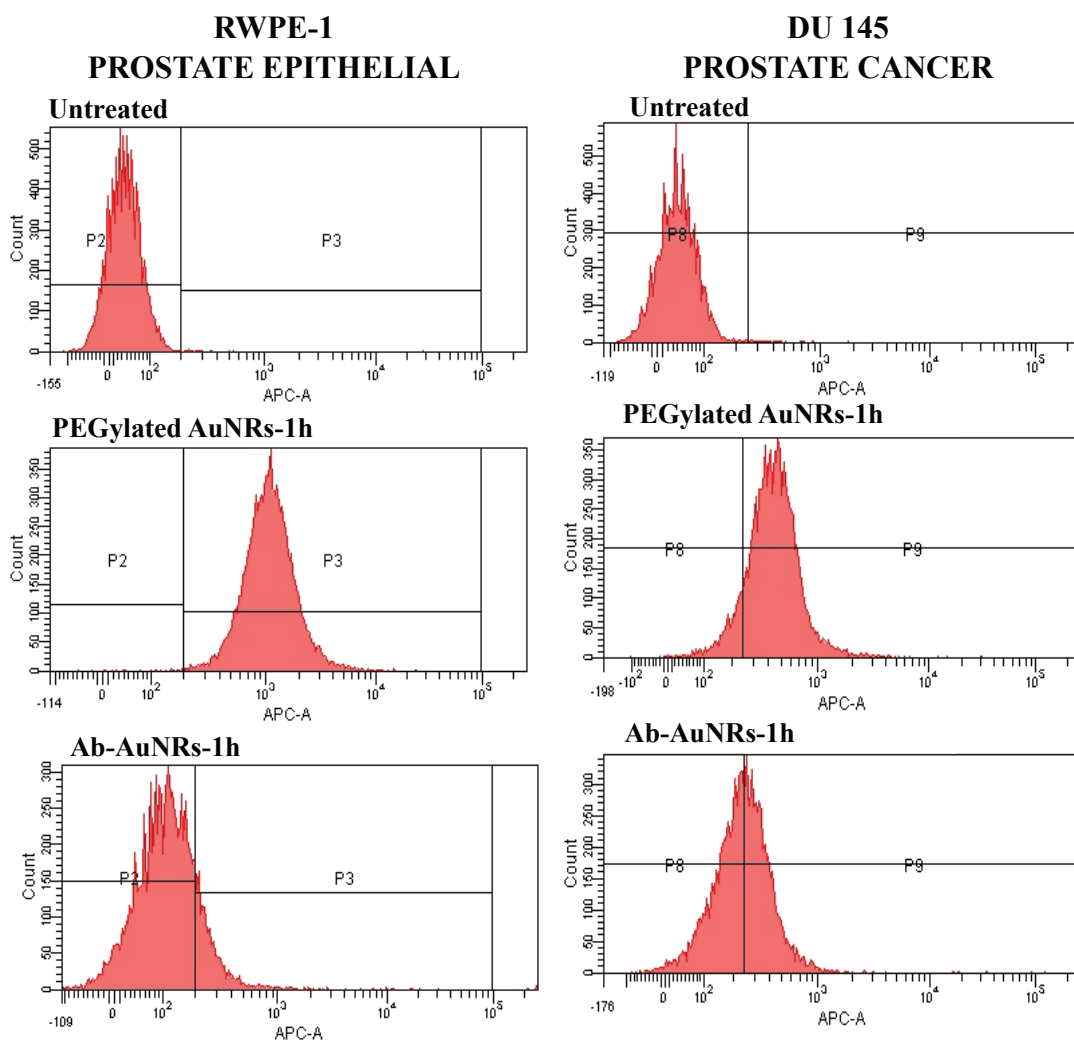


Figure C2. Cellular uptake histograms of RWPE-1 breast epithelial and DU 145 breast cancer cells. Top: untreated, Middle: after incubation with fluorescent-labeled PEGylated AuNRs for 1 h and Bottom: after incubation with fluorescent-labeled Ab-AuNRs for 1 h.

VITA

Place and Date of Birth: İZMİR / 17.08.1988

Tel : +90-(0)530-935-7159

E-Mail: ayseltomak@iyte.edu.tr / tomakaysel@gmail.com

EDUCATION

Ph. D. Materials Science and Engineering, İzmir Institute of Technology, 2014-present.

M.Sc. Nanotechnology, İzmir Gediz University, 2011-2013.

M.Sc. Chemistry Programme (Without Thesis), Celal Bayar University, 2008-2009.

BSc Chemistry, Celal Bayar University, 2004-2008.

LIST OF SCIENTIFIC PUBLICATIONS

M. Sc. Thesis: “Nanostructures for Plasmonic Biosensors”, 2013.

PUBLICATIONS

1. Moghtader, F., Tomak, A., Zareie, H., Piskin, E. “Bacterial Detection Using bacteriophages and gold nanorods by following time-dependent changes in Raman spectral signals” *Artificial Cells, Nanomedicine and Biotechnology*, 2018, 1-9.

2. Gul, A., Bacaksiz, C., Akbali, B., Unsal, E., Tomak, A., Zareie, H. M., Sahin, H. “Theoretical and Experimental Investigation of Conjugation of 1,6- Hexanedithiol on MoS₂” *Materials Research Express*, 2018, 5, 036415.

3. Ozer, I., Tomak, A., Zareie, H., Baran, Y., Bulmus, V. “Effect of Molecular Architecture on Cell Interactions and Stealth Properties of PEG” *Biomacromolecules*, 2017, 18 (9), 2699–2710.

4. Akbali, B., Yanilmaz, A., Tomak, A., Tongay, S., Celebi, C., Sahin, H. “Few- Layer MoS₂ as Nitrogen Protective Barrier” *Nanotechnology*, 2017, 28 (41), 415706.

5. Yanilmaz, A., Tomak, A., Akbali, B., Ozceri, E., Ari, O., Bacaksiz, C., Senger, R. T., Selamet, Y., Zareie, H. M. “Homogen Nitrogen Doping for Facile and Effective Modification of Graphene Surface” *RSC Adv.*, 2017, 7, 28383–28392.

6. Bor, G., Üçüncü, M., Emrulloğlu, M., Tomak, A., Şanlı-Mohamed, G. “BODIPY-conjugated chitosan nanoparticles as a fluorescent probe” *Drug and Chemical Toxicology* 2016, 1-8.

7. Kıymaz, D., Yagmurcukardes, M., Tomak, A., Sahin, H., Senger, R., Peeters, F., Zareie, H., Zafer, C. “Controlled Growth Mechanism of Poly (3- hexylthiophene) Nanowires”, *Nanotechnology* 2016, 27, 455604.

8. Tomak, A., Bacaksiz, C., Mendirek, G., Sahin, H., Hur, D., Görgün, K., Senger, R. T., Birer, Ö., Peeters, F. M., Zareie, H. M. “Structural Changes in Schiff Base Molecular Assembly Initiated By Scanning Tunneling Microscopy Tip”, *Nanotechnology* 2016, 27, 335601.

9. Tomak, A., Zareie, H. M. “Gold nanorod encapsulated bubbles”, *RSC Advances* 2015, 5, 38842.

10. Ayas, S., Cinar, G., Ozkan, A. D., Soran, Z., Ekiz, O., Kocaay, D., Tomak, A., Toren, P., Kaya, Y., Tunc, I., Zareie, H., Tekinay, T., Tekinay, A. B., Guler, M. O., Dana, A. “Label-Free Nanometer-Resolution Imaging of Biological Architectures through Surface Enhanced Raman Scattering”, *Scientific Reports* 2013, 3, 1.

EXPERIENCE: TUBITAK research project scholar 2011-present

AWARDS

1. TÜBİTAK UNIVERSITY PROJECT COMPETITIONS, Entrepreneurship and Innovation Competition, Techno-entrepreneurship Third Prize, Konya, 2017.

2. 12. International Chemical Engineering Congress “Ne üretelim?” Project Competitions, Special Award for Entrepreneurship, İzmir, 2016.

3. Technopark Entrepreneurship Competition, First Prize, “Design and Construction of Localized Surface Plasmon Resonance Spectroscopy”, İzmir, 2016.